

UNIVERSITY OF ALBERTA

**EFFECTS OF MESOSCALE CONVERGENCE ON CONVECTIVE
AND STRATIFORM RAINFALL: RADAR OBSERVATIONS AND
NUMERICAL SIMULATIONS**

by

Lingyan Xin ©

A thesis submitted to the Faculty of Graduate Studies and Research in partial fulfillment of
the requirements for the degree of DOCTOR OF PHILOSOPHY

DEPARTMENT OF EARTH AND ATMOSPHERIC SCIENCES

Edmonton, Alberta

Fall 1996



National Library
of Canada

Acquisitions and
Bibliographic Services Branch

395 Wellington Street
Ottawa, Ontario
K1A 0N4

Bibliothèque nationale
du Canada

Direction des acquisitions et
des services bibliographiques

395, rue Wellington
Ottawa (Ontario)
K1A 0N4

Your file *Votre référence*

Our file *Notre référence*

The author has granted an irrevocable non-exclusive licence allowing the National Library of Canada to reproduce, loan, distribute or sell copies of his/her thesis by any means and in any form or format, making this thesis available to interested persons.

L'auteur a accordé une licence irrévocable et non exclusive permettant à la Bibliothèque nationale du Canada de reproduire, prêter, distribuer ou vendre des copies de sa thèse de quelque manière et sous quelque forme que ce soit pour mettre des exemplaires de cette thèse à la disposition des personnes intéressées.

The author retains ownership of the copyright in his/her thesis. Neither the thesis nor substantial extracts from it may be printed or otherwise reproduced without his/her permission.

L'auteur conserve la propriété du droit d'auteur qui protège sa thèse. Ni la thèse ni des extraits substantiels de celle-ci ne doivent être imprimés ou autrement reproduits sans son autorisation.

ISBN 0-612-18136-7

Canada

UNIVERSITY OF ALBERTA

LIBRARY RELEASE FORM

NAME OF AUTHOR: Lingyan Xin

TITLE OF THESIS: Effects of mesoscale convergence on convective and stratiform
 rainfall: Radar observations and numerical simulations

DEGREE: Doctor of Philosophy

YEAR THIS DEGREE GRANTED: 1996

Permission is hereby granted to the University of Alberta Library to reproduce single copies of this thesis and to lend or sell such copies for private, scholarly, or scientific research purposes only.

The author reserves all other publication and other rights in association with the copyright in the thesis, and except as hereinbefore provided, neither the thesis nor any substantial portion thereof may be printed or otherwise reproduced in any material form whatever without the author's prior written permission.



11723-Edinboro Road
Edmonton, Alberta
Canada T6G 1Z9

Date: August 19, 1996

UNIVERSITY OF ALBERTA

FACULTY OF GRADUATE STUDIES AND RESEARCH

The undersigned certify that they have read, and recommend to the Faculty of Graduate Studies and Research for acceptance, a thesis entitled EFFECTS OF MESOSCALE CONVERGENCE ON CONVECTIVE AND STRATIFORM RAINFALL: RADAR OBSERVATIONS AND NUMERICAL SIMULATIONS submitted by Lingyan Xin in partial fulfillment of the requirements for the degree of DOCTOR OF PHILOSOPHY.



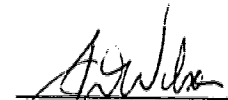
G. W. Reuter, Supervisor



P. M. K. Yau, External Examiner



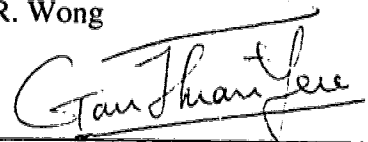
E. P. Lozowski



J. D. Wilson



R. Wong



T. Y. Gan

Date: 19 August, 1996

For my parents and my husband

ABSTRACT

Doppler velocity measurements are combined with a numerical cloud model to quantify the effects of the mesoscale convergence profile on precipitation. Our investigation involves two cases from Alberta, Canada: the 19 August 1992 convective storm, and the 28 June 1993 stratiform rain event.

The area-averaged divergence profile for the stratiform case could be determined using the Extended Velocity Azimuth Display (EVAD) method, even for radars with low maximum elevation angle. The accuracy of the EVAD-derived profile was sensitive to the accuracy of Doppler velocity measurements, and the resolution of elevation angles. For the typical operational setting of the Carvel radar, the divergence profile could only be obtained for the lowest two or three kilometers. For convective, scattered precipitation, the Velocity Volume Processing (VVP) technique provided the low-level convergence estimate accurately if the analysis volume had a spatial dimension of about 40° in azimuth and 20 km in range.

Both rain events were simulated realistically using an axis-symmetric cloud model with the initial conditions taken from observed soundings and radar-derived divergence estimates. Numerical sensitivity experiments showed that the model rainfall is enhanced when either the magnitude of the convergence or the depth of the convergence layer is increased. Rain accumulation increases monotonically but nonlinearly with larger convergence. Stronger convergence or deeper convergence layers accelerate the onset of rainfall reaching the ground. While fixing the mesoscale vertical mass flux at the top of the convergence layer, yet allowing the values of convergence magnitude and convergence depth to vary, we found that a reduction in the convergence depth is associated with a larger vertical moisture flux which

supports stronger convection. The convective rainfall depends crucially on the average vapor mixing ratio of the converging air. The water flux balance equation tends to underestimate the area-averaged stratiform rainfall rates in comparison with the cloud model values. Model results show that stronger upper-level divergence tends to enhance the surface stratiform rainfall, but does not affect the time onset of rain.

Acknowledgments

I would like to present my sincere gratitude to Dr. G. W. Reuter, my supervisor, for his expert guidance and perceptive advice throughout this project. His help and valuable suggestions are gratefully acknowledged.

I wish to express my thanks to Dr. E. P. Lozowski, Dr. J. D. Wilson and Dr. R. B. Charlton for their kindness during my study period, and their careful reading of the manuscript and pertinent comments. My appreciation is also given to Dr. M. K. Yau who kindly accepted the role of the External Examiner, and Dr. R. Wong and Dr. T. Y. Gan for their presence at my oral defence examination.

My heartfelt thanks are going to Mr. Bruno Larochelle for his assistance in archiving and processing the radar data employed in this project. The unhesitant help and various support from Mr. T. Thompson, Mrs. L. Smith and others are also very much appreciated.

Thanks also, to Victor Chung, Brian Crenna and Russ Sampson, who did a lot on my thesis editing, and all other graduate students for their support and friendship.

Financial support for this research was provided by the Natural Sciences and Engineering Research Council and the Atmospheric Environment Service of Environment Canada.

Special thanks are given to Ning - my husband, for his invaluable, heart-whole support and encouragement.

Table of Contents

Chapter 1	Introduction	1
1.1	Research topic	1
1.2	Alberta storms and relevant research review	2
1.3	Statement of research problems	4
1.4	Research methodology for this study	5
1.4.1	Radar data analysis techniques for estimating convergence	5
1.4.2	Numerical cloud model	7
1.4.3	Initialization of numerical cloud model using radar data	8
1.5	Organization of the thesis	9
	References	11
Chapter 2	Divergence Profile Derivation in Stratiform Precipitation Using the EVAD Algorithm	17
2.1	Introduction	17
2.2	The EVAD technique	18
2.2.1	The VAD analysis	18
2.2.2	The EVAD technique	21
2.2.3	Variable regression	22
2.3	Examination of the EVAD analysis in a simulated wind field	23
2.3.1	Influence of measurement errors in Doppler velocity	23
2.3.2	Influence of highest elevation angles	26
2.3.3	Influence of analysis cylinder radius	26
2.3.4	Influence of hydrometeor fall speed	27
2.4	Application of the EVAD analysis on 23 June 1993	28
2.4.1	Synoptic situation	28
2.4.2	Radar observations of precipitation	29
2.4.3	The EVAD results for 23 June 1993	29

2.5 Conclusions	32
References	49

Chapter 3 Estimation of Divergence in Scattered Echo Regions Using the VVP Technique	51
3.1 Introduction	51
3.2 The method	52
3.3 The VVP error analysis and geometry of analysis volume	55
3.3.1 Seven-parameter VVP technique	55
3.3.2 Error analysis	57
3.3.3 Effects of geometry of analysis volume on estimates	58
3.4 Application of the VVP technique to the Carvel radar	60
3.4.1 Synoptic situations	60
3.4.2 Radar observations	61
3.4.3 The VVP results	61
3.5 Summary and conclusions	64
References	71

Chapter 4 Numerical Cloud Model	73
4.1 General considerations	73
4.2 Basic assumptions	74
4.3 Model equations	75
4.4 Parameterization of microphysical processes	78
4.5 Subgrid turbulence parameterization	79
4.6 Numerical techniques	84
4.6.1 Stretched coordinate	84
4.6.2 Finite space difference scheme	87
4.6.3 Finite difference equations	87
4.6.4 Time integration scheme	90
4.6.5 Numerical adjustment procedures for saturation	90

4.7 Boundary conditions	92
4.8 Initial conditions	95
4.9 Summary	96
References	99

Chapter 5 Numerical Simulation of the Effects of Mesoscale

Convergence on Convective Rain Showers	101
5.1 Introduction	101
5.2 Numerical cloud model	105
5.2.1 General characteristics	105
5.2.2 Mesoscale convergence and initialization	106
5.2.3 Numerical aspects	108
5.3 Simulation of control case	109
5.3.1 Environmental conditions	109
5.3.2 Evolution of cloud and precipitation	110
5.3.3 Comparison with radar observations	112
5.4 Results of sensitivity experiments	114
5.4.1 Specifications of experiments	114
5.4.2 Effects of the magnitude of boundary-layer convergence	115
5.4.3 Effects of the depth of boundary-layer convergence	118
5.4.4 Relative contributions of the convergence magnitude versus its depth	119
5.5 Summary and conclusions	121
References	139

Chapter 6 Stratiform Rainfall Rates from the Water Flux Balance Equation and Numerical Cloud Model

6.1 Introduction	143
6.2 Numerical model	145
6.3 Control case simulation	146
6.3.1 Observations on 23 June 1993	146

6.3.2 Simulation results for the control case	148
6.3.3 Comparison of model results with observations	148
6.4 Evaluation of the water flux balance equation for estimating rainfall rates	149
6.4.1 Sensitivity to the magnitude of convergence	150
6.4.2 Sensitivity to the depth of convergence layers	152
6.4.3 Sensitivity to the upper-level divergence	152
6.5 Discussion and conclusion	154
References	167
Chapter 7 Conclusions	169
References	174
Appendix A: Characteristics of carvel Doppler radar	176
Appendix B: Doppler radar data preprocessing	178

List of Tables

<i>Tables</i>	<i>Content</i>	<i>Page</i>
3.1	Typical values of simulated wind parameters used in VVP analysis	55
3.2	Comparison of the VVP analyses for different kinematic parameters	56
3.3	Effects of the geometry of an analysis volume on the VVP estimates	59
5.1	Comparison of model results with observations for the convective case	114
5.2	Specification of numerical sensitivity experiments for the convective case ...	116
6.1	Comparison of model results with observations for the stratiform case	149
A.1	Characteristics of Carvel Doppler radar	177

List of Figures

<i>Figures</i>	<i>Content</i>	<i>Page</i>
2.1	Geometry for the scan of Doppler velocity on a circle	34
2.2	Radar volume scans consisting of different elevation angles	35
2.3	Constant-elevation cones of data used for the EVAD analysis	36
2.4	Sensitivity of divergence estimate to error amplitudes in Doppler velocity	37
2.5	Sensitivity of divergence estimate to uncertainty in Doppler velocity	37
2.6	Schematic relationship between EVAD analysis and elevation angles	38
2.7	Effects of elevation angles on EVAD divergence profile	39
2.8	Effects of analysis cylinder radius on EVAD divergence profile	40
2.9	Effects of hydrometeor fall speed on EVAD divergence estimate	41
2.10	500 hPa, and surface analyses for 0000 UTC 23 June 1993	42-43
2.11	CAPPI 1.5 km radar images from 0030 to 0400 UTC 23 June 1993	44
2.12	Divergence profiles from EVAD analyses for the 23 June 1993 case	45
2.13	Vertical velocity profiles from divergence for the 23 June 1993 case	46
2.14	Profile of horizontal mean wind from EVAD analyses on 23 June 1993	47
2.15	Comparison of EVAD wind profiles with VAD result and sounding data	48
3.1	Geometry of analysis volume for the VVP technique	65
3.2	850 hPa analysis for 0000 UTC 19 August 1992	66
3.3	Tephigram analysis for 1200 UTC 19 August 1992 sounding data	67
3.4	Radar reflectivity 0.5° PPI for 0630 UTC 19 August 1992	68
3.5	Radar reflectivity 0.5° PPI for 0700 UTC 19 August 1992	68
3.6	Divergence field from VVP analysis for 0630 UTC 19 August 1992	69
3.7	Standard error field of divergence estimate for 0630 UTC 19 August 1992 ..	69
3.8	Horizontal deformation field from VVP analysis for 0630 19 August 1992 ...	70
3.9	Vertical wind shear field from VVP analysis for 0630 19 August 1992	70

4.1	Flow diagram describing microphysical processes in cloud model	97
4.2	Staggered grid arrangement used in cloud model integration	98
5.1	Tephigram analysis for 1200 UTC 19 August 1992	124
5.2	Initial conditions for the control case simulation on 19 August 1992	125
5.3	Evolution of maximum vertical velocity and total kinetic energy for the control case simulation	126
5.4	Vertical cross sections of stream function, equivalent potential temperature, cloud water mixing ratio, and radar reflectivity for the control run	127-130
5.5	Comparison of radar-observed and simulated area-averaged rainfall rates for the control run	131
5.6	Schematic vertical profile of divergence used in sensitivity experiments	132
5.7	Effect of convergence magnitude on evolution of rain accumulation and rainfall rate	133
5.8	Time needed for rain production versus convergence magnitude	134
5.9	Effect of convergence magnitude on evolution of kinetic energy	135
5.10	Sounding analysis just before the onset of convection for experiments sensitive to convergence magnitude	136
5.11	Effect of convergence depth on evolution of rain accumulation and rate	137
5.12	Evolution of kinetic energy, upward vapor flux through cloud base, and accumulated rainfall sensitive to the ratio of convergence magnitude to convergence depth	138
6.1	Tephigram analysis for 0000 UTC 23 June 1993 sounding data	156
6.2	Divergence profile from EVAD analysis for 0030 UTC 23 June 1993 used to initialize the model for the control case simulation	157
6.3	Evolution of accumulated rain and peak updraft for the control run	158
6.4	Height-time pattern of radar reflectivity for the control run	159
6.5	Schematic divergence profile used in numerical sensitivity experiments	160
6.6	Comparison of peak updraft evolution for different surface convergences ...	161

6.7	Height-time patterns of reflectivity for various surface convergences	162
6.8	Evolution of accumulated rain, and averaged rainfall rate versus surface convergence magnitude	163
6.9	Evolution of accumulated rain, and averaged rainfall rate versus the depth of convergence	164
6.10	Schematic vertical distributions of divergence used to examine the effects of upper-level divergence on surface rainfall	165
6.11	Effect of upper-level divergence on evolution of accumulated rainfall; and averaged rainfall rate versus divergence maximum	166

CHAPTER 1

INTRODUCTION

1.1 Research Topic

The formation, maintenance and decay of clouds and precipitation are closely associated with the vertical motion in moist air. In a convectively unstable environment, upward motion provides the required lift to release latent instability. As air rises, it cools adiabatically, causing condensation, formation of cloud droplets, and development of subsequent precipitation. During condensation, latent heat is released that strengthens the cloud updraft. Rising of air at cloud base is often associated with convergence in the low-level air flow.

Low-level convergence has been found to be present before the development of organized convective systems (e.g., Lewis 1971, Lewis et al. 1974, Ogura et al. 1979, Chen and Ogura 1982, and Purdom 1982). Byers and Braham (1949) found surface convergence at least 30 min prior to a storm event. During a mesoscale experiment in Florida, Ulanski and Garstang (1978) investigated the role of surface convergence in the formation, maintenance and decay of convective storms. They concluded that surface convergence is a cause, rather than an effect, of the storms, since strong surface convergence developed at least 90 minutes prior to the first radar echoes. By examining the kinematic structure of the pre-thunderstorm environment during the Severe Environmental Storms And Mesoscale Experiment (SESAME), Sidkar and Fox (1983) found distinct cells of surface convergence preceding initial radar echoes by four hours. Doneaud et al. (1983) confirmed the earlier studies that the development of convergence areas precedes radar echoes. Cotton et al. (1983) found that the dominant feature which influenced the development of a mesoscale convective complex was low-level convergence.

Thunderstorms, developing frequently over the foothills of the Rocky Mountains,

are associated with regions of leeside convergence (Henz 1973, Barker and Banta 1984, 1985). The positions of radar-detectable convergence lines and the formation of convective storms were strongly correlated in eastern Colorado (Wilson and Schreiber 1986). At least 80% of the storms were initiated along preexisting radar-detected convergence boundaries. Subsequent investigations (Mueller and Wilson 1989, Carbone et al. 1990) have confirmed the importance of boundary-layer convergence on storm locations.

1.2 Alberta Storms and Relevant Research Review

Low-level convergence tends to precede summer severe convection in central Alberta (e.g., Honch 1989). Central Alberta is affected by hail on an average of 80 or more days each summer (Renick 1979), and experiences about 10 to 20 tornadoes annually (Newark 1984). Alberta farmers suffer about 40 to 50 million dollars in crop losses each year. A particularly disastrous event was the Edmonton tornado on 31 July 1987, which left 27 people dead, 300 injured and caused 250 million dollars in property damage (Bullas and Wallance 1988). The severe hailstorm which swept over Calgary on 7 September 1991 cost insurance companies more than 400 million dollars (Charlton et al. 1995).

To study the formation and possible modification of hailstorms, field experiments were conducted in central Alberta from 1956 to 1985. Some important findings of these activities involved: formation and growth of hail (Longley and Thompson 1965, English 1973); distribution of hailstone size (Cheng and English 1983); water budget of hailstorms (Rogers and Sakellariou 1986); and hail forecasting (Renick and Maxwell 1977). To investigate the initiation of severe convection, the **Limestone Mountain EXperiment, (LIMEX)** was conducted in the Alberta foothills in July of 1985 (Strong 1985). Smith and Yau (1993a, b) used the high resolution surface and sounding data from LIMEX to determine the factors that differentiate severe from non-severe convective outbreaks. They concluded that under generally clear skies, cumulus convection begins over the Alberta

foothills as strong surface heating removes the capping lid. Convective outbreaks occur when an approaching synoptic scale upper-level trough is in phase with strong surface heating over the Alberta foothills. East and northeast surface winds transport moist air from the plains to the foothills, and the normal mountain-plain circulation is amplified by the deep destabilization which is localized over the elevated foothills. Honch (1989), also using the LIMEX data, found that Alberta thunderstorm initiation is directly associated with strong surface convergence in the lee of the Rocky Mountains. Strong upward motion, resulting from convergence zones along the foothills of Alberta, appears five hours before storm events. By analysing the LIMEX moisture fields, Brennand (1992) concluded that moisture convergence tended to precede storm development by two to four hours. The convergence below 750 mb remained during the entire period of storm formation.

Radar studies on Alberta convection began in the 1960's with the installation of an S-band polarization radar in Penhold (52°20' N, 113°08' W). The radar polarization capability provides a useful tool to distinguish hail from heavy rain (Al-Jumily et al. 1991), and improve on estimating rainfall rate for heavy precipitation (English et al. 1991). In 1990, the radar at Carvel (53°35' N, 114°09' W) was upgraded to allow Doppler wind measurements. Carvel radar observations have been used to investigate the organization of cloud and precipitation (Reuter and Nguyen 1993), the severe storm structure (Holt et al. 1994), and the kinematic characteristics of gust fronts and mesocyclones (Laroche 1994).

In this thesis, data from the Carvel Doppler radar will be used to compute mesoscale convergence. The main characteristics of the Carvel radar are: a 5.34 cm wavelength, a 1.4° azimuthal beam width, and a 113 km maximum unambiguous range of echoes. Measurements of radar reflectivity factor and Doppler velocity are recorded in 220 gates each 500 m long spaced continuously along the beam. Data are sampled at three elevation angles of 0.5°, 1.5° and 3.5° in 10 min cycles. The average spacing between successive azimuths of data is 0.5°. More information about the Carvel radar characteristics is provided in Appendix A.

1.3 Statement of Research Problems

Observations show that low-level convergence influences the development of subsequent precipitation. So, information on the strength and location of convergence should improve our understanding of cloud convection. **The first objective of this thesis is to retrieve convergence estimates from the Doppler velocity data measured by the Carvel radar.** Two different retrieval algorithms are used for convective and stratiform precipitation cases, respectively. The focus is on quantifying how the accuracy of the convergence estimates is affected by radar elevation angles, detecting ranges, the size of the analysis volume and the error margin in Doppler velocity measurements.

The second objective of this thesis is to investigate the quantitative effects of the divergence profile on cloud formation and precipitation using a numerical cloud model. Previous numerical studies were focused on relating low-level convergence to the occurrence of precipitation. This research is the first comprehensive attempt to quantify this relationship and examine the effect of the entire vertical profile of divergence on cloud formation and precipitation. To achieve this objective, the radar-derived area-averaged convergence values are used to initialize a cloud model to simulate the subsequent evolution of rain events. Model results are compared with observations to evaluate its performance, and thus to examine the feasibility of using Doppler velocity data as input parameters for numerical cloud simulations. Then, we investigate the effects of individual convergence parameters (e.g., the magnitude and the depth of convergence) on surface rainfall through numerical sensitivity experiments. The impact of upper-level divergence on rain intensity is also examined.

This research is undertaken using two case studies for central Alberta. One is a convective case associated with a multicell summer storm which occurred on 19 August 1992. Another case is a long-lasting stratiform rain event produced by a large-scale low-pressure system on 23 June 1993. Although convective storms frequently occur in Alberta region during summer, long-lasting heavy stratiform precipitation may also cause serious flooding (Reuter and Nguyen 1993). So, the case study on the stratiform rain event is to complement previous studies on the relation between convergence and stratiform rain.

1.4 Research Methodology for This Study

1.4.1 Radar data analysis techniques for estimating convergence

Before 1979, few mesoscale research experiments were made to investigate the convergence in storm environments, mainly because of inadequate coverage of operational networks. Doppler weather radars are now in place with sufficient sensitivity to measure radial wind component even in pre-storm environments.

The inherent limitation of measuring only the **radial** component of the wind vector (along the radar beam direction) has to be overcome when estimating kinematic properties of the wind field. The determination of a 3-D airflow pattern is possible when three or more Doppler radars are deployed simultaneously to view the same volume (Armijo 1969). Since multiple-Doppler techniques require elaborate coordination and are limited in areal coverage, a multiple-Doppler radar analysis is conceivable in a research environment, but not economically feasible for operational application. From the radial velocities sampled by a **single** Doppler radar, only some kinematic parameters (such as divergence) can be estimated, while others such as vorticity remain ambiguous.

The methods primarily used to retrieve the kinematic characteristics of mesoscale wind are the Velocity Azimuth Display (VAD, Lhermitte and Atlas 1961, Caton 1963, Browning and Wexler 1968); the Volume Velocity Processing (VVP, Waldteufel and Corbin 1979, Koscielny et al. 1982), and the Extended VAD (EVAD, Srivastava et al. 1986, Matejka and Srivastava 1991) algorithms. These techniques use the same simplifying assumption about the structure of the wind field: that is, the wind field is assumed to vary linearly in space. With this linear assumption the velocity components can be approximated by a truncated Taylor series expression. Keeping only up to the first derivative, the wind field inside the observed domain is described by the sum of the value at the centre and the gradient terms. This removes the ambiguity of only radial component of a velocity vector detected by a single Doppler radar. Kinematic parameters of the wind are determined through the linear regression of Doppler velocities in corresponding spatial volume.

The VAD technique is an analysis of radial velocities when radar detects the air at

one constant range gate and one constant elevation angle over the entire 360 degrees of azimuth. Doppler velocities are collected on each measured *circle* or *ring* (horizontally arranged). By fitting the zeroth, fundamental, and second Fourier harmonics to Doppler velocities about the circle centred on the radar, areal-averaged estimates of horizontal divergence, mean wind and deformation around the radar for that ring are obtained.

Srivastava et al. (1986) and Matejka and Srivastava (1991) introduced the Extended VAD analysis (acronym EVAD). Assuming the vertical component of air velocity is negligible compared to the terminal velocity of hydrometeors, the divergence and the hydrometeor fall speed are determined using least-squares fits in successive thin-altitude sections. Then, the profiles of these two quantities are obtained. To estimate the divergence only, the EVAD analysis does not require the assumption of linear wind variation. However, the EVAD method is applicable for uniform wind fields (at most quadratic variation) without significant gaps in echo regions, and therefore can only be used in widespread, stratiform rain situations (Matejka and Srivastava 1991). Srivastava et al. (1986) used the EVAD method to retrieve the profile of divergence within a region of widespread precipitation associated with a summertime midlatitude squall line. The profile of vertical air motion, derived by applying the anelastic mass continuity equation to the EVAD divergence, compared well with that obtained from multiple Doppler radar analysis.

Since wind is rarely uniform over large volumes surveyed by a radar, especially during summer time convection, Doppler velocities have to be analysed within smaller areas. Waldteufel and Corbin (1979) suggested processing data within a 3-D *volume sector* (VVP) rather than within an area consisting of full azimuths as in the VAD and the EVAD analyses. With the use of Doppler velocities within the volume sector, the horizontal and vertical derivatives of the wind field are deduced. Because of the small sampling volume, the VVP technique is applicable to small areas when radar echoes are dispersed. Koscielny et al. (1982), using the VVP technique, found that areas of convergence coincided with regions of subsequent storm development. Johnston (1984) used a similar technique to examine the kinematic structure of cold frontal rainbands. The

potential of using the VVP method for nowcasting storm outbreaks in central Oklahoma was illustrated by Smith and Rabin (1989). Long et al. (1990) used the VVP technique to investigate the mesoscale kinematics of a winter mountain storm in southwest Utah. They found that low-level convergence existed ahead of a cold front, and was maintained throughout the lifetime of the winter storm.

In this study, we will use the EVAD method to retrieve the vertical profile of area-averaged convergence for the stratiform rain event occurring on 23 June 1993. With a spatial resolution of about 20 km, the VVP technique is adopted to estimate the convergence field in scattered echo regions for the convective storm on 19 August 1992.

1.4.2 Numerical cloud model

Radar, instrumented aircraft, and weather satellites provide essential information about structure and development of cloud convection and precipitation. However, observations alone are still inadequate to yield simultaneously the fields of temperature, pressure, cloud water, rainwater etc., which are needed to improve the understanding of cumulus dynamics and cloud microphysics. To supplement observations, numerical cloud models have emerged as useful tools to provide the relevant fields **simultaneously** in a physically consistent way. A numerical cloud model is a mathematical description of the complex interactions of the dynamic, thermodynamic and microphysical processes that occur in clouds. The basic equations of a numerical cloud model are those for the conservation of momentum, mass, and energy.

Using a time-dependent slab-symmetric two-dimensional model, Chang and Orville (1973) found that model runs with the inclusion of boundary-layer convergence led to a broader and more intense cumulus than runs without convergence. Using a more sophisticated approach, Chen and Orville (1980) showed that the convection became more intense when low-level convergence existed, while the convection was suppressed in the presence of low-level divergence. More vigorous storms with greater precipitation intensities occurred when low-level convergence instead of divergence was present in three-dimensional simulations (Tripoli and Cotton 1980). The persistence of strong low-

level convergence increases the surface rainfall by 40% for a typical midlatitude condition. (Crook and Moncrieff 1988).

The focus of the above modelling studies was on showing differences in model simulations with and without convergence. Those results indicated the important role of low-level convergence in the development of convection. In this thesis we will quantify the effects of the magnitude and the depth of convergence on cloud formation and subsequent precipitation. To make the computational demands manageable, our model adopts the assumption of symmetry around a vertical axis. The advantages and limitations of using an axi-symmetric cloud model will be discussed in detail in Chapters 4 and 5.

1.4.3 Initialization of numerical cloud model using radar data

In cloud models, the initial conditions are generally specified by horizontally homogenous wind, temperature and humidity profiles obtained from an observed rawinsonde sounding. For a convective cloud, the sounding presumably contains positive Convective Available Potential Energy (CAPE). Then, a perturbation is introduced to initiate the convection process. The most common method is that of a thermal (or moist) bubble near the cloud base height (e.g., Miller and Pearce 1974, Klemp and Wilhelmson 1978, and Rotunno et al. 1988). Simulations employing this “bubble” technique, however, often lead to unrealistic features in the simulated storms (Clark 1979, Tripoli and Cotton 1980). To alleviate this defect, more realistic initial perturbations have been introduced. Tripoli and Cotton (1980) used a horizontally homogeneous field of initial vertical motion to simulate the effect of large-scale convergence on convection. Smolarkiewicz and Clark (1985) used a surface-layer forcing calculated from mesonet data. Johnson et al. (1989) used differential surface heating obtained from a surface energy balance model.

With the remarkable progress in Doppler radar observations of convective storms, there is growing interest in the combined use of numerical cloud models and radar data to “predict” the development of cloud and precipitation (Laroche and Zawadzki 1995). Recently, an adjoint method has been developed to retrieve wind, thermodynamic, and microphysics information by fitting radar-observed radial velocity and reflectivity values to

an anelastic cloud model (e.g., Sun et al. 1991, Gal-Chen and Zhang 1993, and Laroche and Zawadzki 1994). Case studies using this method have been carried out by Sun and Crook (1994), Shapiro et al. (1995), and Sun et al. (1995). However, this method is computationally demanding and is not without flaws (Sun et al. 1995). Rather than applying the adjoint method, Lin et al. (1993) used the 3-D wind fields directly derived from multiple-Doppler radar data for a tornadic storm to initialize the convective storm simulation. There was a fairly good agreement between the simulated storm and observations.

Our research is a new attempt to combine the data measured by an operational single Doppler radar with an axi-symmetric cloud model. The divergence profiles, which are obtained from the EVAD (stratiform rain event) and the VVP (convective case) analyses, are used to initialize the numerical cloud model. These divergence profiles are utilized for the boundary conditions (i.e., the radial flow through the lateral boundary), and also for the initial wind field.

1.5 Organization of the Thesis

In Chapter 2, the EVAD technique is described. It is then applied to a widespread stratiform precipitation event occurring in central Alberta on 23 June 1993. Error analyses are made to evaluate the reliability of the EVAD estimates when Doppler velocity data are sampled at very few scans.

The VVP technique is described in Chapter 3. The dependence of the accuracy of the estimated wind kinematic properties (e.g., divergence, deformation) on the size and shape of sampling volumes and on the number of kinematic parameters in the algorithm is examined. The multicell storm of 19 August 1992 is studied with the VVP analysis. Interpretations are made on the analyses obtained.

Chapter 4 presents the axi-symmetric cloud model used in the current study. The basic assumptions, model equations, parameterization schemes and numerical methods are described.

Chapter 5 deals with the numerical simulation of the storm on 19 August 1992. The VVP-derived convergence is used to initialize the model wind field, and the model results are compared with radar observations. A series of sensitivity experiments are then presented to show the effects of various convergence parameters (such as the magnitude, and the depth of convergence, and their ratio) on the time onset and intensity of convection and precipitation.

In Chapter 6, we apply the EVAD divergence profile to modelling the stratiform rain event. By performing numerical sensitivity experiments using different magnitudes and depths of low-level convergence, and different patterns of upper-level divergence, the effects of the divergence profile on the development of stratiform precipitation are quantified.

The major findings of this research are summarized in Chapter 7. Suggestions for future research regarding the combined use of a single-Doppler radar and a numerical cloud model are also briefly presented.

References

- Armijo, L., 1969: A theory for the determination of wind and precipitation velocities with Doppler radar. *J. Atmos. Sci.*, **26**, 570-573.
- Al-Jumily, K. J., R. B. Charlton, and R. G. Humphries, 1991: Identification of rain and hail with circular polarization radar. *J. Appl. Meteor.*, **30**, 1075-1087.
- Barker, C. L., and R. M. Banta, 1984: The role of mesoscale convergence in convective cloud initiation in mountainous terrain. *Preprints, 10th Conf. on Wea. Forecasting and analysis*. Amer. Meteor. Soc., 555-558.
- _____, and _____, 1985: Preferred regions of thunderstorm initiation over the Colorado Rockies. *Preprints, 14th Conf. on Severe Local Storms*. Amer. Meteor. Soc., 17-20.
- Brennand, M.P., 1992: Convective storms and moisture fields in LIMEX85: A case study. M.Sc. Thesis, University of Alberta, Edmonton, 136 pp.
- Browning, R. A., and R. Wexler, 1968: The determination of kinematic properties of wind field using Doppler radar. *J. Appl. Meteor.*, **7**, 105-113.
- Bullas, J. M., and A. F. Wallace, 1988: The Edmonton Tornado, July 31, 1987. *Preprints, 15th Conf. on Severe Local Storms*, Baltimore, Amer. Meteor. Soc., 437-443.
- Byers, H. R., and R. R. Braham, Jr., 1949: The Thunderstorm. U.S. Govt. Printing Off., Washington, D. C., 187 pp.
- Carbone, R. E., J. W. Conway, N. A. Crook, and M. W. Moncrieff, 1990: The generation and propagation of a nocturnal squall line. Part I: Observations and implications for mesoscale predictability. *Mon. Wea. Rev.*, **118**, 26-49.
- Caton, P. G. F., 1963: The measurement of wind and convergence by Doppler radar. *Proc. 10th Conf. on Radar Meteor.*, Washington, DC, Amer. Meteor. Soc., 290-296.
- Chang, S. M., and H. D. Orville, 1973: Large-scale convergence in a numerical cloud model. *J. Atmos. Sci.*, **30**, 947-950.
- Charlton, R. B., B. M. Kachman, and L. Wojtiw, 1995: Urban hailstorms: A view from Alberta. *Natural Hazards*, **12**, 29-75.
- Chen, Y.-L., and Y. Ogura, 1982: Modulation of convective activity by large-scale flow pattern observed in GATE. *J. Atmos. Sci.*, **39**, 1260-1279.

- Chen, C. H., and H. D. Orville, 1980: Effects of mesoscale convergence on cloud convection. *J. Appl. Meteor.*, **19**, 256-274.
- Cheng, L., and M. English, 1983: A relationship between hailstone concentrations and size. *J. Atmos. Sci.*, **40**, 204-213.
- Clark, T. L., 1979: Numerical simulations with a three-dimensional cloud model: Lateral boundary condition experiments and multi-cellular severe storm simulations. *J. Atmos. Sci.*, **36**, 2191-2215.
- Cotton, W. R., R. L. George, P. J. Wetzel, and R. L. McAnelly, 1983: A long-lived mesoscale convective complex. Part I: The mountain-generated component. *Mon. Wea. Rev.*, **111**, 1893-1918.
- Crook, N. A., and M. W. Moncrieff, 1988: The effect of large-scale convergence on the generation and maintenance of deep moist convection. *J. Atmos. Sci.*, **45**, 3606-3624.
- Doneaud, A. A., J. R. Miller, D. L. Priegnitz, and L. Viswanath, 1983: Surface mesoscale features as potential storm predictors in the northern great plains: two case studies. *Mon. Wea. Rev.*, **111**, 273-292.
- English, M., 1973: Growth of large hail in Alberta hailstorms, Part II. *Met. Monogr.*, **36**, 37-98.
- _____, B. Kochtubajda, and F. D. Barlow, 1991: Radar measurements of rainfall by differential propagation phase: A plot experiment. *Atmos. Ocean*, **29**, 357-380.
- Gal-Chen, T., and J. Zhang, 1993: On the optimal use of reflectivities and single Doppler radar velocities to deduce 3-D motion. *Preprints, 26th Conf. on Radar Meteor.*, Amer. Meteor. Soc., 414-416.
- Henz, J. F., 1973: Characteristics of severe convective storms on Colorado's High Plains. *Preprints, 8th Conf. on Severe Local Storms*, Denver, Amer. Meteor. Soc., 96-103.
- Honch, R. W., 1989: Mesoscale vertical velocity fields in the lee of the Alberta Rockies: A case study. M.Sc. Thesis, University of Alberta, Edmonton, 125 pp.
- Holt, A. R., P. I. Joe, R. McGuinness, E. Torlaschi, T. Nichols, F. Bergwall, and D. A. Holland, 1994: Simultaneous polarization and Doppler observations of severe convective storms in central Alberta. *Atmos. Res.*, **33**, 37-56.

- Johnston, B. W., 1984: The kinematic structure of cold frontal rainbands. Rep. AS146, Dept. of Atmos. Sci., University of Wyoming.
- Johnson, K. W., M. E. Raffensberger, P. S. Ray, and S. L. Lang, 1989: Comparisons between numerical simulations and Doppler radar observations of an isolated mountain thunderstorm. *Preprints, 24th Conf. on Radar Meteor.*, Tallahassee, FL, Amer. Meteor. Soc., 34-37.
- Klemp, J. B., and R. B. Wilhelmson, 1978: The simulation of three-dimensional convective storm dynamics. *J. Atmos. Sci.*, **35**, 1070-1096.
- Koscielny, A. J., R. J. Doviak and R. Rabin, 1982: Statistical considerations in the estimation of divergence from single Doppler radar and application to pre-storm boundary-layer observation. *J. Appl. Meteor.*, **21**, 197-210.
- Laroche, S., and I. Zawadzki, 1994: A variational analysis method for retrieval of three-dimensional wind field from single-Doppler radar data. *J. Atmos. Sci.*, **51**, 2664-2682.
- _____, and _____, 1995: A single-Doppler radar data assimilation cycle. *Preprints, 27th Conf. on Radar Meteor.*, Amer. Meteor. Soc., Vail, 255-257.
- Larochelle, B., 1994: Application of the synthetic dual-Doppler technique to an operational Doppler weather radar. M.Sc. thesis, University of Alberta, Edmonton, 138 pp.
- Lewis, J. M., 1971: Variational subsynoptic analysis with applications to severe local storms. *Mon. Wea. Rev.*, **99**, 786-795.
- _____, Y. Ogura, and L. Gidel, 1974: Large-scale influences upon the generation of a mesoscale disturbance. *Mon. Wea. Rev.*, **102**, 545-560.
- Lhermitte, R. M. and D. Atlas, 1961: Precipitation motion by pulse-Doppler radar. *Proc. 9th Conf. on Radar Meteor.*, Kansas City, Amer. Meteor. Soc., 218-223.
- Lin, Y., P. S. Ray, and K. W. Johnson, 1993: Initialization of a modelled convective storm using Doppler-derived fields. *Mon. Wea. Rev.*, **121**, 2757-2775.
- Long, A. B., B. A. Campistron, and A. W. Huggins, 1990: Investigations of a winter mountain storm in Utah. Part I: Synoptic analyses, mesoscale kinematics, and water release rates. *J. Atmos. Sci.*, **47**, 1302-1322.
- Longley, R. W., and C. E. Thompson, 1965: A study of the causes of hail. *J. Appl. Meteor.*,

4, 69-82.

- Matejka, T. J. and R. C. Srivastava, 1991: An improved version of the extended velocity-azimuth display analysis of single-Doppler radar data. *J. Atmos. Oceanic Technol.*, **8**, 453-466.
- Miller, M. J., and R. P. Pearce, 1974: A three-dimensional primitive equation model of cumulonimbus convection. *Quart. J. Roy. Meteor. Soc.*, **100**, 133-154.
- Mueller, C. K., and J. W. Wilson, 1989: Evaluation of the TDWR nowcasting experiment. *Preprints, 24th Conf. on Radar Meteor.*, Tallahassee, Amer. Meteor. Soc., 224-227.
- Newark, M. J., 1984: Canadian tornadoes, 1950-1979. *Atmos. -Ocean*, **22**, 343-353.
- Ogura, Y., M.-T. Liou, and J. Rusell, and S. T. Soong, 1979: On the formation of organized convective systems observed over the eastern Atlantic. *Mon. Wea. Rev.*, **107**, 426-441.
- Purdum, J. F. W., 1982: Subjective interpretations of geostationary satellite data for nowcasting. *Nowcasting*, K. Browning, Ed., Academic press, 149-166.
- Renick, J. H., 1979: The Alberta hail project field operations - Summary report. Alberta Weather Modification Board, Report 10, Alberta Agriculture.
- _____, J. H., and J. B. Maxwell, 1977: Forecasting hailfall in Alberta. *Met. Monogr.*, **38**, Amer. Meteor. Soc., Boston, 145-151.
- Reuter, G. W., and Nguyen 1993: Organization of cloud and precipitation in an Alberta storm. *Atmos. Res.*, **30**, 127-141.
- Rogers, R. R., and N. K. Sakellariou, 1986: Precipitation production in three Alberta thunderstorms. *Atmos. Ocean*, **24**, 145-168.
- Rotunno, R., J. B. Klemp, and M. R. Weisman, 1988: A theory for strong, long-lived squall lines. *J. Atmos. Sci.*, **45**, 463-485.
- Shapiro, A., S. Ellis, and J Shaw, 1995: Single-Doppler velocity retrieval with Phoenix II data: clear-air and microburst wind retrieval in the planetary boundary layer. *J. Atmos. Sci.*, (in press).
- Sikdar, D. N., and D. Fox, 1983: An evolving severe storm complex during SESAME: its large scale environment and momentum budget. *Preprints, 13th Conf. on Severe*

- Local Storms*. Amer. Meteor. Soc., 312-315.
- Smith, S. D., and R. M. Rabin, 1989: Estimation of divergence in the prestorm boundary layer. *J. Atmos. Oceanic Technol.*, **6**, 459-475.
- Smith, S. B., and M. K. Yau, 1993a: The causes of severe convective outbreaks in Alberta. Part I: A comparison of a severe outbreak with two non-severe events. *Mon. Wea. Rev.*, **121**, 1099-1125.
- _____, and _____, 1993b: The causes of severe convective outbreaks in Alberta. Part II: Conceptual model and statistical analysis. *Mon. Wea. Rev.*, **121**, 1126-1133.
- Smolarkiewicz, P., and T. L. Clark, 1985: Numerical simulation of the evolution of a three-dimensional field of cumulus clouds. Part I: Model description, comparison with observations, and sensitivity studies. *J. Atmos. Sci.*, **42**, 502-522.
- Srivastava, R. C., T. J. Matejka, and T. J. Lorello, 1986: Doppler radar study of the trailing anvil region associated with a squall line. *J. Atmos. Sci.*, **43**, 356-377.
- Strong, G. S., 1985: *The Limestone Mountain Experiment, July 1985 (LIMEX-85). Part I: Scientific planning: hypothesis and objectives*. Unpublished document. Resource Technologies. Dept., Alberta Research Council, Edmonton, Alberta, 10 pp.
- Sun, J., D. W. Flicker and D. K. Lilly, 1991: Recovery of three-dimensional wind and temperature fields from simulated single Doppler radar data. *J. Atmos. Sci.*, **48**, 876-890.
- _____, and N. A. Crook, 1994: Wind and thermodynamic retrieval from single-Doppler measurements of a gust front observed during Phoenix II. *Mon. Wea. Rev.*, **122**, 1075-1091.
- _____, _____, and L. J. Miller, 1995: Retrieval of the dynamical and microphysical structure of convective storms in CAPE using a cloud model and its adjoint. *Preprints, 27th Conf. on Radar Meteor.*, Amer. Meteor. Soc., Vail, 820-822.
- Tripoli, G. J., and W. R. Cotton, 1980: A numerical investigation of several factors contributing to the observed variable intensity of deep convection over south Florida. *J. Appl. Meteor.*, **19**, 1037-1063.
- Ulanski, S. L., and M. Garstang, 1978: The role of surface divergence and vorticity in the life

cycle of convective rainfall. Part I: Observation and analysis. *J. Atmos. Sci.*, **35**, 1047-1062.

Waldteufel, R., and H. Corbin, 1979: On the analysis of single Doppler data. *J. Appl. Meteor.*, **18**, 532-542

Wilson, J. W., and W. E. Schreiber, 1986: Initiation of convective storms at radar-observed boundary-layer convergence lines. *Mon. Wea. Rev.*, **114**, 2516-2536.

CHAPTER 2

DIVERGENCE PROFILE DERIVATION IN STRATIFORM PRECIPITATION USING THE EVAD ALGORITHM

2.1 Introduction

The technique used most commonly for analysing the velocity measurements from a single Doppler radar is the Velocity Azimuth Display (VAD, Lhermitte and Atlas 1961, Caton 1963, Browning and Wexler 1968). From the VAD analysis, the horizontal mean wind and deformation can be estimated in a uniform wind field. However, information about horizontal divergence is obtained only when the fall speed of hydrometeors is known. To estimate the divergence without the knowledge of particle fall speed, the Extended VAD (EVAD, Srivastava et al. 1986, Matejka and Srivastava 1991) technique is developed. The EVAD method is applicable for fairly uniform wind fields without significant gaps in radar echo regions. The Doppler velocity data over the entire range of azimuths and several elevation angles are needed for the EVAD analysis.

Srivastava et al. (1986) used the EVAD method to infer the divergence in the stratiform region of a prefrontal squall line system. Their divergence profiles were similar to those obtained from the analysis of rawinsonde data in tropical systems and in the mid-latitude system described by Ogura and Liou (1980). Moreover, the EVAD-deduced kinematic structures of wind field agreed well with those calculated from the multiple-Doppler radar analysis. However, accuracy of the EVAD estimates is closely related to the radar scanning protocol used for the EVAD analysis (Matejka and Srivastava 1991). They suggested that weighting data from different elevation angles and using weighted regressions could improve the quality of kinematic estimates.

In this chapter, the EVAD technique is applied to the radial velocity data sampled by the Carvel Doppler radar. Kinematic properties of wind field for a long-lasting

stratiform rain event which occurred in Alberta on 23 June 1993 are retrieved and analysed. Since the Carvel Doppler radar collects data only at three low elevation angles (0.5°, 1.5° and 3.5°), such scans impose restrictions on the use of the EVAD analysis because a fairly wide range of elevation angles is needed for the EVAD analysis (Matejka and Srivastava 1991). Thus, before the investigation is made for the case study on 23 June 1993, the EVAD analysis is first performed in a simulated wind field to investigate how the estimate accuracy is affected by radar parameters.

In section 2.2, details about the EVAD technique are presented. Error analyses in the simulated wind field are discussed in section 2.3. Emphasis is placed on examining the sensitivity of the divergence estimate to a) measurement errors in Doppler velocity; b) radar maximum elevation angle; c) radius of the analysis cylinder; and d) fall speed of hydrometeors. The EVAD analyses for the case on 23 June 1993 are carried out in section 2.4. Conclusions for this chapter are summarized in section 2.5.

2.2 The EVAD Technique

2.2.1 The VAD analysis

The EVAD method is an extension of the VAD technique which will be described first. Figure 2.1 shows the essential geometry of the wind detected by the radar beam which is pointing at an elevation angle α with respect to the ground. The centroid of the sampling bin has coordinates (r, α, φ) with r denoting radar range and φ the radar azimuth measured clockwise from the north. Along the radar beam, the Doppler velocity, V_r , at a point (r, α, φ) is given by

$$V_r(r, \alpha, \varphi) = (u \cos\varphi + v \sin\varphi) \cos\alpha + W \sin\alpha \quad (2.1)$$

where u , v are wind components along the x (eastward) and y (northward) directions, respectively. $W = w - V_f$ is the effective vertical motion of scattering particles with w denoting air vertical motion and V_f the terminal fall speed of the particles.

When the wind field is smooth, its local spatial variation can be assumed to be linear in the horizontal dimensions. Thus the wind field inside the observed domain can be

described by the sum of the value at the circle centre and the first derivatives (e.g., Browning and Wexler 1968):

$$\begin{aligned} u &= u_o + u_x x + u_y y \\ v &= v_o + v_x x + v_y y \end{aligned} \quad (2.2)$$

where the subscript “o” denotes the value at the centre of the circle being scanned, and subscripts “x”, “y” and “z” denote partial derivatives. By substituting (2.2) into (2.1), and using the transformation from rectangular (x,y,z) to spherical coordinates (r,α,φ)

$$\begin{aligned} x &= r \cos\phi \cos\alpha \\ y &= r \sin\phi \cos\alpha \\ z &= r \sin\alpha \end{aligned} \quad (2.3)$$

the radial wind component V_r is given by

$$\begin{aligned} V_r(r,\alpha,\phi) &= \frac{1}{2} r \cos^2\alpha (u_x + v_y) + W \sin\alpha \\ &+ v_o \cos\alpha \sin\phi \\ &+ u_o \cos\alpha \cos\phi \\ &+ \frac{1}{2} r \cos^2\alpha (u_y + v_x) \sin 2\phi \\ &+ \frac{1}{2} r \cos^2\alpha (u_x - v_y) \cos 2\phi . \end{aligned} \quad (2.4)$$

Provided V_r is smooth, we can write V_r as a Fourier series in terms of the variable ϕ . Truncating this series to keep only the first (leading) five terms, we have the approximation:

$$V_r(r,\alpha,\phi) = a_o + a_1 \sin\phi + a_2 \cos\phi + a_3 \sin 2\phi + a_4 \cos 2\phi . \quad (2.5)$$

According to the orthogonal characteristics of trigonometric function, the Fourier coefficients, a_m ($m=0,\dots,4$), can be determined uniquely by

$$a_m(r, \alpha) = \begin{cases} \sum_{i=1}^N V_r(r, \alpha, \varphi_i) & m=0 \\ \sum_{i=1}^N V_r(r, \alpha, \varphi_i) \sin \varphi_i & m=1 \\ \sum_{i=1}^N V_r(r, \alpha, \varphi_i) \cos \varphi_i & m=2 \\ \sum_{i=1}^N V_r(r, \alpha, \varphi_i) \sin 2\varphi_i & m=3 \\ \sum_{i=1}^N V_r(r, \alpha, \varphi_i) \cos 2\varphi_i & m=4 \end{cases} \quad (2.6)$$

where N is the total number of the velocity measurements around one VAD ring (azimuth varying from 0° to 360°). By comparing (2.4) and (2.5), the Fourier coefficients are related to kinematic parameters as

$$a_0 = \frac{1}{2} r \cos^2 \alpha (u_x + v_y) + W \sin \alpha \quad (2.7)$$

$$a_1 = v_o \cos \alpha$$

$$a_2 = u_o \cos \alpha$$

$$a_3 = \frac{1}{2} r \cos^2 \alpha (u_y + v_x) \quad (2.8)$$

$$a_4 = \frac{1}{2} r \cos^2 \alpha (u_x - v_y) .$$

For one horizontal circle (i.e., a single VAD ring), r and α are both constants. So, kinematic properties of a local wind field, such as mean wind components u_o and v_o , stretching deformation $(u_x - v_y)$ and shearing deformation $(u_y + v_x)$, can be derived directly from the Fourier coefficients a_1 to a_4 in (2.8). However, in (2.7), the divergence ($DIV = u_x + v_y$) is contaminated by the vertical motion of particles (W), and cannot be directly calculated from a_0 . The VAD technique determines DIV on the basis of assuming a zero contribution of W to a_0 . Browning and Wexler (1968) found that this requirement can be met when radar scans at low elevation angles ($\alpha < 7^\circ$) as in such case the particle vertical motion, W , contributes insignificantly to the radial component (see Figure 2.1).

2.2.2 The EVAD technique

To determine the divergence without the knowledge of W , the EVAD method is adopted. In extensive precipitation areas where the EVAD method is used, the vertical component of the air velocity, w , is negligible compared to the terminal fall speed of hydrometeors, V_r , i.e., $W = w - V_r \approx -V_r$. Hence, (2.7) is rewritten as

$$\frac{2a_o}{L \cos\alpha} = DIV - V_r \frac{2 \sin\alpha}{L \cos\alpha} \quad (2.9)$$

where $L = r \cos\alpha$ is the radius of one VAD ring, and also the horizontal range from the radar. In the volume scan by a radar (see Figure 2.2), each a_o , determined by (2.6), relates to radar ranges and elevation angles, and formulates a set of values along the vertical axis through the radar site. To estimate DIV and V_r separately we can assume that, in (2.9), the DIV and V_r are functions of height only, that is, they are horizontally uniform. Consider the VAD scans for many paired values of L and α such that the resulting VAD circles lie in a narrow interval of height, over which DIV and V_r are regarded constant within a maximum horizontal range, L_{max} , (see Figure 2.3). Under these conditions, the values of $(2a_o/L \cos\alpha)$ as a function of $(2 \sin\alpha/L \cos\alpha)$ are distributed over a straight line. The slope and intercept of the line determined by least-squares fit yield V_r and DIV estimates simultaneously. These quantities are determined in successive thin-layer sections, in which the assumption of DIV and V_r constant are supposed to be satisfied. In this way, the vertical profiles of DIV and V_r are obtained.

It should be pointed out that for estimating the divergence there is no need to assume that the wind field varies linearly in x and y . It is sufficient to assume u and v to vary quadratically in x and y , respectively, since this still allows the divergence to be horizontally uniform within the analysis domain. Specifically, the linear and quadratic variations in u and v would yield that DIV does not depend upon L (Caya and Zawadzki 1992). This follows from the definition of DIV as the mean divergence within a circle centred over the radar. As L varies, the area of the circle changes quadratically, and equally in all directions, leaving DIV unchanged by quadratic variations in the wind components.

2.2.3 Variable regression

The first step in the EVAD analysis is to perform the VAD analyses on the entire volume of radial velocity data collected by a single-Doppler radar. For each VAD ring, a_o is calculated using (2.6). As a result of the VAD analyses, a_o varies as a function of the ring radius, L , and the elevation angle, α , as given by (2.9).

It is convenient to introduce the notation $Y \equiv 2a_o / L \cos \alpha$; $p_1 = DIV$, $p_2 = -V_t$, $g_1 = 1$, and $g_2 = 2 \sin \alpha / L \cos \alpha$. Let the column vector $p = [p_i]$ and define the column vector q and the matrix P by

$$\begin{aligned} q_i &= \sum_{k=1}^M \gamma_k g_i(\alpha_k, L_k) Y(\alpha_k, L_k) \\ P_{ij} &= \sum_{k=1}^M \gamma_k g_i(\alpha_k, L_k) g_j(\alpha_k, L_k) \end{aligned} \quad (2.10)$$

where indices $i, j = 1, 2$, and the summations range over the M rings in the thin layer. The factor γ_k is a weight associated with the k th ring, and is computed by

$$\gamma_k = \frac{L_k^2 \cos^2 \alpha_k}{4n_k \text{Var}(a_o)_k} \quad (2.11)$$

where $\text{Var}(a_o)$ is the estimated variance of a_o , defined by (Draper and Smith 1966, p.88)

$$\text{Var}(a_o) = \frac{1}{N-5} \sum_{i=1}^N [V_r(\varphi_i)_{obs} - V_r(\varphi_i)_{est}]^2 . \quad (2.12)$$

In (2.11), n_k denotes the number of rings that belong to the same elevation cone as ring k and that are also in the same horizontal layers as ring k . The weighted least-squares solution for the coefficients p_i (i.e., DIV and V_t) is

$$p = P^{-1} q . \quad (2.13)$$

The reason for using the weighted regressions (2.10) instead of regular regressions

is that the radar collects data at finite interval along the radar beam rather than at a continuous pattern. Consequently, lower elevation cones contribute more rings to a layer than higher elevation cones for low-levels (see Figure 2.3). This leads to an exaggerated contribution to the regression by data from greater ranges. The inclusion of γ_k in (2.10) restrains this effect for the finite thickness of the layers (Matejka and Srivastava 1991).

2.3 Examination of the EVAD Analysis in a Simulated Wind Field

The EVAD analysis is based on processing radial velocity measurements, and involves the VAD regressions from different elevation angles within a vertical cylinder of radius, L_{max} . Therefore, the effects of the uncertainty in V_r measurements on the accuracy of the divergence estimates needs to be determined. Likewise, how the radar maximum elevation angle and the cylinder radius L_{max} affect the profile of DIV has also to be evaluated. Finally, we examine the impact of the particular choice of the terminal fall speed of hydrometeors on the divergence estimates.

2.3.1 Influence of measurement errors in Doppler velocity

To study the influence of inaccuracies inherent in radial velocity measurements on the divergence estimate, sensitivity analyses are carried out for a simulated wind field. The wind field is simulated by specifying mean wind components and their first derivatives over the radar site according to (2.2). The values of u_o and v_o are set to be constant, but u_x , u_y , v_x and v_y are assumed to vary linearly with height. Specifically, we assume the following conditions:

$$u_o = 10 \text{ ms}^{-1}$$

$$v_o = 8 \text{ ms}^{-1}$$

$$u_x = v_x = \begin{cases} -0.8 \times 10^{-4} z + 1.7 \times 10^{-4} & z \leq 5 \text{ km} \\ 1.2 \times 10^{-4} z - 9.0 \times 10^{-4} & 5 \text{ km} < z \leq 7.5 \text{ km} \\ 1.1 \times 10^{-5} z - 0.8 \times 10^{-4} & z > 7.5 \text{ km} \end{cases} \quad (2.14)$$

$$u_y = v_y = \begin{cases} -0.6 \times 10^{-4} z + 1.3 \times 10^{-4} & z \leq 5 \text{ km} \\ 0.4 \times 10^{-4} z - 3.0 \times 10^{-4} & 5 \text{ km} < z \leq 7.5 \text{ km} \\ 2.2 \times 10^{-5} z - 1.7 \times 10^{-4} & z > 7.5 \text{ km} \end{cases}$$

Here z denotes the height in km, and u_x , u_y , v_x , and v_y are partial derivatives of wind components in s^{-1} . From (2.14), the divergence profile in the simulated wind field is given by:

$$DIV = \begin{cases} -1.4 \times 10^{-4} z + 3.0 \times 10^{-4} & z \leq 5 \text{ km} \\ 1.6 \times 10^{-4} z - 1.2 \times 10^{-3} & 5 \text{ km} < z \leq 7.5 \text{ km} \\ 3.3 \times 10^{-5} z - 2.5 \times 10^{-4} & z > 7.5 \text{ km} \end{cases} \quad (2.15)$$

It is assumed that air flow is divergent beneath the altitude of 2.1 km, but convergent between 2.1 and 7.5 km, and divergent again above 7.5 km. This convergent / divergent flow structure is a typical profile found in mesoscale convective systems (Ogura and Liou 1980, and Zhang et al. 1989).

In meteorology, the measurements of all quantities are subject to uncertainties due to instrument and sampling errors. Velocity measurements by Doppler radar are no exception. In fact, the uncertainty of Doppler velocity measurements is about 10 to 30% of their true values (Doviak and Zmic 1993). To treat this uncertainty, we assume that the wind field given by (2.14) is affected by random errors. Specifically, each Doppler velocity measurement is assumed to have a random perturbation. These errors are spatially uncorrelated. Thus,

$$V_r = V_{ro} + A_p \cdot (\delta - 0.5) \quad (2.16)$$

where $\langle V_r \rangle$ is the expected value of V_r , and $\langle V_r \rangle = V_{rn}$. The second term on the RHS of (2.16) is associated with the statistical uncertainty in the V_r measurement made by the Doppler radar. $A_p = [\langle (V_r - V_{rn})^2 \rangle]^{1/2}$ denotes the magnitude of errors in radial velocity. δ is an uncorrelated random variable whose probability density function is uniform over the $[0, 1]$ interval. Simulated Doppler velocity data are computed every 450 m along the radar beam from sweeps at five elevation angles (0.5°, 11.9°, 23.9°, 37.1°, and 53.3°, see Figure 2.3). The radius of analysis cylinder, L_{max} , is set at 60 km, and layers of 300 m in depth (Δz) are used. The terminal fall speed of raindrops, V_p , in (2.9) is assumed to be 3.0 ms⁻¹ over all layers.

Figure 2.4 and Figure 2.5 illustrate the vertical profiles of the deviation of the divergence estimate from its real value when different A_p and δ values are selected. The departure of the estimated divergence from its original value is represented by the relative error, $\Delta DIV\%$, which is defined as $|DIV_{real} - DIV_{est.}| / DIV_{real} \times 100\%$. Over the layers of 7 km, $\Delta DIV\%$ becomes larger when the A_p value is increased (Figure 2.4). This indicates that the inaccuracy of the divergence estimate increases with the measurement errors in radial velocity. With the height, $\Delta DIV\%$ repeatedly increases as the largest VAD ring from a low elevation vacates the analysis cylinder. The large spike around 1.0 km occurs where the lowest elevation cone drops out and the largest ring is supplied by the second elevation cone. This spike is caused by the few low elevation angles that can be used (only one elevation lower than 1° here), and could be eliminated by spacing the lower elevations more closely. The curves shown in Figure 2.4 indicate that relative errors in divergence estimates are less than 12% when the inaccuracy in V_r measurements is smaller than 28% (i.e., $A_p = 5.0$ ms⁻¹).

Figure 2.5 shows the $\Delta DIV\%$ profiles when δ is “picked” at random between 0 and 1 and $A_p = 6.0$ ms⁻¹. The small discrepancies among the six $\Delta DIV\%$ curves suggest that the divergence estimate is not sensitive to the value of δ . The contribution of δ to the $\Delta DIV\%$ is less than 4%.

2.3.2 Influence of the highest elevation angle

Since the EVAD technique uses the VAD rings from a wide range of elevation angles, Doppler velocity scans at limited elevation angles, such as by the Carvel radar, could impose restrictions on the use of the EVAD analysis. In this section, we investigate how the *DIV* estimate depends on the upper limit of elevation angles. Six scan designs with a maximum elevation angle (α_{max}) as 3°, 5°, 10°, 20°, 40°, and 60° are evaluated. Each scan design consists of different sweeps with $\Delta\alpha=1^\circ$ for $\alpha_{max}=3^\circ, 5^\circ, 10^\circ$, and $\Delta\alpha=2^\circ$ for $\alpha_{max}=20^\circ, 40^\circ, \text{ and } 60^\circ$. The numbers of sweeps in the six scan designs are thus 3, 5, 10, 10, 20 and 30, respectively. Data coverages for the six designs are depicted in Figure 2.6. The simulated wind field given by (2.14) is adopted. The estimated uncertainty in V_r is assumed to be $A_p=3.0 \text{ ms}^{-1}$. The analysis cylinder radius, L_{max} , is taken as 60 km.

Variations of $\Delta DIV\%$ versus height for the six α_{max} designs are shown in Figure 2.7. In Figure 2.7a, the EVAD analysis yields the precise divergence estimate ($\Delta DIV\% < 10\%$) only below 1.8 km when radar elevations are restricted lower than 3°. For the α_{max} of 5° and 10°, the altitudes for estimating the divergence (within a 50% relative error) are raised to 2.4 and 5.7 km, respectively (neglecting the large spike around 2.2 km). It is possible to deduce the divergence up to 7.5 km when the maximum elevation angles of radar sweeps are higher than 20° (Figure 2.7b). Below 1.0 km, $\Delta DIV\%$ increases when the interval of elevation angles, $\Delta\alpha$, is increased from 1° ($\alpha_{max} \leq 10^\circ$) to 2° ($\alpha_{max} \geq 20^\circ$). This feature suggests that errors in estimating the divergence could be reduced by using more elevation angles at a finer elevation step.

For the Carvel Doppler radar, radial velocity data are taken only at three low elevation angles (0.5°, 1.5° and 3.5°). Figure 2.7a suggests that, for $\alpha_{max} \approx 3^\circ$, the EVAD analysis can yield accurate divergence estimates up to 2.0 km when the measurement errors in radial velocity are 16% (i.e., $A_p=3.0 \text{ ms}^{-1}$) and the analysis radius is 60 km.

2.3.3 Influence of analysis cylinder radius

Matejka and Srivastava (1991) pointed out that the accuracy of the EVAD results depends on the radius of the analysis cylinder, particularly when higher elevation angles

are not used. Considering the limited sweeps at a few elevation angles made by the Carvel radar, we need to find an appropriate L_{max} . Beyond this analysis radius, the divergence can be estimated accurately and the EVAD analysis can be applied to the radial velocity measurements for the Carvel radar configuration.

Analyses with different L_{max} are carried out in the simulated wind field give by (2.14) with $A_p=6.0 \text{ ms}^{-1}$. Radial velocity data are computed at 0.5° , 1.5° , and 3.5° , the three elevation angles used by the Carvel radar. Figure 2.8 shows the $\Delta DIV\%$ profiles when the radii of analysis cylinder, L_{max} , are 40, 60, 80, and 100 km, respectively. Larger analysis radius raises the permissible altitude (denoted by Z_{TOP}), below which the divergence can be estimated with $\Delta DIV\%$ less than 50%. For example, $Z_{TOP}=1.2$ km when L_{max} is 40 km, while Z_{TOP} can be increased to 2.4 km for $L_{max}=100$ km. To estimate the divergence profile to the altitude of $Z_{TOP} = 1.8$ km, the radius of an analysis cylinder should be at least 60 km for the Carvel radar.

2.3.4 Influence of hydrometeor fall speed

In this section, we investigate the effect of the terminal fall speed of the hydrometeors (e.g., raindrops) on estimating the EVAD divergence values. To quantify this, we will compare the results for two conditions. In the first, the fall speed remains constant over the entire vertical layers, whereas in the second, the fall speed varies linearly with height. Specifically, we have:

$$\text{Condition I:} \quad V_r = 3.0 \text{ ms}^{-1} ; \quad (2.17)$$

$$\text{Condition II:} \quad V_r = 3.0 - 0.22z \text{ ms}^{-1}. \quad (2.18)$$

In (2.18), z is height in km. For widespread precipitation, evaporation of raindrops below cloud base is of no concern. So, the relationship in Condition II is an attempt to model the increase in raindrop size when the falling raindrops grow by collecting smaller drops through the coalescence process. In both conditions, the wind field is given by (2.14).

Profiles of $\Delta DIV\%$ for Conditions I and II (Figure 2.9) are very similar. This

implies that the EVAD-deduced divergence estimate is indeed insensitive to the specific variation in the hydrometeors fall speed. This conclusion supports the findings of Srivastava et al. (1986): the EVAD analysis can provide the divergence estimate without knowledge of V_r . The large spike at the altitude of about 1 km is artificial, reflecting the improper arrangement of sweeps at low elevation angles. This spike could be eliminated when applying the EVAD analysis to actual velocity data sampled by the Carvel radar because enough low elevation angles are used.

2.4 Application of the EVAD Analysis on 23 June 1993

2.4.1 Synoptic situation

On 22 June 1993, a mid-latitude cyclone developed, spanning the region from western British Columbia to central Manitoba. A complex, slow moving, low pressure system moved over central Alberta and produced abundant precipitation. Along the northern foothills of the Rocky Mountains, rainfall amounts exceeded 50 mm. On 23 June, an additional 30 mm of rain was brought to the most northern and central regions of Alberta with some stations recording up to 180 mm. This resulted in local flooding in northern Alberta. The lowest station pressure in Edmonton in 113 years (91.13 kPa) was recorded on this day.¹

Synoptic conditions on 23 June 1993 are shown in Figure 2.10. The dominant 500-mb feature at 0000 UTC 23 June 1993 (Figure 2.10a) was a cold low over southern Alberta. A trough of warm air aloft (TROWAL) wrapped around the low centre, and the warm air was southeastward being advected from southern Manitoba. On the surface map (Figure 2.10b), the low pressure system was centred at east central Alberta with a northeastward warm front and a southeast-directed cold front. Extensive clouds and rain were produced on and to the rear of the surface cold front.

¹The information was obtained from the *Climatic Perspectives (Monthly Review)* for June 1993, issued by Environment Canada.

2.4.2 *Radar observations of precipitation*

Satellite images suggested that clouds covered most areas of Alberta starting at about 0200 UTC on 22 June 1993. Radar observations showed that the precipitation was fairly uniform between 2300 UTC on 22 June and 0600 UTC on 23 June. Figure 2.11 depicts the 1.5-km CAPPI (Constant Altitude Plan Position Indicator) of rainfall rate at times 0030, 0100, 0200, 0300 and 0400 UTC on 23 June. The image of echo top height at 0030 UTC (Figure 2.11b) is also included to show the upper height of the precipitation field. The echo top varied from 4 to 8 km, averaging at about 6 km. Radar images for rainfall rates were obtained from radar reflectivity by using the Carvel radar Z-R relation: $Z = 295R^{1.43}$.

At 0030 UTC, precipitation was characterized by a northwest-southeast oriented wide zone accompanied by an area with stronger echo cells in the northeast part of the radar display (Figure 2.11a). An echo-free gap formed at the connection of the wide zone and the heavier echo area from azimuths 0° - 20° and ranges 80-220 km. In the following few hours, the precipitation field became smoother as the echo gap diminished and the stronger echo cells weakened. The region scanned by the radar in Doppler mode (its maximum scanning radius of 110 km) was completely covered by uniform precipitation at 0400 UTC. During the period shown in Figure 2.11, the rainfall rate was relatively steady, at around 2 mmh^{-1} at 1.5 km level.

2.4.3 *The EVAD results for 23 June 1993*

a. Data Preprocessing

The EVAD analyses are applied to the Doppler velocity data sampled at times 0030, 0200, 0300 and 0400 UTC on 23 June 1993. Data over the entire azimuths (0° - 360°) and ranges (20-100 km) at three elevation angles of 0.5° , 1.5° and 3.5° are used. The radar data are edited prior to the EVAD kinematics analysis. Detailed procedures for data pre-processing are described in Appendix B.

b. Divergence Estimates

Using the edited velocity data, the VAD analyses are first performed based on (2.6). A set of values consisting of Fourier coefficients a_n to a_4 and the standard variances of the a_n fit is arranged according to the elevation angle (α) and the horizontal range (L) within the radius of an analysis cylinder (L_{max}). These data are then classified into narrow height intervals ($\Delta z=200$ m). The coefficient a_n is used to yield the estimates of DIV and V_r as a function of height. L_{max} was set to 80 km based on the discussion in section 2.3.4.

Figure 2.12 shows the divergence profiles deduced from the EVAD analyses at times (a) 0030, (b) 0200, (c) 0300 and (d) 0400 UTC. Due to the radar scans limited at three low elevation angles, the radial velocity data above 2.4 km were spotty and the EVAD analyses were not applied. Throughout the 3.5 hours of the analyses, the flow pattern displayed similar characteristics. Divergent flow appeared beneath 0.6 km with peak values reaching from $0.7 \times 10^{-4} \text{ s}^{-1}$ to $1.3 \times 10^{-4} \text{ s}^{-1}$. This divergent flow was likely associated with the precipitation fallout below cloud base. Above 0.6 km, the wind field was convergent. The convergence maximum, CON_{max} , varied between $-2.0 \times 10^{-4} \text{ s}^{-1}$ (0200 UTC) and $-6.5 \times 10^{-4} \text{ s}^{-1}$ (0400 UTC). The altitude, at which the convergence reached its maximum, $ZCON_{max}$, fell from 2.2 km to 1.8 km during these 3.5 hours. It should be pointed that large variations in CON_{max} did not correlate with big differences in surface rainfall (see Figure 2.11). This is because the convergence within the layer from 0.6 to 1.7 km remained similar and the $ZCON_{max}$ was too far above the cloud base level.

c. Vertical Velocity Estimates

From the divergence profile, air vertical velocity, w , can be obtained by numerical integration of the continuity equation (incompressible assumption):

$$DIV = \frac{\partial u}{\partial x} + \frac{\partial v}{\partial y} = - \frac{\partial w}{\partial z} , \quad (2.19)$$

where ρ is the air density. Assuming $w|_{z=0} = 0$, the vertical velocity is given by

$$w(z) = - \int_0^z \text{DIV}(z) dz . \quad (2.20)$$

Figure 2.13 shows the profiles of w (from the surface to the altitude of 2.4 km) at times 0030, 0200, 0300 and 0400 UTC. The vertical air motion was downward at low levels but upward aloft. The downdraft, with a maximum varying between 1.5 cms^{-1} and 3.5 cms^{-1} , dominated the layers beneath 1.0 km. It was probably associated with the precipitation fallout below the cloud base. Aloft, air ascended at an updraft speed of a few tens of centimetres per second. Such an updraft speed, supplied by the large low-pressure system, is typical of nimbostratus clouds (Rogers and Yau 1989, p.74). The updraft lasted for a long time ($> 3 \text{ h}$) to produce the widespread, continuous rain. Corresponding to the strongest convergence at 0400 UTC, the resultant peak updraft intensified to around 33 cms^{-1} . However, it contributed little to surface rainfall due to its occurrence at a level much higher than the cloud base.

d. Mean Wind Estimates

Mean values of horizontal wind components, u_o and v_o , can be retrieved from (2.8). Wind derivations for the four times were made. The profiles of u_o and v_o at 0200 UTC are shown in Figure 2.14. Similar profiles were obtained for the other times. Over the vertical depth of 2.7 km, a northwest flow prevailed. In Figure 2.14a, the zonal wind component (u_o) first increased and then decreased with height. The meridional wind component (v_o) increased with height over the lowest 2 km (Figure 2.14b).

To evaluate the EVAD-deduced wind estimate, Figure 2.15 compares the EVAD wind profiles with those obtained from VAD analyses and the 0000 UTC rawinsonde sounding recorded at Stony Plain. There are good agreements among the results from the three sources, especially when comparing the VAD, the 0030 UTC EVAD and the sounding results. A low-level “jet” with a magnitude of 25 ms^{-1} was found around 1.2 km. Wind veered from 290° near the surface to 320° at 2.4 km. The estimates of u_o and v_o from

the EVAD analysis should be more accurate and stable than the VAD result because the VAD analysis was performed using only one elevation angle.

2.5 Conclusions

Kinematic properties of the wind field in stratiform precipitation regions can be deduced from Doppler radar velocity measurements using the EVAD data analysis technique. The EVAD analysis applied to a volume of data in widespread echo areas can estimate vertical profiles of divergence, hydrometeor fall speed, and horizontal wind components. The values obtained are horizontal means over the analysis region which is a vertical cylinder centred over the radar site.

Error analyses were performed in a simulated wind field to examine the effects of specific factors on the EVAD-deduced divergence estimate. Inaccuracy of the divergence estimate was found to increase with the errors in Doppler velocity measurements. When the uncertainty of the radial velocity was 5 ms^{-1} (about 30% of the real V_r value), the errors in estimating the area-averaged divergence were 12% or less beneath 1.5 km, and <10% aloft. The retrieval of the divergence profile crucially depended on the maximum elevation angle and the radius of the analysis cylinder used in the EVAD analysis. Adoption of either higher elevation angles or larger cylinder radius would raise the altitude below which the divergence profile could be derived with high accuracy. For the limited scans used by the Carvel radar, the observing cylinder radius should be at least 60 km so that the divergence estimate up to an altitude of about 2.0 km could be obtained. Experiments in the simulated wind field also showed that the divergence estimate is almost independent of the fall speed of hydrometeors, confirming the results of Srivastava et al. (1986).

Wind kinematic properties in the widespread precipitation of 23 June 1993 were analysed using the EVAD technique at four different times. Divergent air flow occurred beneath 0.6 km, presumably related to the outflow below the cloud base. The wind field aloft was convergent up to the altitude of 2.4 km. The divergent/convergent flow structure was maintained for more than three hours on that day. The convergence caused a weak

but long-lasting ascending motion such produced widespread, continuous rain. Also, we found that the EVAD-derived estimates of horizontal wind agreed reasonably well with those from the VAD analysis and the sounding data recorded at 0000 UTC.

In Chapter 6, the EVAD-derived divergence profile will be used as initial and boundary conditions for an axis-symmetric cloud model. A numerical modelling study will be carried out to simulate this stratiform precipitation event and to investigate the effects of the divergence profile on the development of stratiform precipitation.

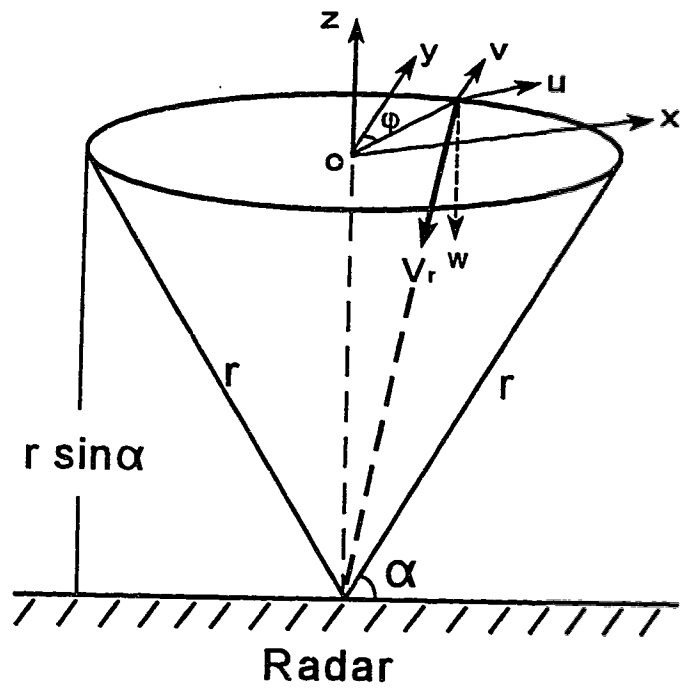


Figure 2.1 Geometry for the scan of velocities on a circle.

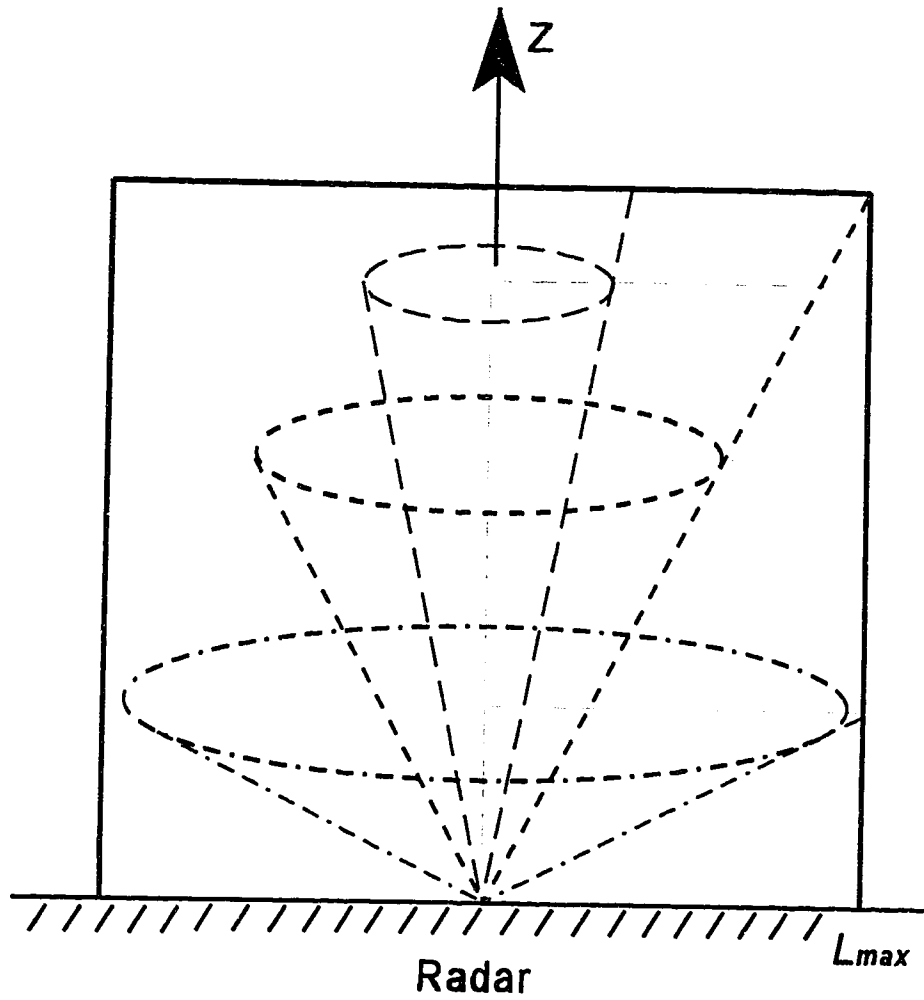


Figure 2.2 The radar volume scans consisting of different elevation angles.

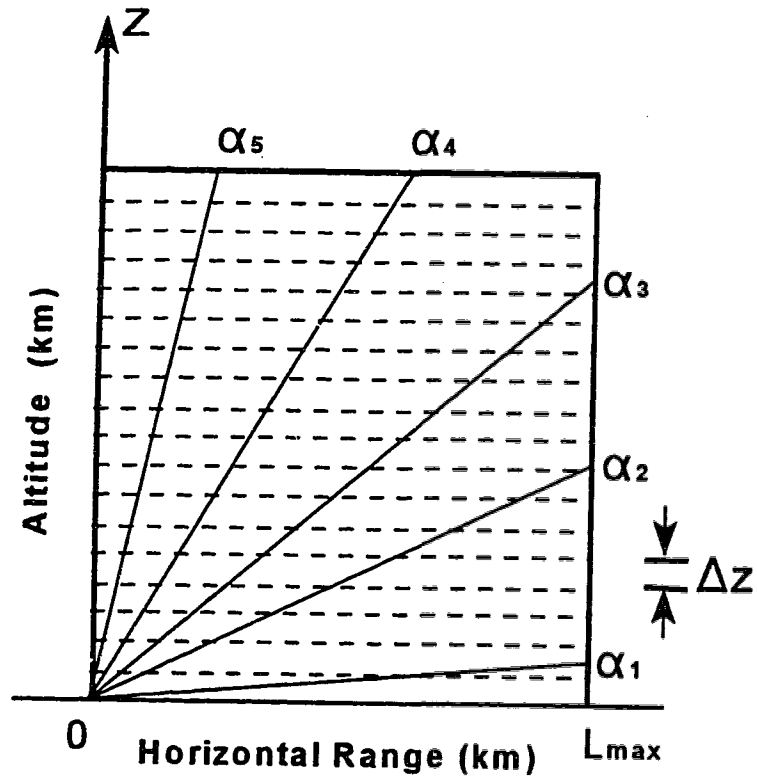


Figure 2.3 Vertical sections depicting the constant-elevation cones of data from various elevation angles for the EVAD analysis.

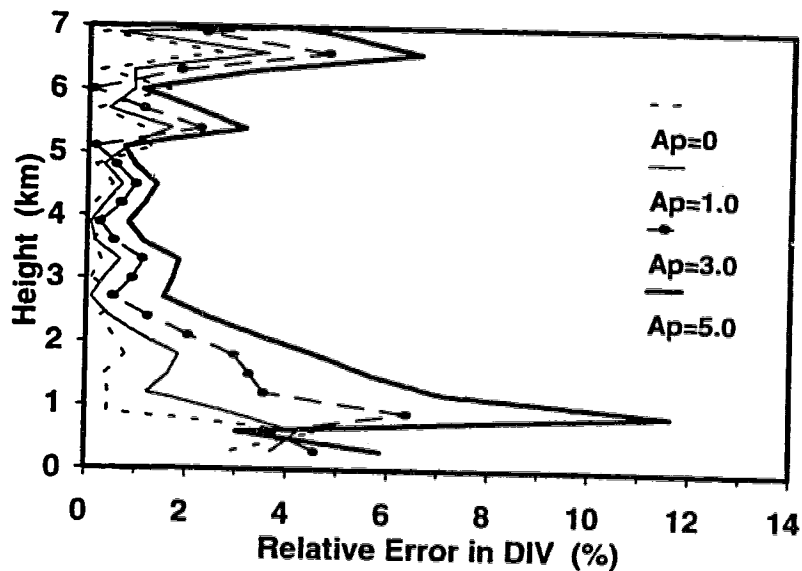


Figure 2.4 Vertical profiles of the relative errors of the EVAD divergence estimate ($\Delta DIV\%$), varying with the amplitude of measurement errors in Doppler velocities, A_p

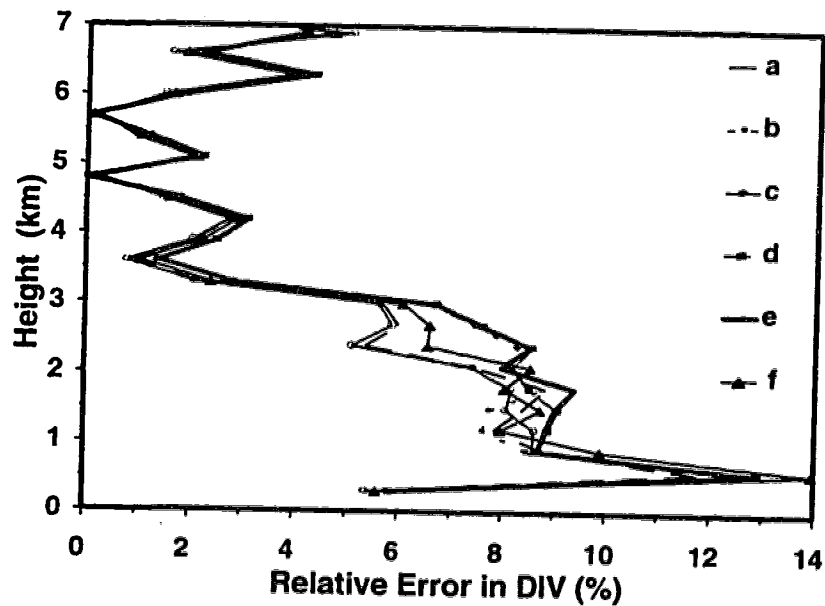


Figure 2.5. The variation of $\Delta DIV\%$ with height. Erroneous Doppler velocities with $A_p = 6.0 \text{ ms}^{-1}$ are randomly produced (denoted by a-f) according to $[0,1]$ uniform probability distribution. Referring to the text for more details.

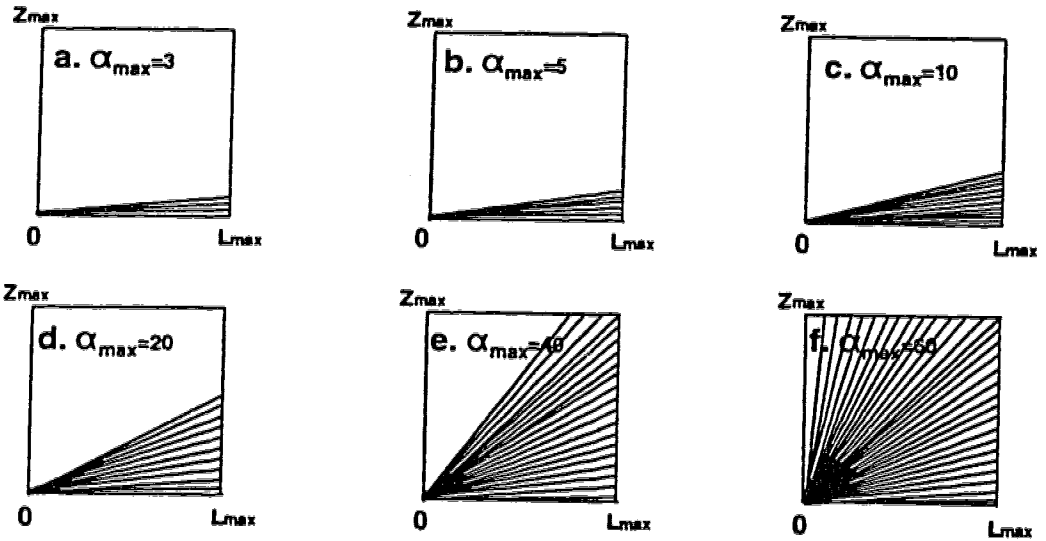


Figure 2.6 Vertical sections depicting the constant-elevation cones of data for various values of Elevation Angle Maximum (α_{max}), and the number of sweeps in the scan.

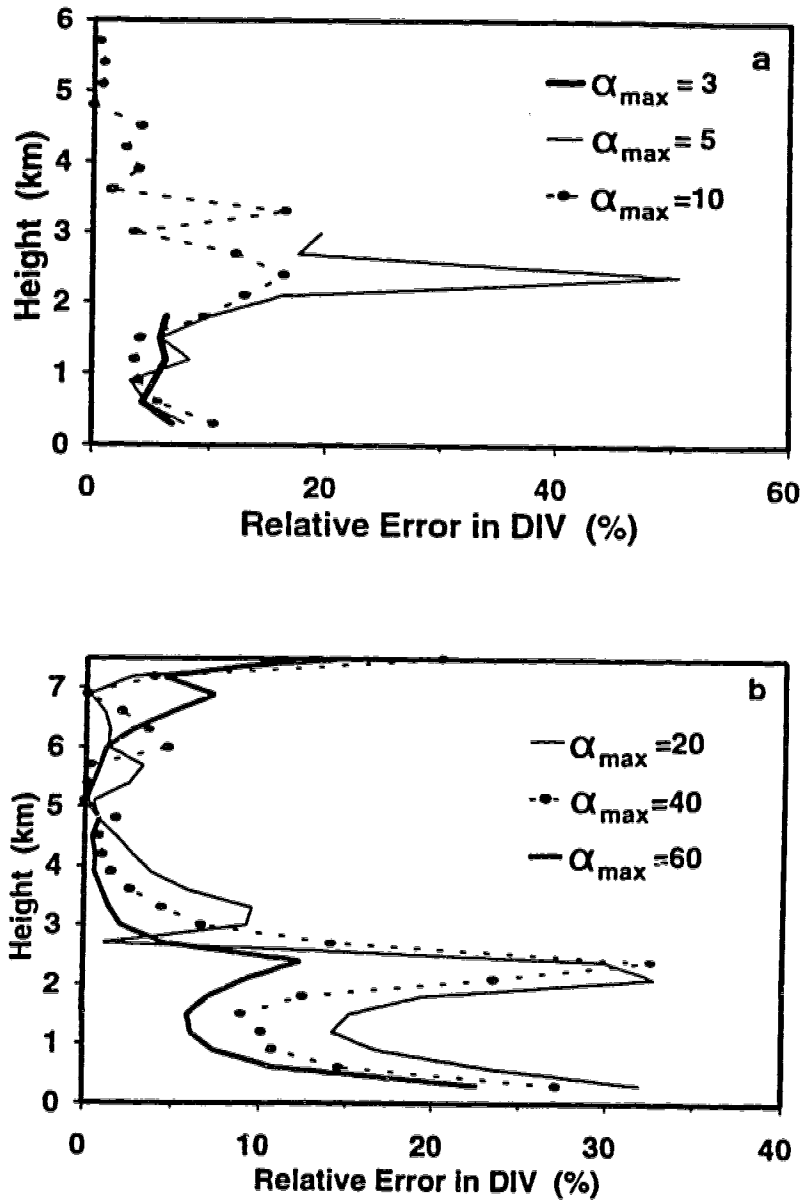


Figure 2.7 The relative errors of divergence estimate ($\Delta DIV\%$) as a function of height, obtained from the EVAD analyses for the six scan designs shown in Figure 2.6. The maximum elevation angles (α_{max}) are (a) 3° , 5° and 10° ; (b) 20° , 40° , and 60° .

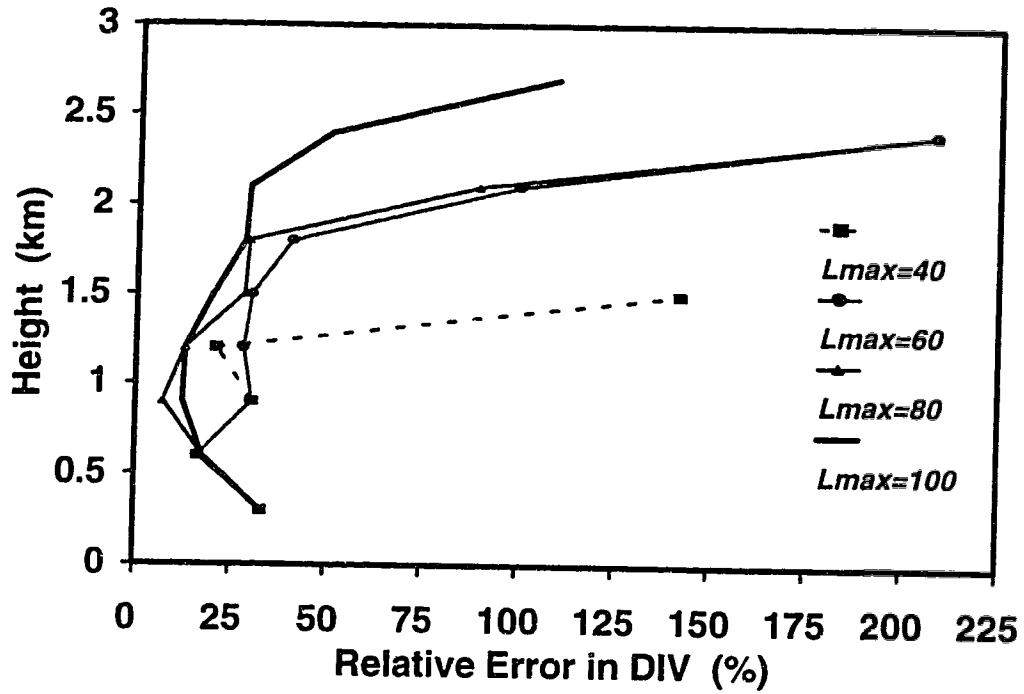


Figure 2.8 The $\Delta DIV\%$ as a function of height, plotted when four radii of analysis cylinder (L_{max} in km) are used. The elevation angles used are same as the Carvel Doppler radar at 0.5° , 1.5° , and 3.5° .

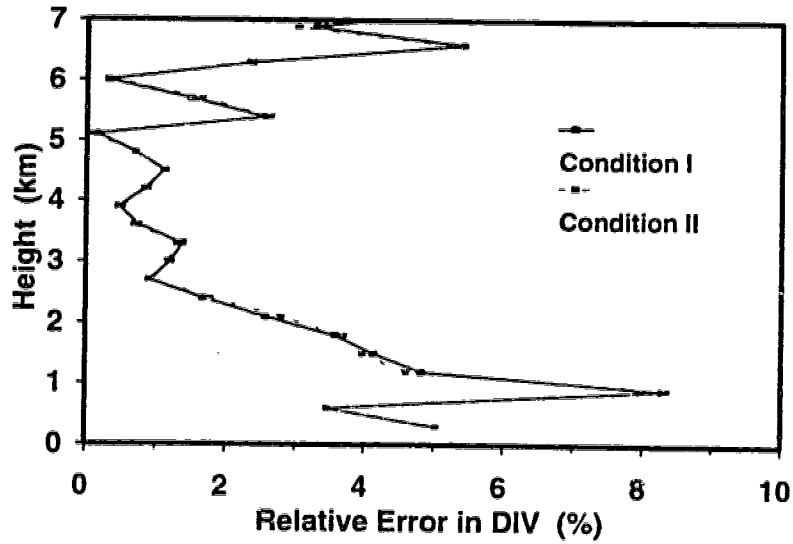


Figure 2.9 Effects of the fall speed of hydrometeors on the EVAD-retrieved divergence estimate. The particle fall speed is assumed constant over the whole layers at Condition I, but to vary linearly with height at Condition II. Vertical profiles of $\Delta DIV\%$ are obtained with $L_{max}=60$ km, and $A_p=3.0$ ms^{-1} .

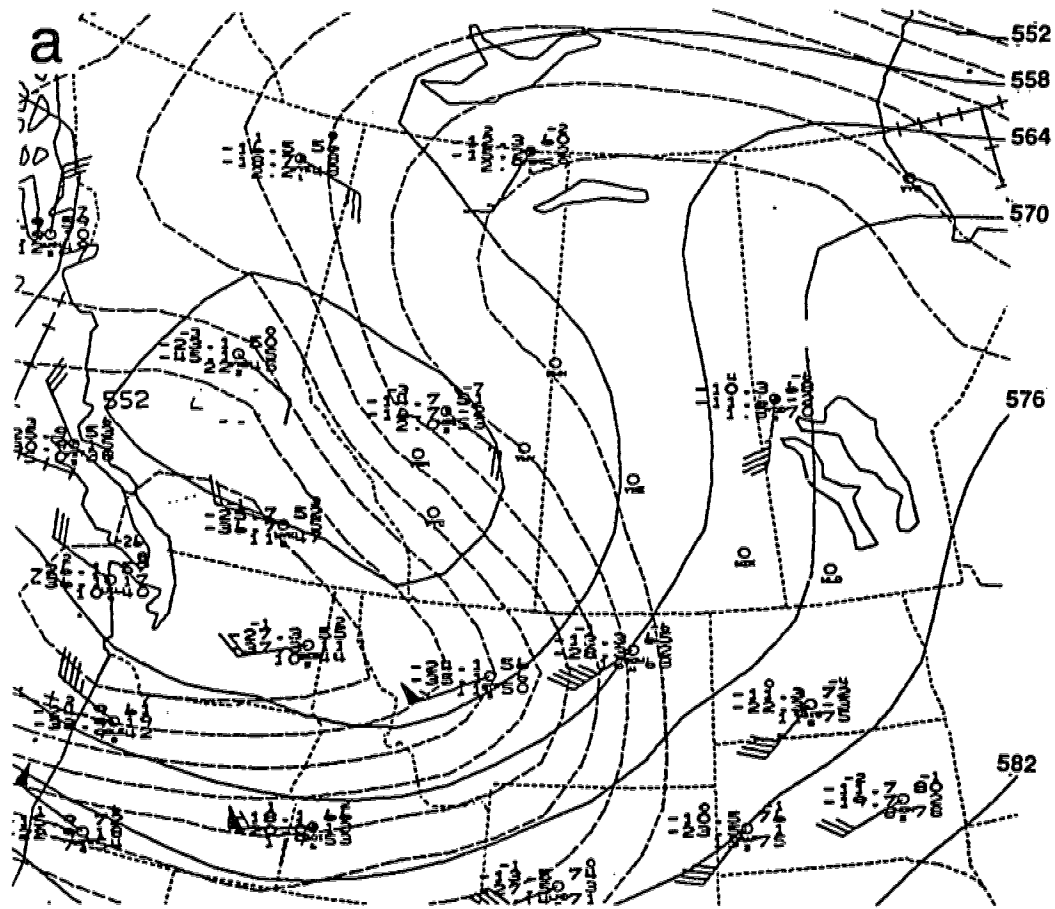


Figure 2.10 (a) 500-mb analysis at 0000 UTC on 23 June 1993. Solid lines are geopotential height contours in decameters while dashed lines are isotherms in °C. Conventional station model used for winds (half bar 5 knots and full bar 10 knots). (b) surface analysis with mean sea level pressure contours in mb.

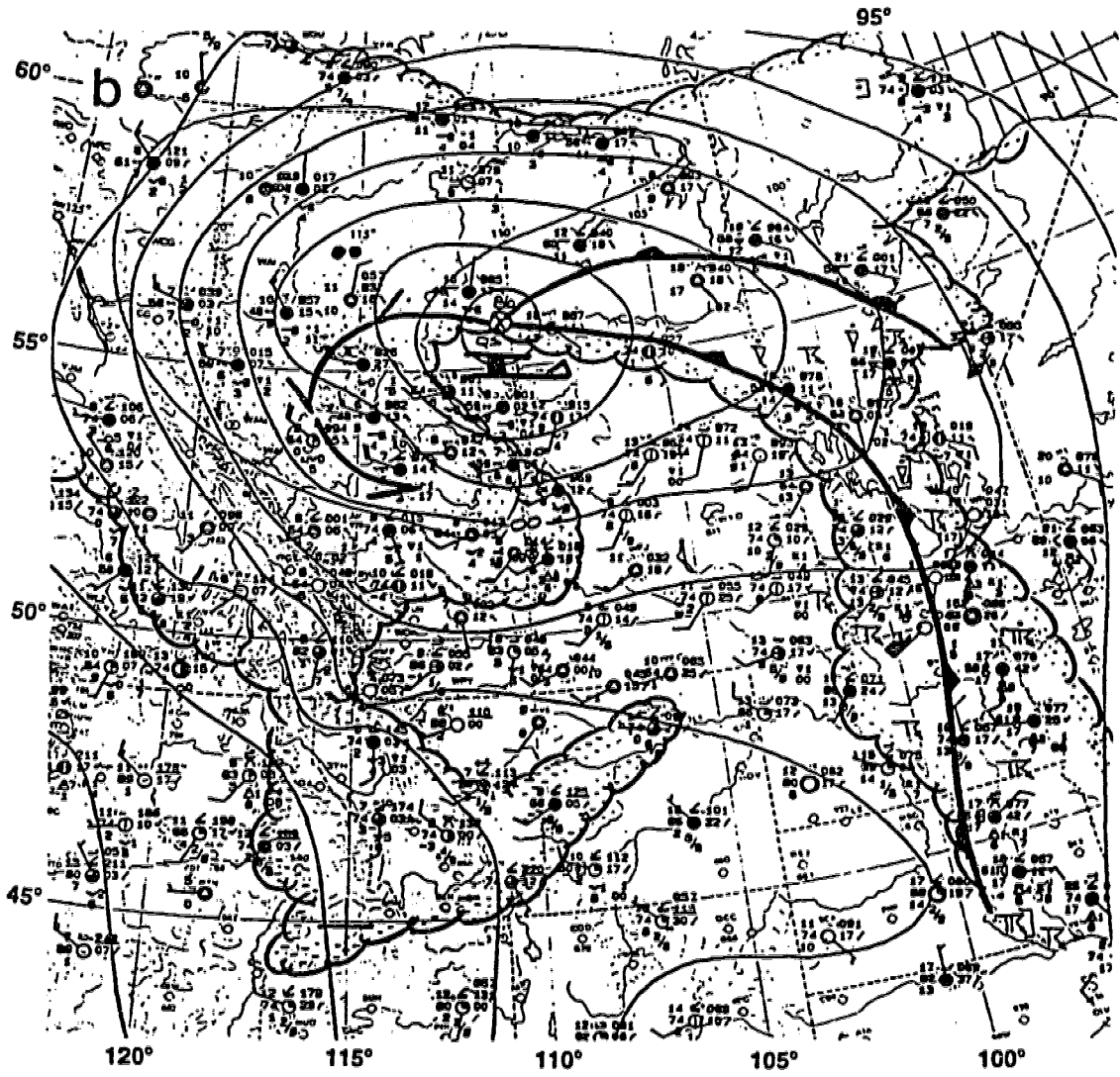


Figure 2.10b.

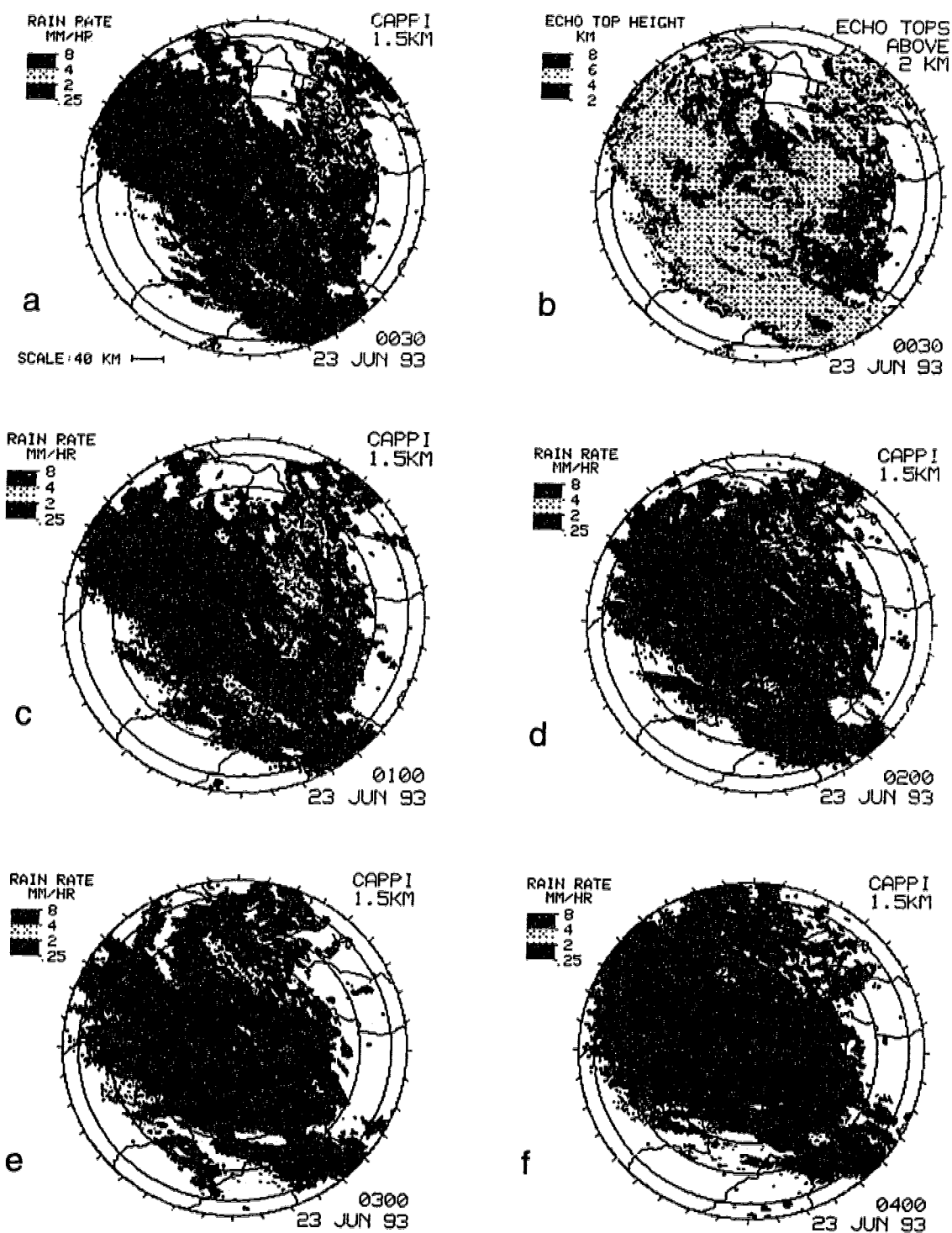


Figure 2.11 Radar observations for 1.5 km-CAPPI of rainfall rate (mmh^{-1}) at (a) 0030, (c) 0100, (d) 0200, (e) 0300, and (f) 0400 UTC; and for (b) echo top height at 0030 UTC on 23 June 1993.

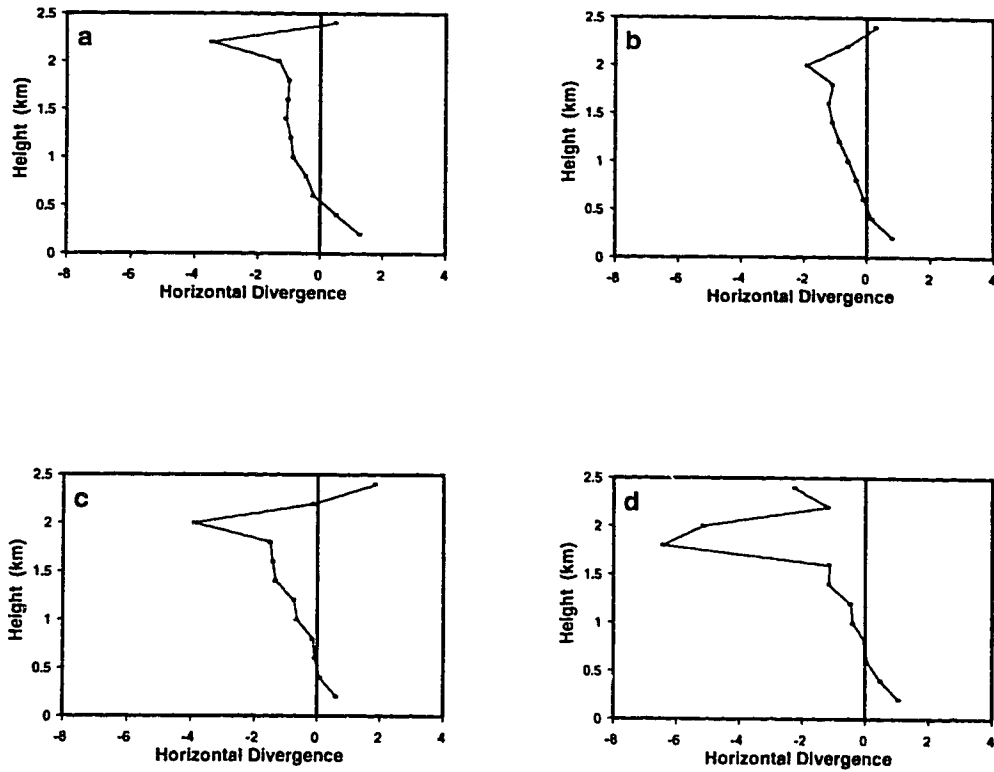


Figure 2.12 Vertical profile of divergence of the horizontal wind from the EVAD analysis at (a) 0030, (b) 0200, (c) 0300, and (d) 0400 UTC. The EVAD analyses are based on data collected by the Carvel Doppler radar on 23 June 1993. The divergence is in unit of $10^{-4} s^{-1}$.

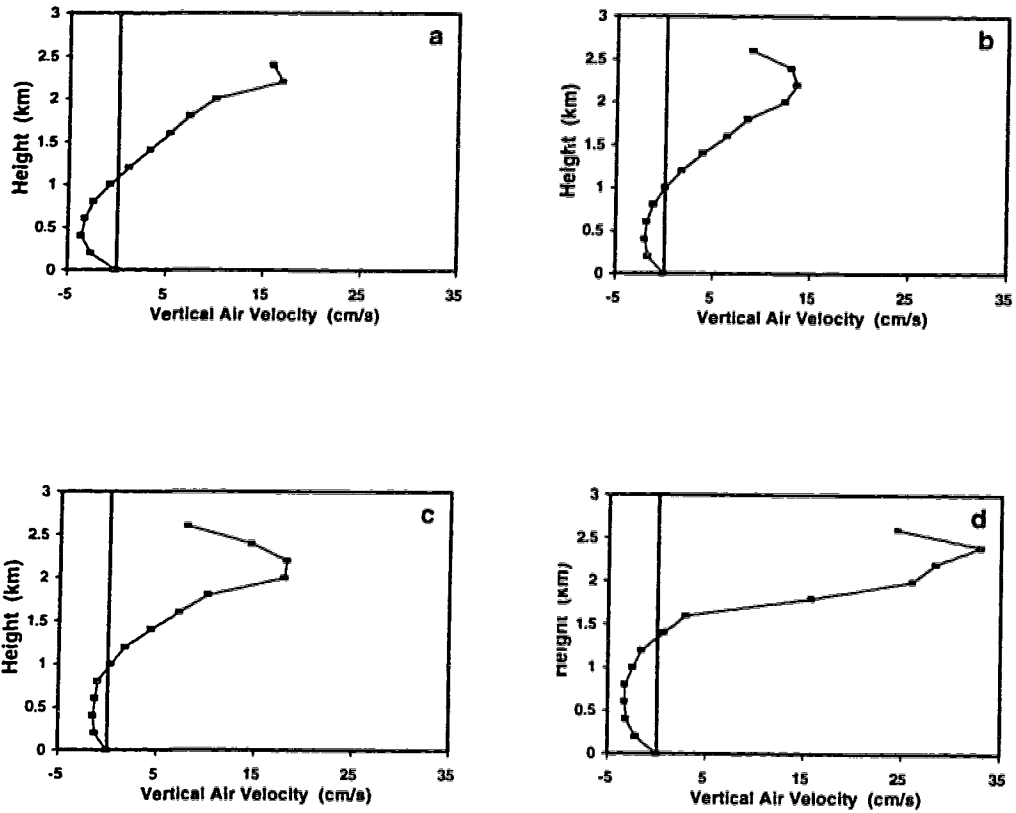


Figure 2.13 Same as Figure 2.12 but for the vertical profile of air vertical velocity. The air vertical velocity is obtained from the integration of the divergence in Figure 2.12 assuming $w=0$ at the surface and $\partial\rho/\partial z=0$.

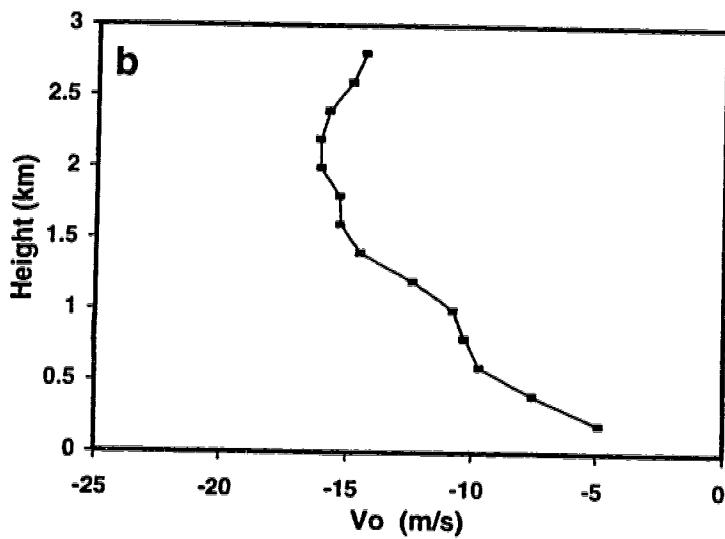
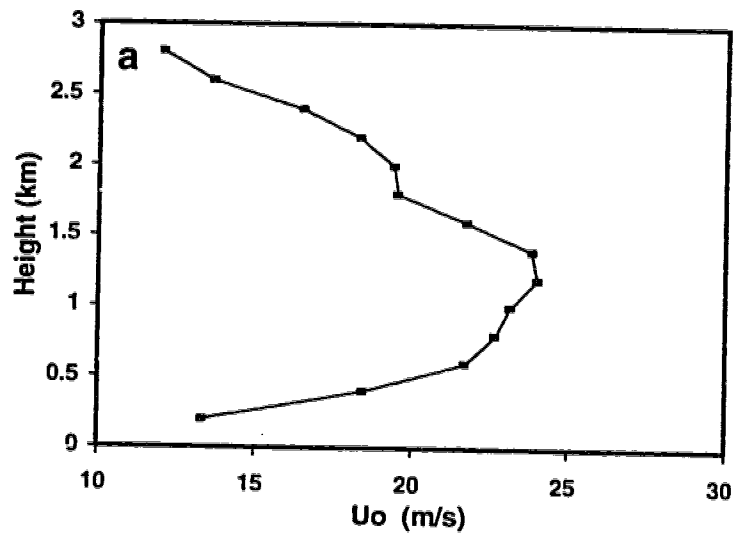


Figure 2.14 Profiles of wind components (a) u_0 , and (b) v_0 , obtained from the EVAD analysis for the observations taken at 0200 UTC on 23 June 1993. The radius of analysis cylinder used in the EVAD analysis is 80 km.

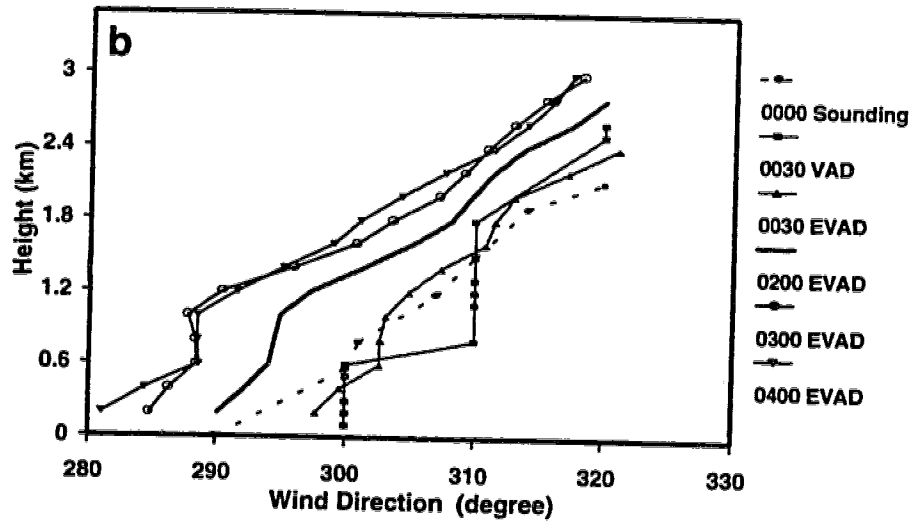
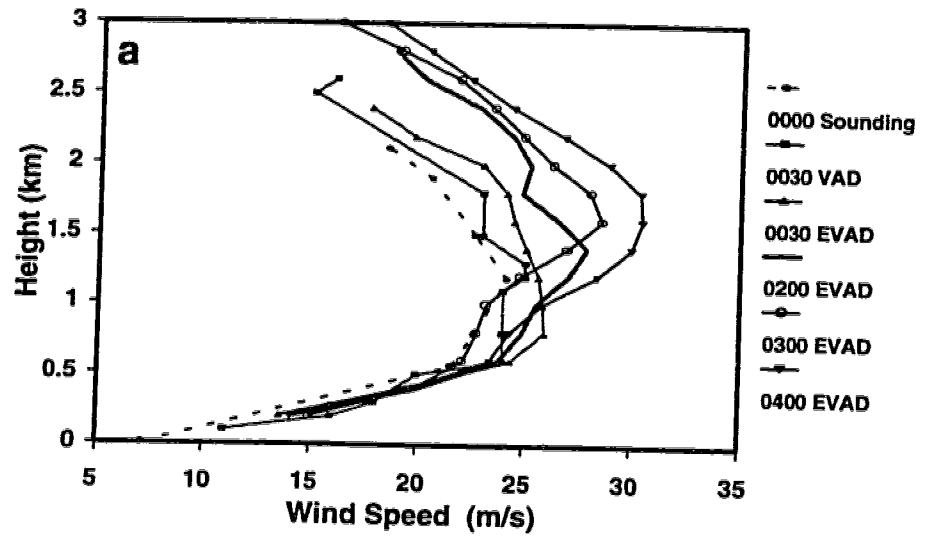


Figure 2.15 Vertical profiles of (a) wind speed, and (b) wind direction from the EVAD analyses at 0030, 0200, 0300 and 0400 UTC. The wind observations from the rawinsonde ascent at Stony Plain and the VAD values at the 0-90 km range and 1.5° elevation angle are also included for comparison.

References

- Browning, R. A., and R. Wexler, 1968: The determination of kinematic properties of a wind field using Doppler radar. *J. Appl. Meteor.*, **7**, 105-113.
- Caton, P. G. F., 1963: The measurement of wind and convergence by Doppler radar. *Proc. 10th Conf. on Radar Meteor.*, Washington, DC, Amer. Meteor. Soc., 290-296.
- Caya, D. and I. Zawadzki, 1992: VAD analysis of nonlinear wind fields. *J. Atmos. Oceanic Technol.*, **1**, 50-57.
- Crozier, C. L., 1986: *King Weather Radar Operations Manual and Users Guide*. Internal publication, Atmospheric Environment Service, Environment Canada.
- Doviak, R. J., and D. S. Zrnic, 1993: *Doppler Radar and Weather Observations*. Academic Press, 562 pp.
- Draper, W. R., and H. Smith, 1966: *Applied Regression Analysis*. Wiley Press, 407 pp.
- Easterbrook, C. C., 1975: Estimating horizontal wind fields by two-dimensional curve fitting of single Doppler radar measurements. *Preprints, 16th Conf. on Radar Meteor.*, Houston, Amer. Meteor. Soc., 214-219.
- Koscielny, A. J., R. J. Doviak and R. Rabin, 1982: Statistical considerations in the estimation of divergence from single Doppler radar and application to pre-storm boundary-layer observation. *J. Appl. Meteor.*, **21**, 197-210.
- Kropfli, R. A., 1986: Single Doppler radar measurements of turbulence profiles in the convective boundary layer. *J. Atmos. Sci.*, 305-314.
- Lhermitte, R. M. and D. Atlas, 1961: Precipitation motion by pulse-Doppler radar. *Proc. 9th Conf. on Radar Meteor.*, Kansas City, Amer. Meteor. Soc., 218-223.
- _____, and _____, 1963: Doppler fall speed and particle growth in stratiform precipitation. *Proc. 10th Conf. on Radar Meteor.*, Houston, Amer. Meteor. Soc., 297-302.
- Matejka, T. J. and R. C. Srivastava, 1991: An improved version of the extended velocity-azimuth display analysis of single-Doppler radar data. *J. Atmos. Oceanic Technol.*, **8**, 453-466.
- Passarelli, R. E., 1983: Wind field estimation by single Doppler radar techniques. *Proc. 21st Conf. on Radar Meteor.*, Boston, Amer. Meteor. Soc., 526-529.

- Rabin, R. M., and I. Zawadzki, 1984: On the single Doppler measurements of divergence in clear air. *J. Atmos. Oceanic Technol.*, **1**, 50-57.
- Rabin, R. M., and Zrnic, D. S., 1980: Subsynoptic-scale vertical wind revealed by dual Doppler radar and VAD analysis. *J. Atmos. Sci.*, **37**, 644-654.
- Ray, P. S., ed., 1986: *Mesoscale Meteorology and Forecasting*. Amer. Meteor. Soc., Boston, 793 pp.
- Srivastava, R. C., T. J. Matejka, and T. J. Lorello, 1986: Doppler radar study of the trailing anvil region associated with a squall line. *J. Atmos. Sci.*, **43**, 356-377.
- Takahashi, N., H. Uyeda and K. Kikuchi and M. Okazaki, 1991: A method to describe the fluctuation and discontinuity of horizontal wind fields by single Doppler radar. *Proc. 25th Conf. on Radar Meteor.*, Boston, Amer. Meteor. Soc., 642-645.
- Waldteufel, R., and H. Corbin, 1979: On the analysis of single Doppler data. *J. Appl. Meteor.*, **18**, 532-542.
- Xu, M. and T. Gal-Chen, 1993: A study of the convective boundary-layer dynamics using single Doppler radar measurements. *J. Atmos. Sci.*, **50**, 3641-3662.
- Zawadzki, I., and C. Desrochers, 1991: A method for real time de-aliasing of very moist clear air Doppler data. *Proc. 25th Conf. on Radar Meteor.*, Boston, Amer. Meteor. Soc., 879-881.

CHAPTER 3

ESTIMATION OF DIVERGENCE IN SCATTERED ECHO REGIONS USING THE VVP TECHNIQUE

Remark: The revised version of this chapter has been submitted as a research note to the *Journal of Atmospheric and Oceanic Technology* for publication.

3.1 Introduction

The Velocity Azimuth Display (VAD) and Extended VAD (EVAD) techniques used to analyse radial velocity measurements sampled by a single Doppler radar are not feasible when precipitation echoes do not fill the entire radar scanning area. In many cases, particularly during summer convection, precipitation echoes are often organized into cells or lines with echo-free regions interspersed. To estimate wind properties for less widespread convective precipitation, the Volume Velocity Processing (VVP) method can be used (Waldteufel and Corbin 1979, Koscielny et al. 1982, Smith and Rabin 1989). For the VVP analysis, radial velocity data are required only within a small volume delimited by an azimuth range of about 30° , a radial range of about 30 km, and an elevation angle range of about 1° .

Despite its attractive ability to deal with scattered precipitation, the VVP method has been used sparingly in the past. The first attempt at using this method was made by Waldteufel and Corbin (1979) who studied wind kinematic properties in frontal precipitation zones. They found that departures from linearity in the actual wind field constitute the basic limitation to wide application of the VVP method. Koscielny et al. (1982) applied the VVP method and showed that areas of convergence coincided with regions where cumulus clouds and storms later developed. Johnston (1984) used the technique to reveal the kinematic structures of cold frontal rainbands. Smith and Rabin (1989) assessed the accuracy of this technique in a case study of a severe storm outbreak in central Oklahoma.

In this chapter, the VVP approach is applied to the Doppler velocity data sampled by the Carvel radar to estimate the low-level convergence field. The case considered occurred on 19 August 1992. A multicellular thunderstorm passed through central Alberta and spawned two tornadoes. Hailstones were reported with sizes ranging from pea to golf-ball. Before this case is investigated, the VVP method is first applied to simulated radial velocity data to determine how the accuracy of the VVP algorithm depends on the number of model parameters and the analysis volume resolution.

3.2 The Method

The VVP technique can be best described with reference to Figure 3.1. Data are sampled in the range from r to $r+\Delta r$, azimuth from ϕ to $\phi+\Delta\phi$, and elevation angle from α to $\alpha+\Delta\alpha$. The volume element $\Delta r \times \Delta\phi \times \Delta\alpha$ is referred to as the **analysis volume**. It is convenient to use a Cartesian coordinate system xyz as shown in Figure 3.1. The z axis points upwards, while the x -axis and the y -axis are directed eastwards and northwards, respectively. The coordinate (x, y, z) is related to the spherical radar coordinates (r, ϕ, α) by:

$$\begin{aligned} x &= r \sin\phi \cos\alpha \\ y &= r \cos\phi \cos\alpha \\ z &= r \sin\alpha \end{aligned} \quad (3.1)$$

The basic assumption of the VVP method is that the spatial variation of the wind can be approximated by a linear function. Specifically, the wind vector $\vec{V}=(u, v, w)$ at a point (r, ϕ, α) is assumed to vary linearly in $x, y,$ and z :

$$\vec{V}(x, y, z) = \vec{V}_o(x_o, y_o, z_o) + \frac{\partial \vec{V}}{\partial x}(x-x_o) + \frac{\partial \vec{V}}{\partial y}(y-y_o) + \frac{\partial \vec{V}}{\partial z}(z-z_o) \quad , \quad (3.2)$$

where $\vec{V}_o=(u_o, v_o, w_o)$ is the wind at the point (x_o, y_o, z_o) , which is usually taken as the centre of the analysis volume.

The radial component of air velocity along the radar beam, V_r , is the projection of \vec{V} onto \vec{r} which is the position vector from the radar to the data point (r, ϕ, α) . That is,

$$\begin{aligned}
V_r &= \vec{V} \cdot \vec{r} \\
&= u \sin\phi \cos\alpha + v \cos\phi \cos\alpha + w \sin\alpha \\
&= u_o' \sin\phi \cos\alpha \\
&\quad + v_o' \cos\phi \cos\alpha \\
&\quad + (u_y + v_x) [r \cos\alpha \sin\phi \cos\phi - \frac{1}{2}(x_o \cos\phi + y_o \sin\phi)] \cos\alpha \\
&\quad + u_x [r \sin\phi \cos\alpha - x_o] \sin\phi \cos\alpha \\
&\quad + v_y [r \cos\phi \cos\alpha - y_o] \cos\phi \cos\alpha \\
&\quad + u_z [r \sin\alpha - z_o] \sin\phi \cos\alpha \\
&\quad + v_z [r \sin\alpha - z_o] \cos\phi \cos\alpha \\
&\quad + w_o \sin\alpha \\
&\quad + w_z [r \sin\alpha - z_o] \sin\alpha \\
&\quad + w_x [r \sin\phi \cos\alpha - x_o] \sin\alpha \\
&\quad + w_y [r \cos\phi \cos\alpha - y_o] \sin\alpha
\end{aligned} \tag{3.3}$$

where $u_o' = [u_o + \frac{1}{2}y_o (v_x - u_y)]$, $v_o' = [v_o - \frac{1}{2}x_o (v_x - u_y)]$. The subscripts x , y and z denote partial derivatives. Since the 11 unknowns (u_o' , v_o' , $u_y + v_x$, u_x , v_y , u_z , v_z , w_o , w_x , w_y and w_z) are multiplied by different functions of r , ϕ and α , the kinematic properties of the wind field can be discriminated through the different dependencies that they predict on the measured radial component V_r as \vec{r} scans the entire analysis volume. However, four of the linear wind parameters, u_o' , v_o' , u_y , v_x , appear in (3.3) in combined forms multiplied by unique trigonometric functions. Additional assumptions have to be made to determine all of the 12 parameters. For example, the vertical component of vorticity, $(v_x - u_y)$, cannot be discriminated from u_o and v_o because they share a common trigonometric dependency. If x_o and y_o were zero, then u_o and v_o would be uncoupled from vorticity and hence could be retrieved. However, this would require the analysis volume to be centred directly above the radar site, constituting a severe restriction.

To simplify notation, a column vector U_{11} is introduced with its definition:

$$\begin{aligned}
\mathbf{U}_{11}^T &= [u'_o, v'_o, u_y+v_x, u_x, v_y, u_z, v_z, w_o, w_x, w_y, w_z] \\
&= [u_1, u_2, u_3, \dots, u_{11}] \quad ,
\end{aligned} \tag{3.4}$$

where the superscript T denotes the matrix transpose. The trigonometric functions in (3.3) are referred to as predictor functions of r , ϕ , and α , denoted by

$$\mathbf{P}_{11} = \begin{bmatrix} p_1 \\ p_2 \\ p_3 \\ p_4 \\ p_5 \\ p_6 \\ p_7 \\ p_8 \\ p_9 \\ p_{10} \\ p_{11} \end{bmatrix} = \begin{bmatrix} u'_o \sin\phi \cos\alpha \\ v'_o \cos\phi \cos\alpha \\ (u_y+v_x) [r \cos\alpha \sin\phi \cos\phi - \frac{1}{2}(x_o \cos\phi + y_o \sin\phi)] \cos\alpha \\ u_x [r \sin\phi \cos\alpha - x_o] \sin\phi \cos\alpha \\ v_y [r \cos\phi \cos\alpha - y_o] \cos\phi \cos\alpha \\ u_z [r \sin\alpha - z_o] \sin\phi \cos\alpha \\ v_z [r \sin\alpha - z_o] \cos\phi \cos\alpha \\ w_o \sin\alpha \\ w_z [r \sin\alpha - z_o] \sin\alpha \\ w_x [r \sin\phi \cos\alpha - x_o] \sin\alpha \\ w_y [r \cos\phi \cos\alpha - y_o] \sin\alpha \end{bmatrix} \tag{3.5}$$

Using this notation, the radial component of air velocity can be expressed as

$$\mathbf{V}_r = \mathbf{P}_{11}^T \cdot \mathbf{U}_{11} \quad . \tag{3.6}$$

Within the analysis volume, the number of radial velocity measurements, n , is determined by n_r , n_ϕ and n_α which, respectively, represents the V_r numbers measured at various ranges, azimuths and elevation angles. Typically, the value of n ($=n_r \times n_\phi \times n_\alpha$) reaches about 10^3 to 10^4 . All V_r measurements within the analysis volume are grouped into a vector $\mathbf{V}_m^T = (V_{r1}, V_{r2}, \dots, V_m)$. The associated predictor functions, \mathbf{P} , are arranged into an $(n \times m)$ matrix $\mathbf{Q}_{nm}^T = (\mathbf{P}_{1m}^T, \mathbf{P}_{2m}^T, \dots, \mathbf{P}_{im}^T, \dots, \mathbf{P}_{nm}^T)$, where \mathbf{P}_{im} is determined by (3.5) for m ($=11$ here) predictors with index $i=1, 2, \dots, n$. Therefore, we have $\mathbf{V}_m = \mathbf{Q}_{nm} \cdot \mathbf{U}_m$. Estimation of parameters becomes a multivariate regression problem which can be solved by standard

techniques such as the least-squares fit. The least-squares estimate of U_m , denoted by \hat{U}_m , is computed from (Draper and Smith 1966, p.59)

$$\hat{U}_m = G_{mm}^{-1} \cdot Q_{nm}^T \cdot V_m \quad (3.7)$$

where $G_{mm} = Q_{nm}^T \cdot Q_{nm}$ contains the covariances between the predictor functions, and the superscript "-1" indicates the matrix inverse.

The number m in (3.7) can be chosen as a value equal to or less than 11 . Usually, the variances of parameter estimates tend to increase with the number of regressors because the same amount of information on the radial velocity field in a fixed volume is spread over more regressors. This results in a loss of confidence in each corresponding parameter estimate. When the parameters of the model (3.7) are less than 11 , Koscielny et al. (1982) called such processing the **Modified Volume Velocity Processing (MVVP)**.

3.3 The VVP Error Analysis and Geometry of Analysis Volume

3.3.1 Seven-parameter VVP technique

To examine how the selection of m affects the estimates of kinematic parameters, the VVP analysis is first applied to simulated radial velocity data. The twelve parameters defining a linear simulated wind field are $u_o, u_x, u_y, u_z, v_o, v_x, v_y, v_z, w_o, w_x, w_y,$ and w_z . Typical values for these parameters, as suggested by Waldteufel and Corbin (1979) based on earlier observations, are listed in Table 3.1.

Table 3.1 Typical values of mesoscale wind parameters (adopted from Waldteufel and Corbin 1979).

Zeroth Derivative Terms	(ms ⁻¹)	First Derivative Terms	(10 ⁻⁴ s ⁻¹)
u_o, v_o	10.0	u_x, u_y, v_x, v_y	1.0
		u_z, v_z	10.0
w_o	5.0	w_x, w_y	0.1
		w_z	5.0

Simulated radial velocity data are computed using (3.3). The analysis volume is chosen to be a sector of $40^\circ \times 40$ km with elevation angles of 0.4° and 0.8° . The VVP estimates of kinematic parameters for the simulated wind, \hat{U}_m , are obtained using (3.7). Table 3.2 lists the comparison of the estimates with their initial control values, U_{m0} , for $m=7$, $m=9$, and $m=11$, respectively. When $m=11$, the differences between U_{m0} and \hat{U}_m for u_o , v_o , and u_x are not small (relative errors around 30%), but still tolerable. However, the estimates for u_z , v_z , w_o , w_z , w_x and w_y are extremely in error. As m is reduced in the postulated model, more of the estimates approach their initial control values. When $m=7$, all estimates are fairly accurate.

Table 3.2 Comparison of the estimates of kinematic parameters from the VVP analysis with their simulated control values when the processing includes 11, 9, and 7 parameters. The analysis volume consists of a sector of $40^\circ \times 40$ km with elevation angles of 0.4° and 0.8° . The simulated control values are taken from Table 3.1.

Parameters	Units	Control Values		Estimates	
		U_{m0}	\hat{U}_7 (MVVP)	\hat{U}_9 (MVVP)	\hat{U}_{11} (VVP)
u_o	ms^{-1}	10.0	10.01	11.14	12.56
v_o	ms^{-1}	10.0	10.05	12.95	12.94
u_y+v_x	$10^{-4} s^{-1}$	2.0	1.99	0.66	11.75
u_x	$10^{-4} s^{-1}$	1.0	1.00	0.96	1.88
v_y	$10^{-4} s^{-1}$	1.0	0.97	0.52	14.98
u_z	$10^{-4} s^{-1}$	10.0	10.08	142.7	695.07
v_z	$10^{-4} s^{-1}$	10.0	13.02	358.58	-121.29
w_o	ms^{-1}	5.0	/	265.31	-4459.0
w_z	$10^{-4} s^{-1}$	5.0	/	-17295.0	-15219.0
w_x	$10^{-4} s^{-1}$	0.1	/	/	-8034.7
w_y	$10^{-4} s^{-1}$	0.1	/	/	-1786.8

Therefore, the proper selection of m for the postulated model is crucial in order to obtain valid U_m estimates. To estimate divergence, terms w_o , w_x , w_y and w_z are

mathematically considered to be nuisance parameters in the least-squares regression (Draper and Smith 1966, p.81), and will be left out of the model. The vertical derivatives of horizontal wind, u_z and v_z , will be kept in the model (3.6) to remove the contamination of horizontal derivatives caused by the vertical shear (Koscielny et. al 1982). This regression model with seven parameters will henceforth be called the VVP7 algorithm.

3.3.2 Error analysis

The error analysis performed here is based on the statistical regression theory presented in detail by Draper and Smith (1966). For a postulated model in which some necessary parameters have been left out, the unbiased estimate of U_m can be obtained from (Draper and Smith, p.81):

$$E[\hat{U}_m] = U_m + A_{ml} U_l^T \quad (3.8)$$

where $E[\hat{U}_m]$ is the expected value of \hat{U}_m , and $l = 11 - m$. Vector $U_l^T = [u_{m+1}, u_{m+2}, \dots, u_{11}]$ denotes the unmodeled parameters. The alias matrix A_{ml} is computed using

$$A_{ml} = G_{mm}^{-1} \cdot Q_{nm}^T \cdot Q_{nl} \quad (3.9)$$

where $Q_{nl} = [P_{1l}^T, P_{2l}^T, \dots, P_{nl}^T]$ and $P_l^T = [p_{m+1}, p_{m+2}, \dots, p_{11}]$. Since the alias matrix depends on the predictors P_m and the geometry of the analysis volume, the bias in \hat{U}_m can be reduced if the analysis volume is properly designed.

Because the parameter-estimate variance resulting from unmodeled wind parameters and velocity measurement errors is unknown, it is often estimated using the variance errors of \hat{U}_m (e.g., Koscielny et al. 1982). For each parameter, the magnitude of this variance is determined by the diagonal elements of the covariance matrix of U_m . The covariance matrix C_{mm} is given by (Draper and Smith, p.61):

$$C_{mm} = G_{mm}^{-1} \cdot \sigma_\epsilon^2 \quad (3.10)$$

where σ_e^2 is the sum of squares of the residuals from the least-squares fit, which is determined by (Draper and Smith, p.88)

$$\sigma_e^2 = \frac{\mathbf{E}_n^T \cdot \mathbf{E}_n}{(n-m)} \quad (3.11)$$

and $\mathbf{E}_n = [\mathbf{V}_m - \mathbf{Q}_{nm}^T \cdot \hat{\mathbf{U}}_m]$. When the $\hat{\mathbf{U}}_m$ estimates are unbiased, σ_e^2 represents the variance of measurement errors in Doppler velocity. Measurement errors are assumed to be uncorrelated normal random variables with zero mean and variance σ_e^2 . The result of (3.10) and (3.11) indicates that the inaccuracy of each parameter estimate increases linearly with the statistical uncertainty in the V_r measurement made by the Doppler radar.

The normalized standard error of the divergence estimate is computed by:

$$\begin{aligned} \sigma_d &= [\sigma_{u_x}^2 + \sigma_{v_y}^2 + 2 \text{COV}(u_x, v_y)]^{1/2} / \sigma_e \\ &= (c_{44} + c_{55} + 2c_{45})^{1/2} \end{aligned} \quad (3.12)$$

where σ_{u_x} and σ_{v_y} are the standard errors of u_x and v_y , $\text{COV}(u_x, v_y)$ is the covariance of errors in u_x and v_y , and c_{ij} is an element of matrix \mathbf{C}_{mm} . From the VVP analyses for the simulated wind field, the standard errors in divergence estimate are $1.4 \times 10^{-4} \text{ s}^{-1}$, $1.5 \times 10^{-6} \text{ s}^{-1}$ and $1.5 \times 10^{-7} \text{ s}^{-1}$ when $m=11, 9$, and 7 , respectively. That is, the VVP7 technique yields a σ_d , three orders smaller than that from the VVP11 method and one order smaller than that from the VVP9. Therefore, the VVP7 algorithm will be adopted in the following analyses to estimate divergence, deformation and vertical shear.

3.3.3 Effects of geometry of analysis volume on estimates

Since the VVP estimates $\hat{\mathbf{U}}_m$ are related to the predictor matrix \mathbf{Q}_{nm} in (3.7), the size and shape of an analysis volume and the distribution of data therein will affect the accuracy of the kinematic estimates. In this subsection, we examine how $\hat{\mathbf{U}}_m$ and σ_d depend upon the geometry of the analysis volume in a simulated wind field. The simulated wind field is specified in Table 3.1. Using spacings of 500 m in range and 1° in azimuth, radial velocity data are computed at elevation angles of 0.4° and 0.8° . The least-squares

estimates of U_m are obtained by using (3.7). Under various sector sizes of $\Delta\phi \times \Delta r$, relative errors in estimates, labelled as $\hat{U}_m\%$, and the divergence standard error, σ_d , are listed in Table 3.3. For all sectors, the estimates of horizontal mean wind, u_o , and v_o , agree with their simulated control values within an error margin of $\hat{U}_m\%$ less than 10%. However, the σ_d value and the estimates of horizontal deformation and vertical shear are fairly sensitive to the variation of $\Delta\phi \times \Delta r$. In general, with the increase of $\Delta\phi$ or Δr , $\hat{U}_m\%$ decreases as a consequence of the correlations among the regressors being reduced. All seven parameters can be accurately estimated ($\hat{U}_m\% \leq 25\%$) when the sector sizes of $30^\circ \times 30$ km, $40^\circ \times 20$ km, $40^\circ \times 30$ km and $40^\circ \times 40$ km are used. Although larger analysis volumes could contain more radial velocity measurements (i.e., greater n), the estimates obtained from such volumes would likely become questionable due to violation of the linear wind assumption (Waldteufel and Corbin 1979). The best compromise seems to use an analysis volume which has an azimuthal width of about 40° , and a range extent of about 20 km. At least two elevations are needed for estimating vertical shear.

Table 3.3 *Relative errors in kinematic parameter estimates and the standard errors in divergence estimation for a simulated wind field under various sized sectors of $\Delta\phi \times \Delta r$ using the VVP7 with $\alpha_1=0.4^\circ$ and $\alpha_2=0.8^\circ$.*

$\Delta\phi \times \Delta r$	Relative Errors in \hat{U}_m Estimates [$\hat{U}_m\% = (\hat{U}_m - U_{mo})/U_{mo} \times 100\%$]							σ_d ($10^{-1} s^{-1}$)
	u_o	v_o	u_y+v_x	u_x	v_y	u_z	v_z	
$10^\circ \times 30$ km	2.8	0.4	21.0	127.0	4.0	30.2	2.6	12.8
$20^\circ \times 30$ km	2.2	0.4	1.0	28.0	1.0	86.0	7.4	2.5
$30^\circ \times 30$ km	1.2	1.1	0.5	4.0	1.0	20.6	20.3	0.9
$40^\circ \times 30$ km	0.2	1.0	5.5	17.0	2.0	4.9	16.6	0.5
$40^\circ \times 10$ km	0.6	1.3	17.0	32.0	8.0	3.5	36.4	1.4
$40^\circ \times 20$ km	0.2	1.2	12.5	25.0	5.0	0.6	19.9	0.7
$40^\circ \times 30$ km	0.2	1.0	5.5	17.0	2.0	4.9	16.6	0.5
$40^\circ \times 40$ km	0.1	1.1	5.5	15.0	2.0	6.1	14.4	0.3

3.4 Application of the VVP Technique to the Carvel Radar

The seven-parameter VVP algorithm is applied to the Doppler velocity data collected by the Carvel radar on 19 August 1992. This day presents an interesting case study for testing the VVP analysis.

3.4.1 Synoptic situations

Figure 3.2 shows the 850-mb weather chart at 0000 UTC on 19 August 1992. A short-wave trough was over western Canada with the trough axis passing through central Alberta. This trough axis remained essentially stationary during the next 12 hours. There was significant baroclinicity over the region with 850-mb isotherms ranging from 8°C to 26°C. The alignments of geopotential height contours and isotherms suggest that there was cold air advection at mid-levels on the lee-side of the Rocky Mountains overrunning the warm and moist air near the surface. The cooling aloft likely contributed to the build-up of potential instability for convective overturning.

The 1200 UTC sounding taken at Stony Plain (Figure 3.3) indicates the potential for convective instability. The temperature lapse rate was close to dry adiabatic from the surface to about 850-mb. However, the vapor mixing ratio was not well-mixed in the boundary layer. The air was moist in the layer between 850 and 500 mb, but relatively dry aloft. The airmass was convectively unstable with a Convective Available Potential Energy of about 607 J kg^{-1} for the surface air.

Surface observations from Alberta Forestry Lightning Detection network, weather watcher and synoptic stations indicated that storms were quite vigorous on 19 August 1992. About 15,000 lightning strikes appeared in a wide band from Grande Cache to Cold Lake. Hail (as large as golf-ball size) fell near Barrhead around 0130 UTC, at Morinville at 0525 UTC, and later from Josephburg to Hillard. Pea-sized hailstones were reported at Redwater, Fox Creek, Edmonton, Whitecourt, Grande Prairie, Edson and Slave Lake. A tornado near Fort Assinibolne at 0130 UTC damaged a mobile home and levelled trees at a campground. At 0315 UTC, another tornado picked up dust near Morinville. More information about the storm observations can be found in Vickers (1992).

3.4.2 Radar observations

Radar data were sampled by the Carvel operational C-band Doppler radar. Doppler velocity measurements were made every 10 minutes at elevation angles of 0.5, 1.5 and 3.5 degrees within a detecting radius of 110 km. Observations showed that an eastward-moving multicellular storm entered the radar coverage area from the northwest at 0000 UTC. Precipitating cells within this storm evolved rapidly. A gust-front appeared near the radar site at 0300 UTC and had echo cells stronger than 55 dBZ at its leading edge.

Figure 3.4 shows the 1.5° PPI (Plan Position Indicator) of radar reflectivity at 0630 UTC. The Carvel radar is located at point (0,0). At this time, cloud clusters were distributed in an azimuthal sector from 260° to 60°. There were three echo cells, labelled as A, B, and C. Cell A was centred at ($x=-65$ km, $y=50$ km), Cell B at ($x=-15$ km, $y=45$ km), and Cell C at ($x=25$ km, $y=50$ km). By 0700 UTC (Figure 3.5), Cell A had intensified with its maximum reflectivity changing from 30 dBZ to more than 35 dBZ. The intensity of Cell C, however, had been reduced from 35 dBZ to 30 dBZ. A new cell (Cell D) developed between Cell B and Cell C at ($x=0$ km, $y=45$ km) with its maximum reflectivity exceeding 35 dBZ. This observed decay, growth, and new development of convective cells are typical of the evolution features occurring in most multicell storms.

3.4.3 The VVP results

a. Divergence Estimate

Emphasis of our VVP7 analysis is placed on estimating low-level divergence, deformation and vertical wind shear based on the velocity data sampled at 0630 UTC. Before the VVP7 analysis was performed, observed radial velocity data were first pre-processed. Procedures for data decoding, velocity dealiasing, and outlier removing are described in detail in Appendix B. After this pre-processing, the corrected velocity data at ranges from 20 km to 100 km and azimuths from 260° to 60° are divided into a number of small sectors of size 40°×20 km. The two low elevation angles of 0.5° and 1.5° are used. Divergence (i.e., u_x+v_y) values are estimated and plotted at the centre of each sector. To

obtain a better resolution, the analysis is repeated with the analysis sector shifted 10° in azimuth.

The VVP7-deduced divergence estimates at 0630 UTC are contoured and shown in Figure 3.6. The results beyond a range of 100 km were neglected because of low Signal-to-Noise Ratio (SNR). Similarly, the estimate values at ranges less than 20 km are doubtful because of ground clutter contamination. Figure 3.6 shows that (positive) divergence appeared mainly in two large regions centred at $(x=-12 \text{ km}, y=45 \text{ km})$ and at $(x=25 \text{ km}, y=45 \text{ km})$, respectively. This divergent flow was likely associated with the precipitation outflow from echo cells (Cell B and Cell C shown in Figure 3.4). Meanwhile, there were two convergence (i.e., negative divergence) zones in the northwestern (Zone 1) and northern (Zone 2) sectors, respectively. The magnitude of the convergence in Zone 2 exceeded $1.5 \times 10^{-3} \text{ s}^{-1}$. In Zone 1, three small cells also had convergence values around $0.6 \times 10^{-4} \text{ s}^{-1}$. Previous studies have suggested that the convergence areas could influence the later development of convective precipitating cells (Byers and Braham 1949, Ogura and Chen 1977, and Ulanski and Garstang 1978). Their conclusion is supported by our analysis results.

Comparisons of Figure 3.4, Figure 3.5 and Figure 3.6 show that the enhancement of Cell A (from 30 dBZ at 0630 UTC to about 40 dBZ at 0700 UTC) was associated with the convergence area - Zone 1 at 0630 UTC. The strong convergence in Zone 2 at 0630 UTC led to a new large precipitating cell (Cell D) at 0700 UTC. Conversely, echo cells in the divergent flow areas, i.e., Cell B and Cell C, reduced their intensities during this 30 minutes period. This analysis confirms that the initiation or development of observed storms occurred within regions of moderately strong convergence of about 10^{-4} s^{-1} (e.g., Schreiber 1986, and Wilson et al. 1992).

The normalized standard error of divergence estimate, σ_d , obtained from the VVP7 analysis at 0630 UTC, is plotted in Figure 3.7. The accuracy of the divergence estimate is of the order of 10^{-5} s^{-1} in most areas. Achieving this precision in divergence estimate is useful in monitoring thunderstorm development because the typical convergence magnitude in such environments is on the order of 10^{-4} to 10^{-3} s^{-1} (e.g., Ogura and Chen

1979). For the three regions where $\sigma_d > 6.0 \times 10^{-5} \text{ s}^{-1}$, the divergence estimates become unreliable due to insufficient V_r measurements when either the detecting ranges were larger than 90 km or smaller than 20 km, or when the azimuths were beyond 60° .

b. Horizontal deformation and vertical shear

Horizontal deformation and vertical shear of the wind field at 0630 UTC were also retrieved using the VVP7 analysis. Figure 3.8 shows the deformation field ($u_d = v_x + u_y$). Three closed centres with strong deformation values appeared in the northwest, north and northeast areas, where Cells A, B and C were located (Figure 3.4). Horizontal deformation tends to reshape the spatial pattern of the precipitation field (e.g., Holton 1979). For example, a circular-shaped echo region can be deformed into an elliptic-shape. In our case, regions with positive deformation values would dilate northeastward, while areas with negative deformation values would expand along the northwest direction. This behaviour can be seen when the reflectivity fields at 0630 (Figure 3.4) and 0700 UTC (Figure 3.5) are compared. These strong deformation areas also had strong divergence or convergence values shown in Figure 3.6.

The field of the VVP7-derived vertical shear $[(u_z^2 + v_z^2)^{1/2}]$ at 0630 UTC is displayed in Figure 3.9. In the two areas of divergence (shown in Figure 3.6), vertical shear was strong with magnitudes reaching up to $8 \times 10^{-3} \text{ s}^{-1}$. The two convergence areas were also affected by vertical shear: $3 \times 10^{-3} \text{ s}^{-1}$ in Zone 2 and $8 \times 10^{-3} \text{ s}^{-1}$ in Zone 1. Early observations (e.g., Byers and Braham 1949) have suggested that vertical shear may suppress the growth of small convective cells because strong shear tends to tear the cells apart. However, large convective cells tend to be enhanced by the presence of shear since the updraft interacts with the sheared flow (e.g., Rotunno and Klemp 1985). For our case, echo cells were reduced in the divergence areas with strong shear, but were enhanced in the convergence regions with moderate-to-strong shear.

3.5 Summary and Conclusions

In this chapter, the single-Doppler analysis technique known as the VVP has been examined. By assuming linear wind variations within analysis volumes, some kinematic parameters of the wind field are estimated. It was shown that the accuracy of the estimates depends on several factors. First, estimation accuracy is largely influenced by the number of kinematic parameters included in the postulated model. The comparison of the results obtained from the VVP analyses with 11, 9 and 7 parameters in a simulated wind field showed that, to estimate divergence accurately, only the seven-parameter VVP algorithm is acceptable. The seven parameters include the divergence, deformation, vertical shear, and horizontal mean wind (modified by vertical vorticity). Secondly, the geometry of VVP7 analysis volumes affects the magnitudes of bias and variance errors in all parameter estimates. Results computed with simulated velocity data indicated that an appropriate analysis volume for estimating divergence should have an azimuthal width of about 30°-40° and a range extent of 20-30 km. Two low elevation angles are required for estimating vertical shear values. In addition, the VVP7 estimates also depend on the accuracy of Doppler velocity measurements. The uncertainty in all kinematic estimates increases linearly with random (i.e., spatially uncorrelated) errors in Doppler velocity measurements.

In the application of the VVP7 algorithm to the Doppler velocity data collected on 19 August 1992, the analysis volume was chosen to be 20 km × 40°. The standard error of the divergence estimate was approximately 10^{-5} s^{-1} , about one tenth of the typical convergence magnitude observed during storm formation. Analyses of observations showed that the initiation and enhancement of existing precipitating cells were both associated with the low-level convergence which was estimated from the VVP analysis. Conversely, echoes became suppressed in the areas of the VVP-deduced divergence. Combined with the information of vertical shear from the VVP7 analysis, we found that echo cells weakened in the divergent areas where strong wind shear appeared, but intensified when moderate-to-strong wind shear was co-located with strong convergence. The results from this chapter suggests that the VVP analysis technique has the potential for aiding in forecasting convective rainfall.

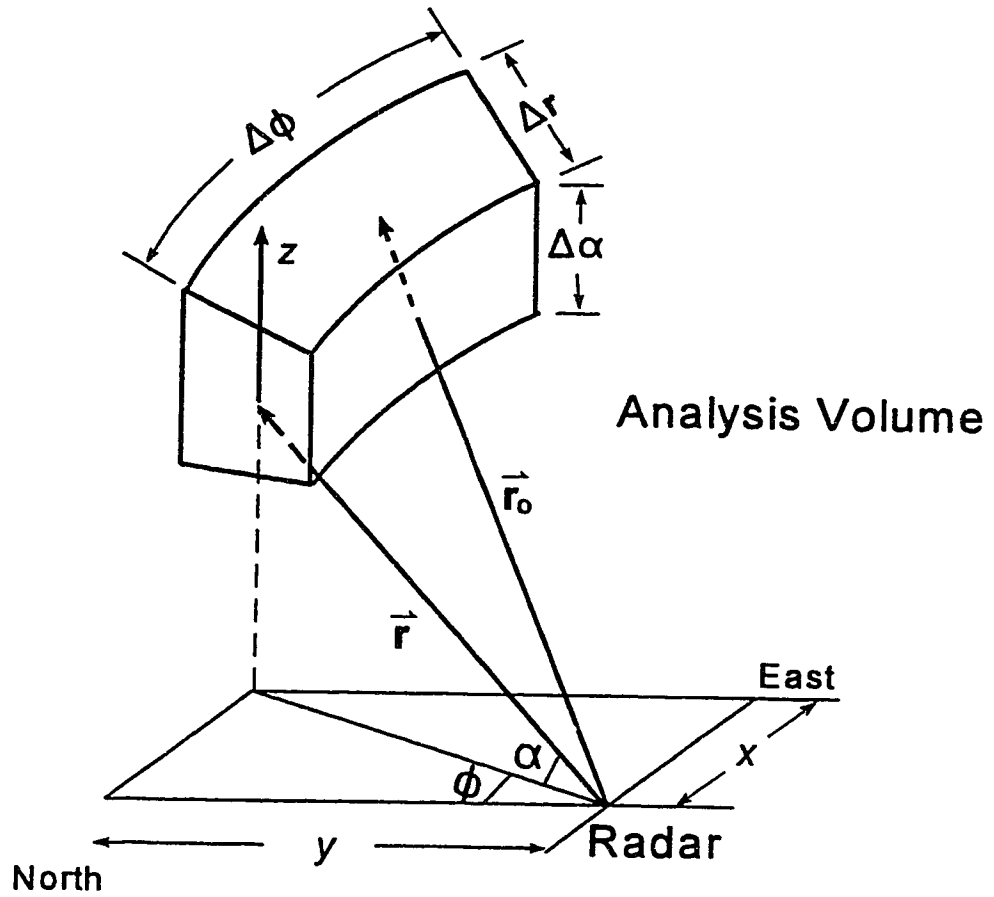


Figure 3.1 The geometry of analysis volume for the Velocity Volume Processing technique. The r , ϕ , α are the radar detecting range, azimuth and elevation angles, respectively. The range vector, \vec{r}_0 , is directed to the centre of the analysis volume from the radar.

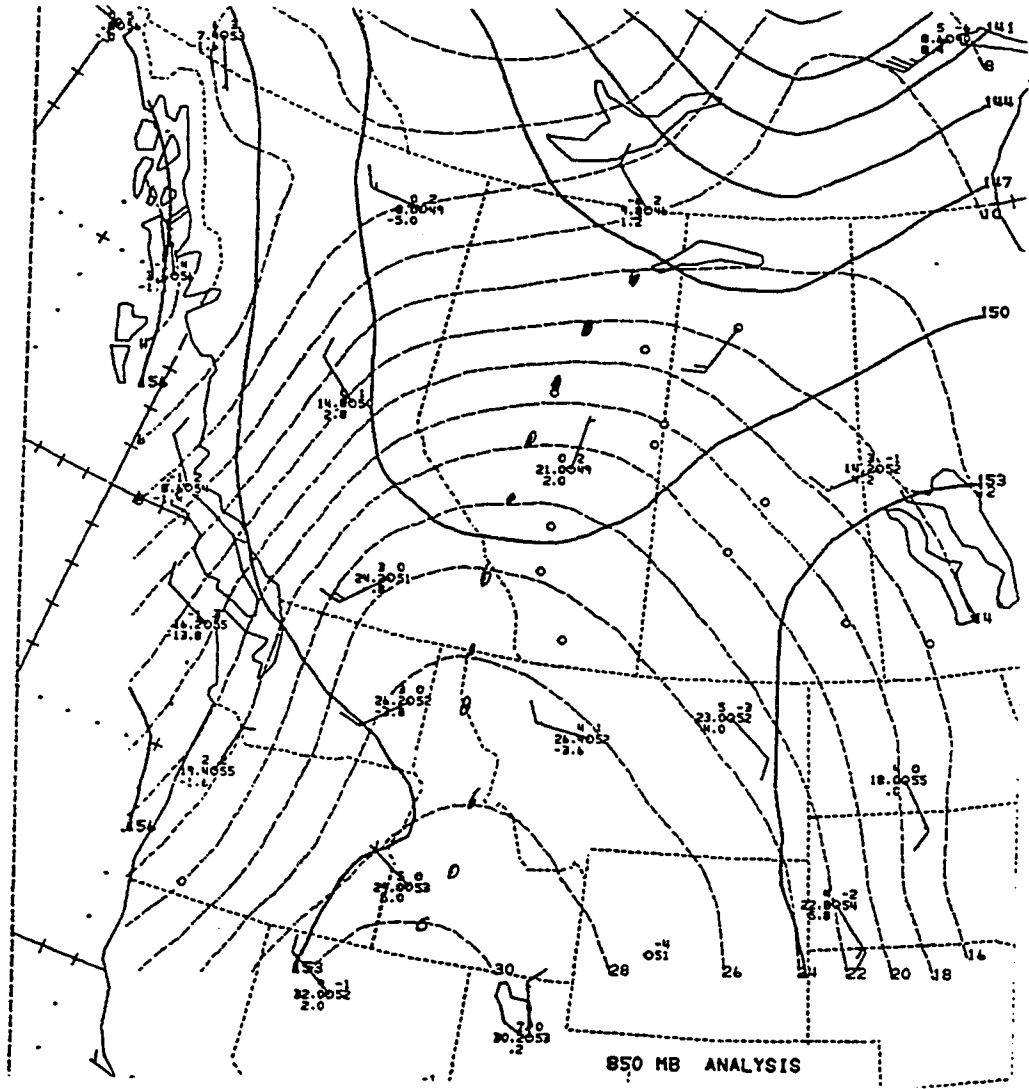


Figure 3.2 The 850-mb analysis at 0000 UTC on 19 August 1992. Solid lines are geopotential height contours in decameters while dashed lines are isotherms in °C. Wind barbs are in knots. A short wind barb is 5 knots, and a long wind barb is 10 knots.

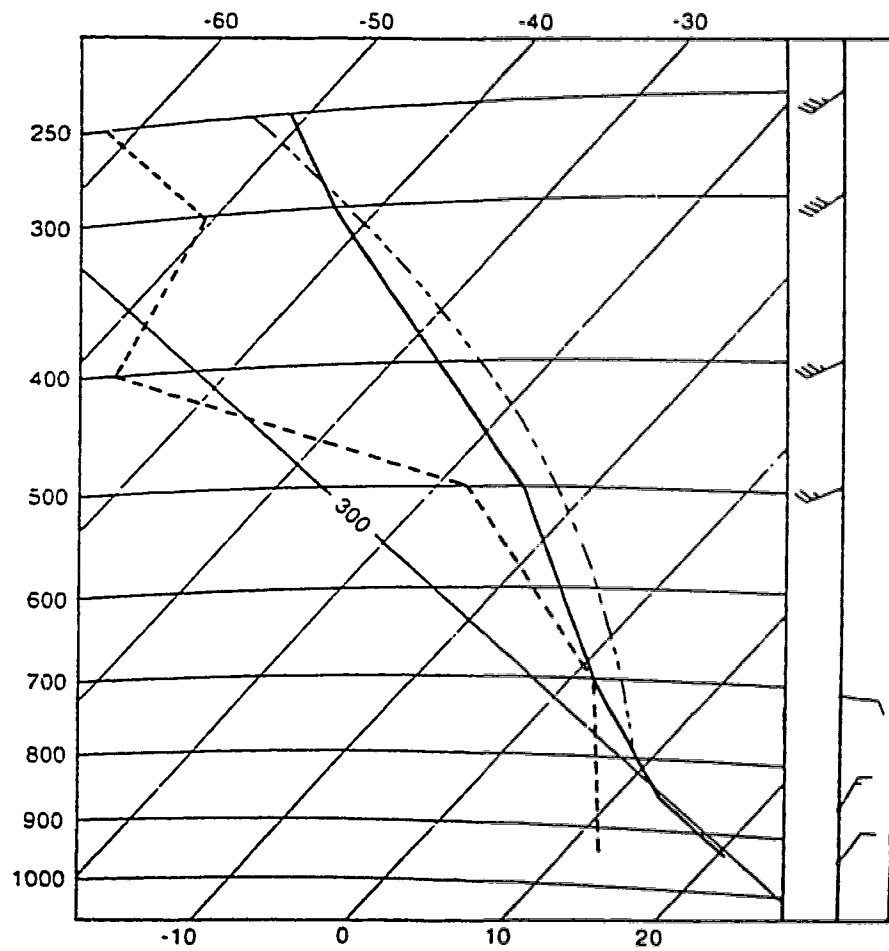


Figure 3.3 Sounding recorded at Stony Plain, Alberta at 1200 UTC on 19 August 1992. The thick solid line depicts the temperature in °C, and the thick dashed line the dew-point. Full wind barb is 5 ms⁻¹, and the wind flag 10 ms⁻¹.

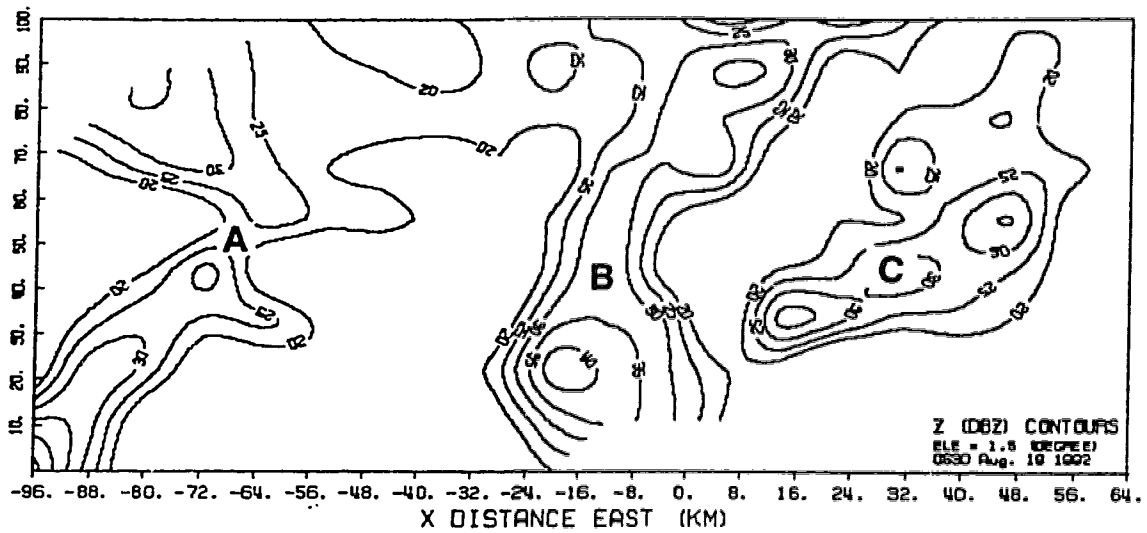


Figure 3.4. Radar reflectivity PPI in dBZ at elevation angle of 1.5° observed at 0630 UTC on 19 August 1992. The radar is sited at (0,0), and echo intensities are contoured in the interval of 5 dBZ.

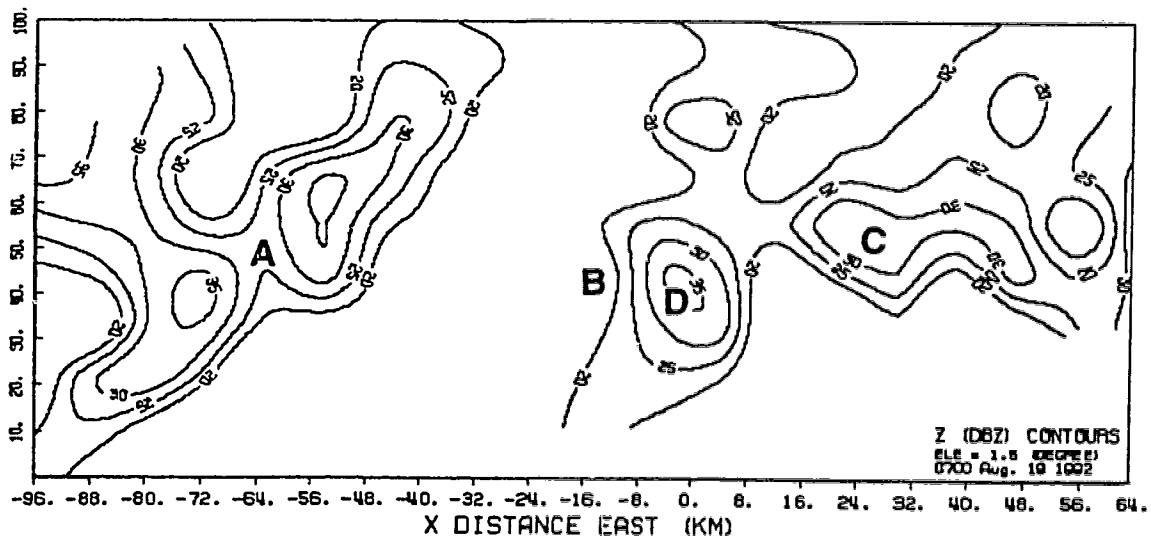


Figure 3.5. Same as Figure 3.4 except at 0700 UTC.

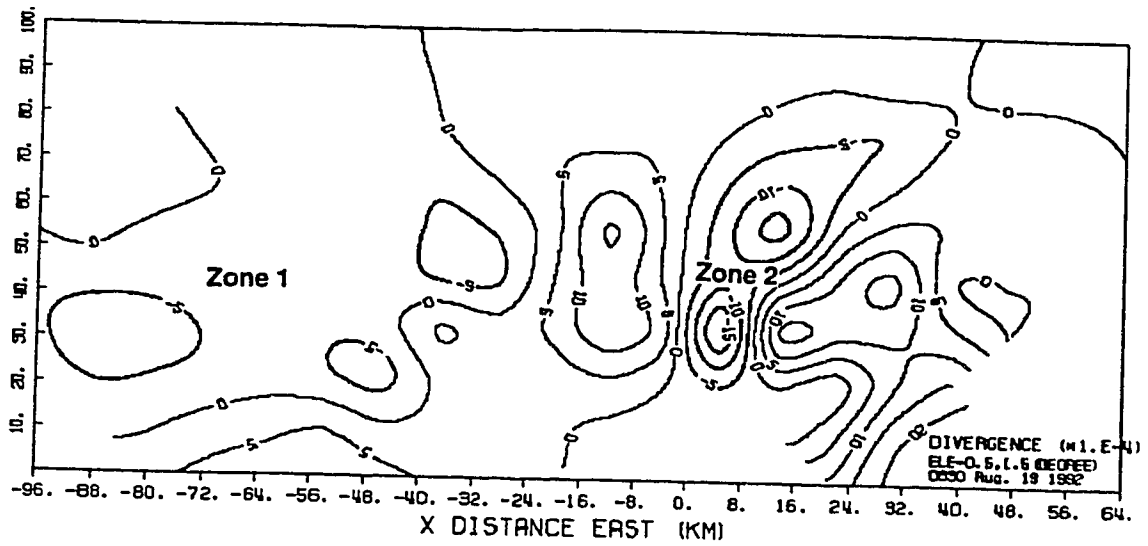


Figure 3.6. Horizontal divergence field computed from the Doppler velocity data at 0630 UTC on 19 August 1992 using the seven-parameter MVVP technique. The thick (thin) contours represent regions of convergence (divergence). The contour interval is $5 \times 10^{-4} \text{ s}^{-1}$.

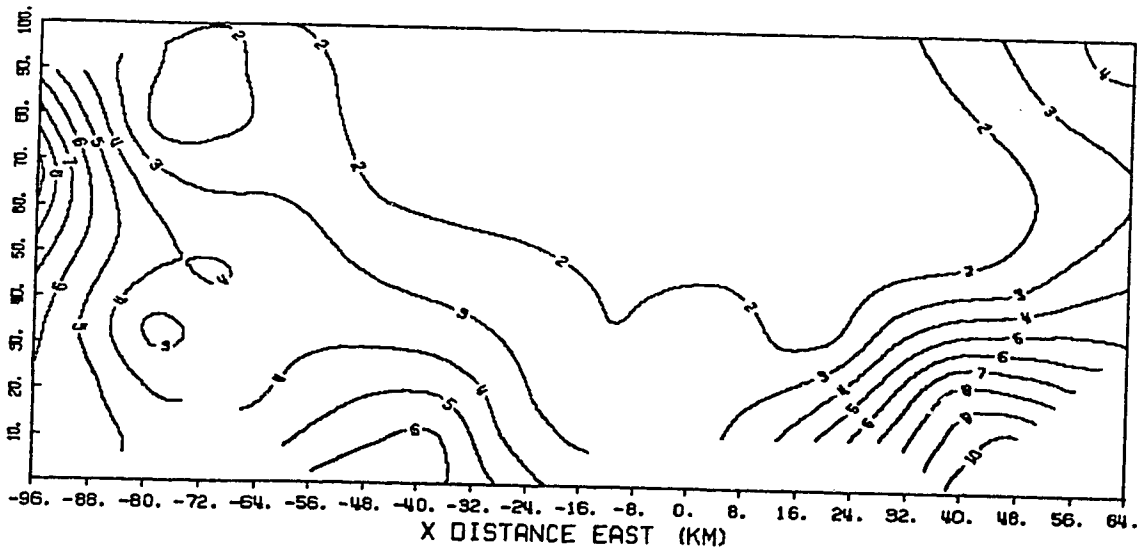


Figure 3.7. Same as Figure 3.6 except for the normalized standard error of divergence estimate σ_d . The contour interval is 10^{-5} s^{-1} .

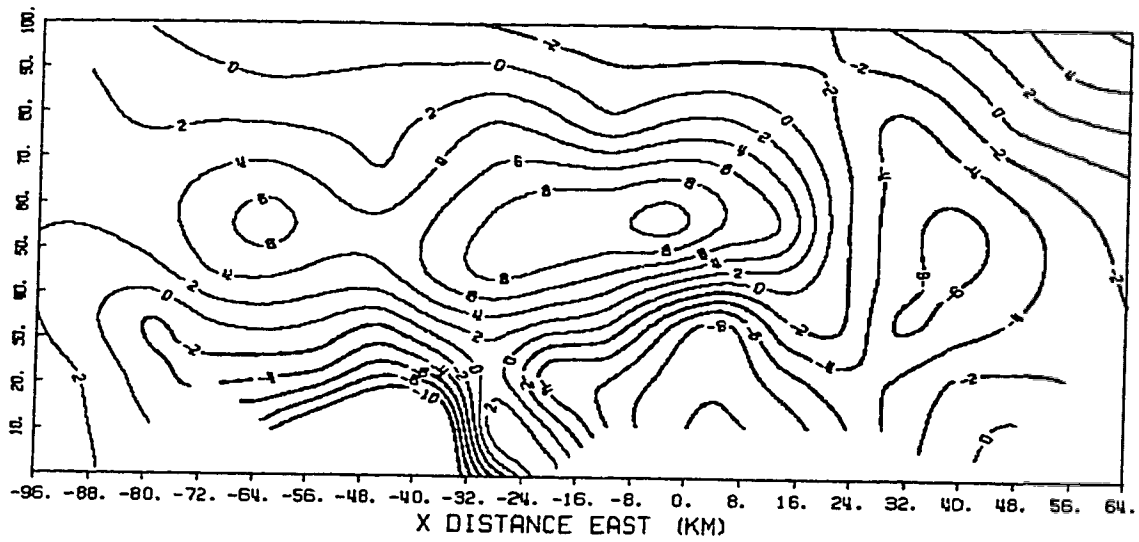


Figure 3.8. Same as Figure 3.6 except for the horizontal deformation, $(u_y + v_x)$. The contour is plotted in a step of $2 \times 10^{-4} \text{ s}^{-1}$.

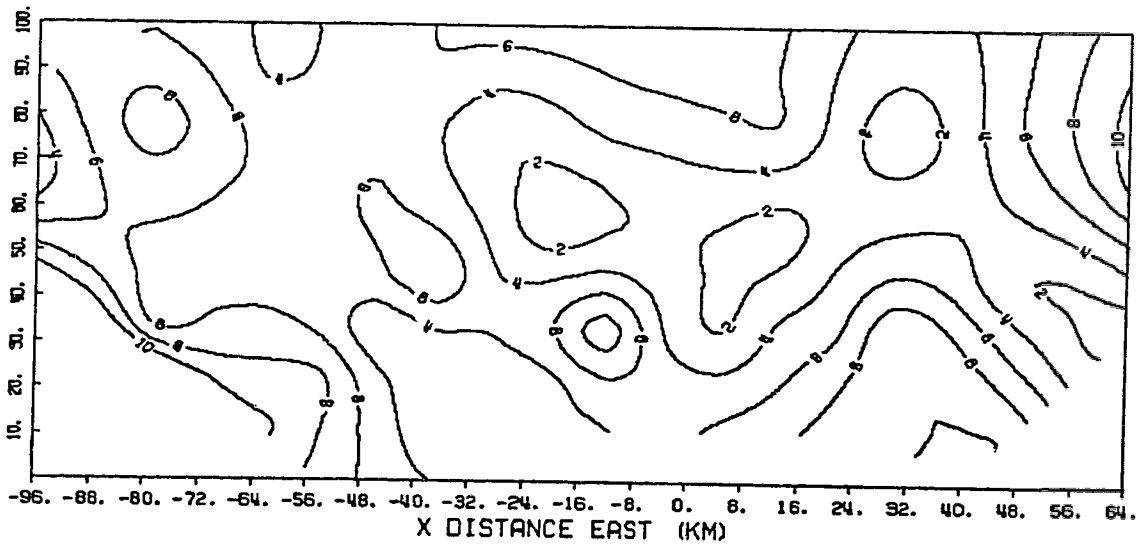


Figure 3.9. Same as Figure 3.6 except for the vertical wind shear, $(u_z^2 + v_z^2)^{1/2}$. The contour interval is $2 \times 10^{-3} \text{ s}^{-1}$.

References

- Byers, H. R., and R. R. Braham, Jr., 1949: *The Thunderstorm*. U.S. Govt. Printing Office, Washington, D. C., 287 pp.
- Doswell, C. A., 1987: The distinction between large-scale and mesoscale contribution to severe convection: A case study example. *Weather and Forecasting*, **1**, 3-16.
- Doviak, R. J., and D. S. Zrnic, 1993: *Doppler Radar and Weather Observations*. Academic Press, San Diego, California, 562 pp.
- Draper, J. R., and H. Smith, 1966: *Applied Regression Analysis*. Wiley Press, 407 pp.
- Holton, J. R., 1979: *An Introduction to Dynamic Meteorology*. 2nd Ed., Academic Press, London, 391 pp.
- Johnston, B. W., 1984: The kinematic structure of cold frontal rainbands. Rep. AS146, Dept. of Atmos. Sci., University of Wyoming.
- Koscielny, A. J., R. J. Doviak, and R. M. Rabin, 1982: Statistical considerations in the estimation of divergence from single Doppler radar and application to pre-storm boundary-layer observation. *J. Appl. Meteor.*, **21**, 197-210.
- Leichter, I., 1974: *Moisture flux and precipitation studies of convective storms in western South Dakota using pibal and radar data*. Rep. 74-11, Inst. of Atmos. Sci., South Dakota School of Mines and Technology, 63 pp.
- Lewis, J. M., Y. Ogura, and L. Gidel, 1974: Large-scale influences upon the generation of a mesoscale disturbance. *Mon. Wea. Rev.*, **102**, 545-560.
- Ogura, Y., and Y. L. Chen, 1977: A life history of an intense mesoscale convective storm in Oklahoma. *J. Atmos. Sci.*, **34**, 1458-1476.
- Rabin, R. M., and I. Zawadzki, 1984: On the single-Doppler measurement of divergence in clear air. *J. Atmos. Oceanic Technol.*, **1**, 50-57.
- Rotunno, R., and J. B. Klemp, 1985: On the rotation and propagation of simulated supercell thunderstorms. *J. Atmos. Sci.*, **42**, 271-292.
- Smith, S. D., and R. M. Rabin, 1989: Estimation of divergence in the prestorm boundary layer. *J. Atmos. Oceanic Technol.*, **6**, 459-475.
- Schreiber, W. E., 1986: Case studies of thunderstorms initiated by radar-observed

- convergence lines. *Mon. Wea. Rev.*, **114**, 2256-2266.
- Ulanski, S. L., and M. Garstang, 1978: The role of surface divergence and vorticity in the life circle of convective rainfall. Part I: Observation and analysis. *J. Atmos. Sci.*, **35**, 1047-1062.
- Vickers, G., 1992: *1992 Alberta Weather Centre summer severe weather program*. Western Region, Atmospheric Environment Service, Environment Canada, 30 pp.
- Waldteufel, P., and H. Corbin, 1979: On the analysis of single Doppler radar data. *J. Appl. Meteor.*, **18**, 532-542.
- Wilson, J. W., and W. E. Schreiber, 1986: Initiation of convective storms at radar-observed boundary-layer convergence lines. *Mon. Wea. Rev.*, **114**, 2516-2536.

CHAPTER 4

NUMERICAL CLOUD MODEL

4.1 General Considerations

The advent and improvement of digital computers has made it possible to develop numerical models that can simulate realistically the evolution of clouds and cloud systems. The environment, in which clouds usually develop, is characterized by air flow which changes both its direction and magnitude with height. To realistically simulate cumulus development in such sheared conditions, a three-dimensional time-dependent cloud model is needed. However, the use of three spatial dimensions results in enormous storage requirements, particularly for simulations with high spatial resolution. This makes fully 3-D cloud models cumbersome for use when numerous sensitivity experiments are required. Due to these constraints, modelling studies of clouds often make the simplifying assumptions of either **slab-symmetry** or **axial-symmetry**.

Slab-symmetric models are suited for simulating cloud bands that are oriented perpendicular to an ambient flow which has unidirectional vertical shear (that is, wind does not veer with height). However, slab-symmetric models restrict the flow to a vertical plane producing unrealistic limitations on the flow, particularly for individual convective cells (e.g., Soong and Ogura 1973, Steiner 1973). Furthermore, the deviations of hydrostatic pressure tend to be overestimated in the slab-symmetric geometry, causing exaggerated perturbation pressure effects (Schlesinger 1984). Because of these concerns, an axi-symmetric cloud model is used in this study. This model is developed in cylindrical coordinates, and the azimuthal gradients of all quantities are set to zero. Axis-symmetric cloud models are suitable for simulating a single cumulus cell growing in an environment with little or no vertical shear. A more detailed discussion of the advantages of using the axisymmetry assumption rather than that of slab-symmetry is given in Chapter 5. This chapter describes the major assumptions, equations, parameterizations, boundary conditions and numerical schemes for the axi-symmetric cloud model.

4.2 Basic Assumptions

The axi-symmetric cloud model used here is an extended version of the model developed by Steiner (1982), Reuter and Yau (1987), and Guan and Reuter (1995). Reuter and Yau (1987) used this model to investigate mixing mechanisms in cumulus congestus clouds. Guan and Reuter (1995) extended the model by including a water cycle for warm-rain processes to simulate industrial cumulus clouds in their study. In this thesis, the model is further developed to incorporate large-scale convergence effects. The basic modelling assumptions are:

- 1) The equations of motion are formulated in a cylindrical coordinate system (r, θ, z) , and all azimuthal derivatives are set to zero (i.e., $\partial/\partial\theta = 0$).
- 2) The set of deep anelastic equations is used to eliminate numerically driven sound waves. This allows us to use a long time step (>3 seconds) which still ensures numerical stability.
- 3) A first-order sub-grid turbulence closure scheme is used, in which the Reynolds stresses are assumed to be proportional to the velocity deformation and the buoyancy frequency.
- 4) The effects of the earth's rotation and of friction at the earth's surface are neglected.
- 5) Surface heat flux and radiation effects are not included in the model.
- 6) Large-scale convergence incorporated in the model is time-independent, and maintained throughout the period of model simulation.
- 7) A bulk parameterization of the warm-rain process is used. The liquid water is subdivided into cloud water and rainwater. Cloud droplets follow the air motion passively, whereas rain drop falls with a mean terminal velocity consistent with the Marshall-Palmer drop size distribution.
- 8) Condensation occurs whenever the vapor mixing ratio exceeds the saturation value. Any cloud water in an unsaturated region evaporates until saturation is achieved. A threshold value for the auto-conversion from cloud water into rainwater is assumed.
- 9) The ice phase (freezing, melting, deposition and sublimation) is not considered.

In assumption 6), the mesoscale convergence is kept fixed (time-independent). In nature, however, the cloud convection will feed back (positively and negatively) into the convergence forcing. This interactive two-way feedback between small-scale and large-scale circulations is probably most important for long-lasting organized convection such as persistent rainbands, squall lines, or supercells. Based on the cases we choose, it is reasonable and simple to assume the mesoscale convergence time-independent.

Omitting ice phase microphysical processes in the model simulation requires some justification. Previous studies indicated that including ice microphysics is important for simulating the precipitation in squall lines that have extensive stratiform rain from broad rear anvils (e.g., Tao and Simpson 1993, Caniaux et al. 1994). Ice processes are also desirable when simulating tall tropical storms that develop in a neutrally stratified environment (e.g., Bennets and Rawlins 1981). However, ice microphysics does not affect the precipitation and the dynamics of clouds developing in strongly convective-unstable conditions with little vertical shear (Tripoli and Cotton 1982, Koenig and Murray 1984, Reuter 1987, 1988). Based on the selection of our thermodynamic soundings and the absence of ambient shear, it is expected that our model results would not change significantly if an ice phase microphysics parameterization were adopted.

4.3 Model Equations

The motion of air is governed by Newton's Second Law of Motion, which can be written in flux form as:

$$\frac{\partial u}{\partial t} = - \frac{1}{r} \frac{\partial(ru^2)}{\partial r} - \frac{1}{\rho_o} \frac{\partial(\rho_o w u)}{\partial z} - \frac{1}{\rho_o} \frac{\partial p'}{\partial r} \quad (4.1)$$

$$\frac{\partial w}{\partial t} = - \frac{1}{r} \frac{\partial(ruw)}{\partial r} - \frac{1}{\rho_o} \frac{\partial(\rho_o w^2)}{\partial z} - \frac{1}{\rho_o} \frac{\partial p'}{\partial z} + B \quad (4.2)$$

where u and w are the radial and vertical components of wind velocity in r and z directions, respectively; p is the air pressure, and ρ is the air density. B denotes buoyancy

given by

$$B = g \left[\frac{T'}{T_o} + 0.61q_v' - q_c - q_r - \frac{P'}{P_o} \right] \quad (4.3)$$

where q_v , q_c , and q_r denote the mixing ratios for water vapor, cloud water, and rainwater; g is the acceleration of gravity; and T is temperature. In (4.1), (4.2) and (4.3), the variables with subscripts “o” represent those in the environmental base state in hydrostatic equilibrium. All primed variables indicate departures from the hydrostatic base-state values. Any quantity not subscripted or primed represents the sum of the base state and the deviation. The mass continuity equation for deep convection, using the anelastic approximation, is written as:

$$\frac{1}{r} \frac{\partial(ru)}{\partial r} + \frac{1}{\rho_o} \frac{\partial(\rho_o w)}{\partial z} = 0 . \quad (4.4)$$

A diagnostic equation for perturbation pressure, p' , is obtained by taking the divergence of (4.1) and (4.2) combined with the continuity equation (4.4):

$$\frac{1}{r} \frac{\partial}{\partial r} \left(r \frac{\partial p'}{\partial r} \right) + \frac{\partial}{\partial z} \left(\frac{\partial p'}{\partial z} \right) = - \frac{1}{r} \frac{\partial(\rho_o r A_u)}{\partial r} - \frac{\partial(\rho_o A_w - \rho_o B)}{\partial z} + G \quad (4.5)$$

$$\text{and} \quad G = - \frac{\partial}{\partial t} \left[\frac{\rho_o}{r} \frac{\partial(ru)}{\partial r} + \frac{\partial(\rho_o w)}{\partial z} \right] . \quad (4.6)$$

Here A_u and A_w are the advective terms, consisting of the first two terms of the Right Hand Side (RHS) in (4.1) and (4.2). The term G corresponds to the rate of local change of the mass convergence flux. G is theoretically zero according to (4.4). However, in the numerical model, it is not strictly zero because of its finite-difference truncation errors. It is kept here to provide a negative feedback. Actual forms of A_u , A_w and G used in the numerical scheme will be presented in section 4.6.3.

Figure 4.1 shows, schematically, the microphysical processes used in the model.

According to this parameterization scheme, cloud water q_c first appears by the condensation of water vapor, but vapor is not condensed directly onto raindrops. Once sufficient cloud water has been produced, microphysical processes can then lead to the auto-conversion of some cloud water to rainwater. After auto-conversion has started to act, the amount of precipitation can then increase further through either auto-conversion or collection of cloud water, or both. Cloud droplets are assumed to evaporate instantaneously if the air is unsaturated.

Conservation of total non-precipitating water substance ($q_T = q_v + q_c$), and rainwater (q_r) is given by:

$$\frac{\partial q_T}{\partial t} = -\frac{1}{r} \frac{\partial(ruq_T)}{\partial r} - \frac{1}{\rho_o} \frac{\partial(\rho_o w q_T)}{\partial z} + EV_{rv} - CL_{cr} - AN_{cr} \quad (4.7)$$

$$\frac{\partial q_r}{\partial t} = -\frac{1}{r} \frac{\partial(ruq_r)}{\partial r} - \frac{1}{\rho_o} \frac{\partial(\rho_o w q_r)}{\partial z} - EV_{rv} + CL_{cr} + AN_{cr} + \frac{1}{\rho_o} \frac{\partial(\rho_o q_r V_r)}{\partial z} \quad (4.8)$$

where EV_{rv} denotes the rate of evaporation of rainwater to vapor, AN_{cr} the conversion rate of cloud water into rainwater due to the auto-conversion, and CL_{cr} the collection rate of cloud water by rainwater. Each of these terms has a double subscript, where the first subscript indicates the water phase being depleted and the second subscript is the water phase that is growing. The subscripts v , c , and r denote vapor, cloud and rain, respectively. V_r is the effective terminal fall speed of rainwater. The determination of EV_{rv} , CL_{cr} , AN_{cr} , and V_r is given in the next section.

Conservation of heat results in a prognostic equation for total specific entropy ($\phi = \phi_o + \phi'$),

$$\frac{\partial \phi}{\partial t} = -\frac{1}{r} \frac{\partial(ru\phi)}{\partial r} - \frac{1}{\rho_o} \frac{\partial(\rho_o w \phi)}{\partial z} + \frac{L \cdot EV_{rv}}{T} + \tilde{O}(\phi), \quad (4.9)$$

where L is the latent heat of vaporization and $\tilde{O}(\phi)$ represents the influence of precipitation fallout on ϕ . We assume that $\tilde{O}(\phi)$ is negligible. However, $\tilde{O}(\phi)$ should be

modelled or parameterized in some conditions. The total entropy per unit mass, ϕ , is given by

$$\begin{aligned}\phi(r, z, t) &= \phi_o(z) + \phi'(r, z, t) \\ &= C_{pd} \ln T - R_d \ln p + \frac{Lq_v}{T} + const\end{aligned}\quad (4.10)$$

$$\text{with } \begin{cases} \phi_o(z) = C_{pd} \ln T_o - R_d \ln p_o + \frac{Lq_{vo}}{T_o} + const \\ \phi'(r, z, t) = C_{pd} \ln\left(1 + \frac{T'}{T_o}\right) - R_d \ln\left(1 + \frac{p'}{p_o}\right) + \frac{L(q_v' T_o - q_{vo} T')}{T_o(T_o + T')} + const \end{cases} \quad (4.11)$$

where R_d is the gas constant for dry air, and C_{pd} the specific heat capacity at constant pressure. Eq. (4.9) ensures the conservation of total entropy over all liquid water phase changes.

4.4 Parameterization of Microphysical Processes

The cloud physics parameterization for warm-rain production follows Kessler's (1969) bulk-water scheme.

1) The autoconversion rate of cloud water to rainwater, AN_{cr} (s^{-1}), is given by (Kessler 1969, Liu and Orville 1969):

$$AN_{cr} = \begin{cases} 10^{-3} (q_c - \beta) & q_c > \beta \\ 0 & q_c \leq \beta \end{cases} \quad (4.12)$$

where parameter β is the cloud water mixing ratio threshold, assumed to be 10^{-3} kg kg⁻¹.

2) The collection rate of rainwater by sweeping out cloud water, CL_{cr} (s^{-1}), is given by (Innocentini and Caetano 1992):

$$CL_{cr} = 2.2 q_c q_r^{0.875} . \quad (4.13)$$

The rainwater mixing ratio increases as a result of the large falling drops intercepting and collecting small cloud droplets lying in their paths.

3) The rate of evaporation of rainwater is given by (Innocentini and Caetano 1992):

$$EV_{rv} = \begin{cases} 0.2 q_r^{0.675} (q_{vs} - q_v) & q_v < q_{vs} \\ 0 & q_v \geq q_{vs} \end{cases} \quad (4.14)$$

where q_{vs} is the saturated vapor mixing ratio with respect to a plane surface of liquid water.

4) The effective terminal fall speed of rainwater, V_t (ms^{-1}), is given by:

$$V_t = 21.18 q_r^{0.2} . \quad (4.15)$$

This is based on the Marshall-Palmer drop size distribution with a constant slope (Marshall and Palmer 1948).

4.5 Subgrid Turbulence Parameterization

A field variable X can be decomposed as (Cotton and Tripoli 1978, and Tripoli and Cotton 1980):

$$X(r,z,t) = \overline{X}(r,z,t) + X^*(r,z,t) = X_o(z) + \overline{X'}(r,z,t) + X^*(r,z,t) \quad (4.16)$$

where the overbar represents the average taken over a given numerical grid box and one time step, the superscript star represents the deviation from that grid-averaged value, and the subscript "o" denotes the horizontally-averaged basic reference state in hydrostatic balance. The primed quantity is a deviation from that basic state value.

Applying grid-volume averaging to (4.1), (4.2), (4.7) to (4.9) results in:

$$\frac{\partial \bar{u}}{\partial t} = -\bar{A}_u - \frac{1}{\rho_o} \frac{\partial \bar{p}'}{\partial r} + \bar{F}_u \quad (4.17)$$

$$\frac{\partial \bar{w}}{\partial t} = -\bar{A}_w - \frac{1}{\rho_o} \frac{\partial \bar{p}'}{\partial z} + \bar{B} + \bar{F}_w \quad (4.18)$$

$$\frac{\partial \bar{q}_T}{\partial t} = -\bar{A}_{q_T} + \overline{EV}_{rv} - \overline{CL}_{cr} - \overline{AN}_{cr} + \bar{F}_{q_T} \quad (4.19)$$

$$\frac{\partial \bar{q}_r}{\partial t} = -\bar{A}_{q_r} - \overline{EV}_{rv} + \overline{CL}_{cr} + \overline{AN}_{cr} + \frac{1}{\rho_o} \frac{\partial(\rho_o \bar{q}_r \bar{V}_r)}{\partial z} + \bar{F}_{q_r} \quad (4.20)$$

$$\frac{\partial \bar{\phi}}{\partial t} = -\bar{A}_\phi + \frac{L \cdot \overline{EV}_{rv}}{\bar{T}} + \bar{F}_\phi \quad (4.21)$$

The grid-averaged advective term \bar{A}_Q is given by:

$$\bar{A}_Q = \frac{1}{r} \frac{\partial(r \bar{u} \bar{Q})}{\partial r} + \frac{1}{\rho_o} \frac{\partial(\rho_o \bar{w} \bar{Q})}{\partial z} \quad (4.22)$$

where Q is any of u , w , q_r , q_r , and ϕ . The grid-averaged eddy term \bar{F}_Q is given by:

$$\bar{F}_Q = -\frac{1}{r} \frac{\partial(r \overline{u'Q'})}{\partial r} - \frac{1}{\rho_o} \frac{\partial(\rho_o \overline{w'Q'})}{\partial z} \quad (4.23)$$

It should be pointed out that for the case of radial velocity component, the eddy flux with one extra term is given by:

$$\overline{F_u} = -\frac{1}{r} \frac{\partial(r \overline{u'u'})}{\partial r} + \frac{\overline{v'v'}}{r} - \frac{1}{\rho_v} \frac{\partial(\rho_v \overline{w'u'})}{\partial z}. \quad (4.24)$$

The term $-(\overline{v'v'}/r)$ arises from the correlation effect of turbulent tangential motion. The $\overline{u'u'}$, $\overline{u'w'}$, and $\overline{w'w'}$ are the usual Reynolds stress terms.

After the averaging, a closure problem arises because the eddy fluxes $\overline{F_Q}$ become additional variables in the equations for the mean variables. Therefore, these fluxes must be determined from known quantities in order for the system of equations governing the air motion in cloud to remain a closed set. The parameterization scheme used most commonly for subgrid-scale turbulence is adopted. It assumes that the Reynolds fluxes are proportional to the gradients of the corresponding quantities. The thermodynamic and water subgrid scale fluxes are parameterized in the same way, with an eddy coefficient proportional to that for momentum. For velocity variables, the turbulent fluxes are parameterized by:

$$\begin{aligned} -\overline{u'u'} &= 2K_m \left| \frac{\partial \bar{u}}{\partial r} \right| \\ -\overline{v'v'} &= 2K_m \frac{|\bar{u}|}{r} \\ -\overline{u'w'} &= K_m \left(\frac{\partial \bar{u}}{\partial z} + \frac{\partial \bar{w}}{\partial r} \right) \\ -\overline{w'w'} &= 2K_m \left| \frac{\partial \bar{w}}{\partial z} \right|, \end{aligned} \quad (4.25)$$

while for the scalar variables q_T , q_r , and ϕ , the fluxes appear as

$$\begin{aligned}
-\overline{u'q_T'} &= K_s \frac{\partial \overline{q_T}}{\partial r} ; & -\overline{w'q_T'} &= K_s \frac{\partial \overline{q_T}}{\partial z} \\
-\overline{u'q_r'} &= K_s \frac{\partial \overline{q_r}}{\partial r} ; & -\overline{w'q_r'} &= K_s \frac{\partial \overline{q_r}}{\partial z} \\
-\overline{u'\phi'} &= K_s \frac{\partial \overline{\phi}}{\partial r} ; & -\overline{w'\phi'} &= K_s \frac{\partial \overline{\phi}}{\partial z}
\end{aligned} \tag{4.26}$$

where K_m and K_s are, respectively, the eddy exchange coefficients for momentum and all scalar variables. In this thesis, the scheme of $K_s=K_m$ (Hill 1974) is used. In (4.18) to (4.21), we approximate \overline{B} with B , \overline{EV}_r with EV_r , \overline{CL}_{cr} with CL_{cr} and \overline{AN}_{cr} with AN_{cr} . These particular choices are not always suitable in large-scale models.

Substituting (4.22)-(4.26) into (4.17)-(4.21), the basic prognostic equations become

$$\begin{aligned}
\frac{\partial u}{\partial t} &= -\frac{1}{r} \frac{\partial(ru^2)}{\partial r} - \frac{1}{\rho_o} \frac{\partial(\rho_o w u)}{\partial z} - \frac{1}{\rho_o} \frac{\partial p'}{\partial r} \\
&+ \frac{1}{r} \frac{\partial}{\partial r} [2rK_m \frac{\partial u}{\partial r}] - 2K_m \frac{u}{r^2} + \frac{1}{\rho_o} \frac{\partial}{\partial z} [\rho_o K_m (\frac{\partial u}{\partial z} + \frac{\partial w}{\partial r})]
\end{aligned} \tag{4.27}$$

$$\begin{aligned}
\frac{\partial w}{\partial t} &= -\frac{1}{r} \frac{\partial(ruw)}{\partial r} - \frac{1}{\rho_o} \frac{\partial(\rho_o w^2)}{\partial z} - \frac{1}{\rho_o} \frac{\partial p'}{\partial z} + B \\
&+ \frac{1}{r} \frac{\partial}{\partial r} [rK_m (\frac{\partial u}{\partial z} + \frac{\partial w}{\partial r})] + \frac{1}{\rho_o} \frac{\partial}{\partial z} [2\rho_o K_m \frac{\partial w}{\partial z}]
\end{aligned} \tag{4.28}$$

$$\begin{aligned}
\frac{\partial q_T}{\partial t} &= -\frac{1}{r} \frac{\partial(ruq_T)}{\partial r} - \frac{1}{\rho_o} \frac{\partial(\rho_o w q_T)}{\partial z} + EV_r - CL_{cr} - AN_{cr} \\
&+ \frac{1}{r} \frac{\partial}{\partial r} [rK_s \frac{\partial q_T}{\partial r}] + \frac{1}{\rho_o} \frac{\partial}{\partial z} [\rho_o K_s \frac{\partial q_T}{\partial z}]
\end{aligned} \tag{4.29}$$

$$\begin{aligned} \frac{\partial q_r}{\partial t} = & -\frac{1}{r} \frac{\partial(ruq_r)}{\partial r} - \frac{1}{\rho_o} \frac{\partial(\rho_o w q_r)}{\partial z} - EV_r + CL_{cr} + AN_{cr} + \frac{1}{\rho_o} \frac{\partial(\rho_o g_r V_r)}{\partial z} \\ & + \frac{1}{r} \frac{\partial}{\partial r} [rK_s \frac{\partial q_r}{\partial r}] + \frac{1}{\rho_o} \frac{\partial}{\partial z} [\rho_o K_s \frac{\partial q_r}{\partial z}] \end{aligned} \quad (4.30)$$

$$\begin{aligned} \frac{\partial \phi}{\partial t} = & -\frac{1}{r} \frac{\partial(ru\phi)}{\partial r} - \frac{1}{\rho_o} \frac{\partial(\rho_o w \phi)}{\partial z} + \frac{L \cdot EV_r}{T} \\ & + \frac{1}{r} \frac{\partial}{\partial r} [rK_s \frac{\partial \phi}{\partial r}] + \frac{1}{\rho_o} \frac{\partial}{\partial z} [\rho_o K_s \frac{\partial \phi}{\partial z}] . \end{aligned} \quad (4.31)$$

Because only grid-volume averages now appear in the equations, the overbars have been omitted. Following the scheme of Hill (1974), the eddy exchange coefficient for momentum is assumed to be of the form:

$$K_m = \begin{cases} 0 & R_i > 0.25 \\ \lambda l^2 (f_s + f_b) & R_i < 0.25 \end{cases} \quad (4.32)$$

where $l = (\Delta r \Delta z)^{1/2}$ is a representative grid spacing with Δr and Δz denoting the grid spacings in the radial and vertical directions, respectively; λ , a dimensionless constant, is chosen to be 0.4, and R_i is the Richardson number. The factors f_s and f_b represent velocity-deformation (shear) and buoyancy frequencies. The shear frequency is given by

$$f_s = \sqrt{\left(\frac{\partial u}{\partial z} + \frac{\partial w}{\partial r}\right)^2 + 2\left[\left(\frac{\partial u}{\partial r}\right)^2 + \left(\frac{u}{r}\right)^2 + \left(\frac{\partial w}{\partial z}\right)^2\right]} . \quad (4.33)$$

The buoyancy frequency f_b is determined by the frequency scale of atmospheric oscillations:

$$f_b = \begin{cases} 0 & R_i > 0 \\ \sqrt{-g \frac{\gamma_{vad} - \gamma_{venv}}{T}} & R_i < 0 \end{cases} \quad (4.34)$$

The Richardson number is defined as

$$R_i = \frac{g (\gamma_{vad} - \gamma_{venv})}{T \left(\frac{\partial u}{\partial z} \right)^2} \quad (4.35)$$

where γ_{vad} and γ_{venv} are the moist adiabatic lapse rate and the environmental virtual temperature lapse rate, respectively. Their difference can be approximated as

$$\gamma_{vad} - \gamma_{venv} = \frac{g \alpha}{C_{pd}} + \frac{\partial T}{\partial z} + 0.61 T \frac{\partial q_v}{\partial z} \quad (4.36)$$

$$\text{where } \alpha = \begin{cases} 1 & \text{For unsaturated air} \\ \frac{1 + \frac{L q_{vs}}{R_d T}}{1 + \frac{0.622 L^2 q_{vs}}{C_{pd} R_d T^2}} & \text{For saturated air} \end{cases} \quad (4.37)$$

4.6 Numerical Techniques

4.6.1 Stretched coordinate

A stretched coordinate (s, θ, z) was used in the axi-symmetric cloud model to solve the equations on a finite-difference grid with higher horizontal resolution near the central axis than elsewhere (Steiner 1982, Reuter and Yau 1987, Guan and Reuter 1995). This

grid arrangement is obtained from the transformation of horizontal coordinate r to a coordinate s so that Δr is smaller near the central axis and larger toward the lateral boundary, while the interval Δs is equally spaced. The r and s are related by the monotonically increasing function

$$r = \frac{R}{2C} \ln \left(\frac{A+s}{A-s} \right) \quad (4.38)$$

where R is the half-width of the domain in the radial direction. Constants A and C are determined at the beginning of every simulation from the relations

$$\begin{aligned} n\Delta s &= A \tanh C \\ \text{and} \\ m\Delta s &= A \tanh (Ck) , \end{aligned} \quad (4.39)$$

where n is the total number of grid points in the horizontal, and m is the number of grid points within a distance of kR from the axis (i.e., the number of grid points occupying portion k of the total radial distance modeled). Eq. (4.39) is solved by an iterative method based on the selection of optional parameters m , n , and k .

From (4.38), the following expressions are derived:

$$\begin{aligned} r' &= \frac{dr}{ds} = \frac{AR}{C} \cdot \frac{1}{(A+s)(A-s)} \\ \frac{\partial}{\partial r} &= \frac{1}{r'} \cdot \frac{\partial}{\partial s} \\ u &= \frac{dr}{dt} = \frac{dr}{ds} \cdot \frac{ds}{dt} = r' \cdot \dot{s} . \end{aligned} \quad (4.40)$$

With the use of (4.40), model prognostic equations (4.27)-(4.31) in the stretched coordinate (s, θ, z) become

$$\begin{aligned} \frac{\partial \dot{s}}{\partial t} = & -\frac{1}{rr'^2} \frac{\partial}{\partial s}(rr'^2 \dot{s}^2) - \frac{1}{\rho_o} \frac{\partial}{\partial z}(\rho_o \dot{s} w) - \frac{1}{\rho_o r'^2} \frac{\partial p'}{\partial s} - \frac{2K_m \dot{s}}{r^2} \\ & + \frac{1}{rr'^2} \frac{\partial}{\partial s} \left[\frac{2rK_m}{r'} \frac{\partial}{\partial s}(r'\dot{s}) \right] + \frac{1}{\rho_o r'} \frac{\partial}{\partial z} \left[\rho_o K_m \left(r' \frac{\partial \dot{s}}{\partial z} + \frac{1}{r'} \frac{\partial w}{\partial s} \right) \right] \end{aligned} \quad (4.41)$$

$$\begin{aligned} \frac{\partial w}{\partial t} = & -\frac{1}{rr'} \frac{\partial}{\partial s}(rr' \dot{s} w) - \frac{1}{\rho_o} \frac{\partial}{\partial z}(\rho_o w^2) + B - \frac{1}{\rho_o} \frac{\partial p'}{\partial z} \\ & + \frac{1}{rr' \partial s} \left[rK_m \left(r' \frac{\partial \dot{s}}{\partial z} + \frac{1}{r'} \frac{\partial w}{\partial s} \right) \right] + \frac{1}{\rho_o} \frac{\partial}{\partial z} \left(2\rho_o K_m \frac{\partial w}{\partial z} \right) \end{aligned} \quad (4.42)$$

$$\begin{aligned} \frac{\partial q_T}{\partial t} = & -\frac{1}{rr'} \frac{\partial}{\partial s}(rr' \dot{s} q_T) - \frac{1}{\rho_o} \frac{\partial}{\partial z}(\rho_o w q_T) + EV_{r'} - CL_{cr} - AN_{cr} \\ & + \frac{1}{rr' \partial s} \left(\frac{rK_s}{r'} \frac{\partial q_T}{\partial s} \right) + \frac{1}{\rho_o} \frac{\partial}{\partial z} \left(\rho_o K_s \frac{\partial q_T}{\partial z} \right) \end{aligned} \quad (4.43)$$

$$\begin{aligned} \frac{\partial q_r}{\partial t} = & -\frac{1}{rr'} \frac{\partial}{\partial s}(rr' \dot{s} q_r) - \frac{1}{\rho_o} \frac{\partial}{\partial z}(\rho_o w q_r) + \frac{1}{\rho_o} \frac{\partial}{\partial z}(\rho_o V_r q_r) \\ & - EV_{r'} + CL_{cr} + AN_{cr} + \frac{1}{rr' \partial s} \left(\frac{rK_s}{r'} \frac{\partial q_r}{\partial s} \right) + \frac{1}{\rho_o} \frac{\partial}{\partial z} \left(\rho_o K_s \frac{\partial q_r}{\partial z} \right) \end{aligned} \quad (4.44)$$

$$\begin{aligned} \frac{\partial \phi}{\partial t} = & -\frac{1}{rr'} \frac{\partial}{\partial s}(rr' \dot{s} \phi) - \frac{1}{\rho_o} \frac{\partial}{\partial z}(\rho_o w \phi) + \frac{L \cdot EV_{r'}}{T} \\ & + \frac{1}{rr' \partial s} \left(\frac{rK_s}{r'} \frac{\partial \phi}{\partial s} \right) + \frac{1}{\rho_o} \frac{\partial}{\partial z} \left(\rho_o K_s \frac{\partial \phi}{\partial z} \right) . \end{aligned} \quad (4.45)$$

4.6.2 Finite space difference scheme

The above differential equations are solved using a staggered finite-difference grid scheme. The staggered grid arrangement is shown in Figure 4.2. The velocity component normal to the sides of the grid boxes is computed at the midpoints of the sides; all other variables are computed at the centre of each box. That is, all variables except s' and w are computed at $\{(i+1/2)\Delta s, (j+1/2)\Delta z\}$, shown as \bullet in the diagram; s' (or u) at $\{i\Delta s, (j+1/2)\Delta z\}$ shown as \times , and w at $\{(i+1/2)\Delta s, j\Delta z\}$ shown as \circ . The subscripts i ($=1, 2, \dots, NH$) and j ($=1, 2, \dots, NV$) are the grid point indices in radial and vertical directions, respectively, with NH and NV denoting the total number of grid points in the two directions.

A second-order, non-diffusive centred differencing method is used to calculate all derivatives, and the following notations are employed:

$$\begin{aligned}
 \delta_s X &= \frac{X_{i-\frac{1}{2},j} - X_{i+\frac{1}{2},j}}{\Delta s} \\
 \delta_z X &= \frac{X_{i,j+\frac{1}{2}} - X_{i,j-\frac{1}{2}}}{\Delta z} \\
 \bar{X}^s &= \frac{X_{i-\frac{1}{2},j} + X_{i+\frac{1}{2},j}}{2} \\
 \bar{X}^z &= \frac{X_{i,j+\frac{1}{2}} + X_{i,j-\frac{1}{2}}}{2} \\
 \delta_{2t} X &= \frac{X^{(\tau+1)} - X^{(\tau-1)}}{2 \Delta t}
 \end{aligned} \tag{4.46}$$

where τ is the time index. As seen from the last expression in (4.46), a leapfrog scheme is used for the time integration.

4.6.3 Finite difference equations

The finite-difference forms of prognostic equations (4.41)-(4.45) are:

$$\delta_{2t} \dot{s} = A_s^{(\tau)} - \frac{1}{\rho_o r_s'^{1/2}} \delta_s p'^{(\tau)} + F_s^{(\tau-1)} \quad (4.47)$$

$$\delta_{2t} w = A_w^{(\tau)} - \frac{1}{\rho_o} \delta_z p'^{(\tau)} + \bar{B} z^{(\tau)} + F_w^{(\tau-1)} \quad (4.48)$$

$$\delta_{2t} q_T = A_{q_T}^{(\tau)} + EV_{r'}^{(\tau)} - CL_{cr}^{(\tau)} - AN_{cr}^{(\tau)} + F_{q_T}^{(\tau-1)} \quad (4.49)$$

$$\delta_{2t} q_r = A_{q_r}^{(\tau)} + \frac{1}{\rho_o} \delta_z (\rho_o q_r V_r)^{(\tau)} - EV_{r'}^{(\tau)} + CL_{cr}^{(\tau)} + AN_{cr}^{(\tau)} + F_{q_r}^{(\tau-1)} \quad (4.50)$$

$$\delta_{2t} \phi = A_\phi^{(\tau)} + L \left(\frac{EV_{r'}}{T} \right)^{(\tau)} + F_\phi^{(\tau-1)} \quad (4.51)$$

where

$$A_s = -\frac{1}{r_s r_s'^{1/2}} \delta_s (r r'^{1/2} \bar{s}^s \bar{s}^s) - \frac{1}{\rho_o r_s'} \delta_z (\rho_o r_s' \bar{s}^z \bar{w}^s) \quad (4.52)$$

$$A_w = -\frac{1}{r r'} \delta_s (r_s r_s' \bar{s}^z \bar{w}^s) - \frac{1}{\rho_o} \delta_z (\rho_o \bar{w}^z \bar{w}^z) \quad (4.53)$$

$$A_{q_T} = -\frac{1}{r r'} \delta_s (r_s r_s' \bar{s} \bar{q}_T^s) - \frac{1}{\rho_o} \delta_z (\rho_o w \bar{q}_T^z) \quad (4.54)$$

$$A_{q_r} = -\frac{1}{r r'} \delta_s (r_s r_s' \bar{s} \bar{q}_r^s) - \frac{1}{\rho_o} \delta_z (\rho_o w \bar{q}_r^z) \quad (4.55)$$

$$A_\phi = -\frac{1}{r r'} \delta_s(r_s r_s' \dot{s} \bar{\phi}^s) - \frac{1}{\rho_o} \delta_z(\rho_o w \bar{\phi}^z) \quad (4.56)$$

$$F_{\dot{s}} = \frac{1}{r_s r_s'^2} \delta_s \left[\frac{2r K_m}{r'} \ddot{s}(r_s' \dot{s}) \right] - \frac{2\overline{K_m^s} \dot{s}}{r_s^2} + \frac{1}{\rho_o r_s'} \delta_z(\rho_o \overline{K_m^s} r_s' \delta_z \dot{s} + \frac{1}{r_s'} \delta_s w) \quad (4.57)$$

$$F_w = \frac{1}{r r'} \delta_s [r_s \overline{K_m^s} (r_s' \delta_z \dot{s} + \frac{1}{r_s'} \delta_s w)] + \frac{1}{\rho_o} \delta_z(2\rho_o K_m \delta_z w) \quad (4.58)$$

$$F_{q_T} = \frac{1}{r r'} \delta_s (\overline{K_s^s} \frac{r_s}{r_s'} \delta_s q_T) + \frac{1}{\rho_o} \delta_z (\overline{K_s^z} \rho_o \delta_z q_T) \quad (4.59)$$

$$F_{q_r} = \frac{1}{r r'} \delta_s (\overline{K_s^s} \frac{r_s}{r_s'} \delta_s q_r) + \frac{1}{\rho_o} \delta_z (\overline{K_s^z} \rho_o \delta_z q_r) \quad (4.60)$$

$$F_\phi = \frac{1}{r r'} \delta_s (\overline{K_s^s} \frac{r_s}{r_s'} \delta_s \phi) + \frac{1}{\rho_o} \delta_z (\overline{K_s^z} \rho_o \delta_z \phi) \quad (4.61)$$

Here, r_s and r_s' are the radial ranges at points where s and \dot{s} are computed (i.e., at location $\{(i\Delta s, (j+1/2)\Delta z)\}$), while unsubscripted r and r' are the values at the centres of grid boxes (at $\{(i+1/2)\Delta s, (j+1/2)\Delta z\}$). Advective and turbulent sub-grid terms are denoted by A_Q and F_Q where Q can be any of \dot{s} , w , q_T , q_r , or ϕ . All terms involving turbulence factors are lagged by one single time step.

The finite-difference form of the perturbation pressure equation (4.5) is given by:

$$\begin{aligned} \delta_z \delta_z p'^{(\tau)} + \frac{1}{rr'} \delta_s \left(\frac{r_s}{r_s'} \delta_s p'^{(\tau)} \right) &= \frac{\rho_o}{rr'} \delta_s [rr_s' (A_s^{(\tau)} + F_s^{(\tau-1)})] \\ &+ \delta_z [\rho_o (A_w^{(\tau)} + F_w^{(\tau-1)} + \bar{B}^{\tau})] \\ &- \left[\frac{\dot{D}^{(\tau+1)} - \dot{D}^{(\tau-1)}}{2rr' \Delta t} \right] . \end{aligned} \quad (4.62)$$

$$\text{where} \quad \dot{D} = \frac{\rho_o}{rr'} \delta_s (r_s r_s' \dot{s}) + \delta_z (\rho_o w) . \quad (4.63)$$

Due to computational round-off errors, \dot{D} is not always zero at each time step. Following Harlow and Welch (1965), $\dot{D}^{(\tau+1)}$ is set to zero in (4.62) whereas $\dot{D}^{(\tau-1)}$ is retained. This treatment ensures that the magnitude of the divergence is prevented from increasing with time (negative feedback).

4.6.4 Time integration scheme

The model uses the leapfrog scheme shown in (4.46) for time integration of the marching equations. However, the turbulent terms are lagged in time. Initially, and after every 20 time steps, a mixing procedure based on Gordon (1978) is invoked to prevent the possible splitting of solutions at odd and even time steps. This involves a forward difference over $1/8$ of the usual time step, followed by centred differences over $1/8$, $1/4$, and $1/2$ of the usual time step, before employing the regular centred time difference procedure. This procedure is quite economical for several-hour simulations. The time step is set to 3 seconds for the convective case study which will be discussed in Chapter 5, and 5 seconds for the stratiform precipitation case in Chapter 6.

4.6.5 Numerical adjustment procedures for saturation

When integrating (4.7), (4.8) and (4.9) to obtain the values of q_v , q_c , q_r and ϕ at new time steps, it is necessary to determine whether the air is saturated in order to

consider the evaporation of rainwater and cloud water. The logical analysis introduced by Ogura (1963) is adopted in the model. The empirical formula for saturation vapor pressure with respect to water is (Bolton 1980):

$$e_s(T) = a \exp\left[\frac{b(T-c)}{T-d}\right] \quad (4.64)$$

where $a=611.2 \text{ Nm}^{-2}$, $b=17.67$, $c=273.15 \text{ K}$, and $d=29.65 \text{ K}$. Assuming that $T = T_o(z) + T'$, $|T'| \leq 3 \text{ K}$, $|T_o(z)-d| \leq 200 \text{ K}$, and expanding the exponential on RHS of (4.64) results in

$$e_s(T) = e_s(T_o) [1 + H_1(z) T' + H_2(z) T'^2]$$

$$\text{where } H_1(z) = \frac{b(c-d)}{[T_o(z)-d]^2} \quad (4.65)$$

$$H_2(z) = \frac{b^2 [2c-d-T_o(z)]}{2 [T_o(z)-d]^3}$$

During the extension from (4.64) to (4.65), all terms with magnitudes two orders less than the largest one have been neglected. Thus, the saturation mixing ratio $q_{vs} = 0.622 e_s/(p-e_s)$ can be approximated by

$$q_{vs} = \frac{0.622 e_s(T_o)}{p_o} [1 + H_1(z) T' + H_2(z) T'^2] \left[1 + \frac{e_s(T_o)}{p_o}\right] \quad (4.66)$$

If the air is saturated, we neglect the variation of q_{vs} over the time step and assume q_v remains constant. Therefore, sources contributing to both q_v and q_c are added to the existing q_c to find the amount of q_c available over the time step. If $q_c=0$, all microphysical sources contributing to both q_c and q_v are added to q_v . Because of the truncation error associated with the finite-difference scheme, negative rainwater values may be produced. Obviously, this is not physically correct and an adjustment is needed to increase the

predicted negative rainwater mixing ratio to zero by subtracting from the vapor mixing ratio in the same grid box.

The values q_v and q_c are determined according to the following steps, once ϕ , q_T and q_r are determined at a given time step:

Step 1: The negative q_r is eliminated.

If $q_r < 0$, q_T is adjusted to $q_T + q_r$, and $q_r = 0$.

Step 2: The q_{vs} value is determined.

Assuming that the air is unsaturated, ϕ' and q_T' can be obtained by subtracting ϕ_0 and q_{T0} from ϕ and q_T . Eq. (4.11) is adopted to compute T' using either $p'=0$ or the p' value obtained from the previous time step. Then, a value of q_{vs} is computed from (4.66) using the value of T' .

Step 3: Saturation is examined by checking the differences between q_{vs} and q_T .

If $q_T < q_{vs}$, the air must be unsaturated and hence $q_v' = q_T - q_{vs} = q_T'$ and $q_c = 0$. In this case, the T' is indeed the value which is obtained from (4.11) in Step 2. Then Step 4 will be carried out. Otherwise (i.e., $q_T > q_{vs}$), the assumption of subsaturation is clearly false. Therefore, $q_v (= q_{vs} + q_v') = q_{vs}$, and $q_c = q_T - q_v$. The T' is recomputed based on (4.11) using known ϕ' , q_v' , and p' .

Step 4: Rain evaporation is considered.

If i) the air is unsaturated, ii) $q_r > 0$, and iii) the evaporation effects have not been adjusted yet, the evaporated water (following (4.14)) must be subtracted from q_r . As a result, both q_T and ϕ must be adjusted to new values.

4.7 Boundary Conditions

Since the numerical domain is finite, appropriate boundary conditions must be

specified along the sides of the model domain. The top and bottom boundaries are assumed to be flat, rigid and smooth; that is, there is no transfer of vapor, cloud water, or entropy through these boundaries. However, rain water is allowed to leave the domain at the bottom. In summary,

$$\left. \begin{aligned} w &= 0 \\ \frac{\partial u}{\partial z} &= \frac{\partial q_T}{\partial z} = \frac{\partial \phi}{\partial z} = 0 \\ \frac{\partial K_m}{\partial z} &= \frac{\partial K_s}{\partial z} = \frac{\partial \rho_o}{\partial z} = 0 \end{aligned} \right\} \text{ at } z = 0, Z_H \quad (4.67)$$

$$\text{and } \frac{\partial q_r}{\partial z} = 0 \quad \text{at } z = Z_H \quad (4.68)$$

where Z_H is the domain height. Due to the staggered grid used in the model, the vertical derivatives at the top and bottom boundaries are set to zero to prevent turbulent diffusion across the boundaries in computing eddy diffusion terms.

Substituting (4.67) into the equation of vertical motion (4.48) results in the boundary condition for perturbation pressure p' ,

$$\frac{1}{\rho_o} \delta_z p' + \bar{B}^z = 0 \quad \text{at } z = 0, Z_H \quad (4.69)$$

The lateral boundary conditions (LBCs) are more problematical. Difficulties associated with lateral boundaries are mostly avoided by the 'closed box' assumption, that is, no flow is allowed through the sides (e.g., Steiner 1982, Reuter and Yau 1987, and Guan and Reuter 1995). In this study, the model is modified in LBC. The approach is to implement a one-way open LBC with a prescribed vertical profile of radial flow into the cylindrical domain. Along the central axis of the domain, the variables are assumed to obey:

$$u = 0 \quad \text{at } r = 0$$

$$\frac{\partial w}{\partial r} = \frac{\partial q_T}{\partial r} = \frac{\partial q_r}{\partial r} = \frac{\partial \phi}{\partial r} = \frac{\partial p'}{\partial r} = 0 \quad \text{at } r = 0, R. \quad (4.70)$$

The radial inflow and outflow at the model lateral boundary are determined by a height-dependent divergence as

$$Div(z) = \frac{1}{r} \frac{\partial [u(r,z) \cdot r]}{\partial r} \quad (4.71)$$

or $\delta_s(r_s, r'_s, \dot{s}) = r \cdot r' \cdot Div(z) \quad .$

During the determination of u (or s) at the lateral boundary, care has been given to assuring that there is no net influx of mass when integrating over the entire model domain. That is, all the air entering in the lower layers must exit the domain at higher levels. The magnitudes of low-level convergence and upper-level divergence, and the depths of convergent and divergent layers, follow the expression

$$\int_0^{Z_H} \rho(z) \cdot Div(z) dz = 0 \quad . \quad (4.72)$$

For a given divergence profile, the amounts of air inflow and outflow are determined by (4.71) and (4.72). However, Eq. (4.72) is only the necessary condition to ensure the conservation of total air mass flux over the entire domain when the finite-difference form of (4.72) is used in the model computation. To preserve the total air mass influx, the profile of u (or s) at the lateral boundary must also be readjusted to satisfy

$$\sum_{j=1}^{NV} \rho_j \cdot u_{NH,j} = 0 \quad . \quad (4.73)$$

In the view of assumption 6 in section 4.2, the inflow and outflow at the lateral boundary remain constant throughout the simulation period.

4.8 Initial Conditions

Initial temperature, pressure and humidity values are specified from a sounding observed in the cases under investigation. Using the assumption of horizontal uniformity, the sounding values of temperature and dew-point are linearly interpolated to grid-point levels throughout the model with given values of $p(z)$. The remaining quantities such as ρ , q_v , and ϕ are then calculated at all grid-point levels.

In contrast to previous versions of the model, the initial wind fields are non-quietescent in the present model. Radial wind components, in finite-difference form, are obtained from the profile of divergence according to

$$\dot{s}_{i+1, j+\frac{1}{2}} = \frac{r_{si} r'_{si} \dot{s}_{i, j+\frac{1}{2}} + r_i r'_i \text{Div}_{j+\frac{1}{2}}}{r_{si+1} r'_{si+1}} \quad (4.74)$$

with $\dot{s}_{i, j+\frac{1}{2}} = 0$ (i.e., zero radial wind speed at the central axis of the domain). Consistent with the radial wind field, the initial mesoscale vertical velocity components are specified by the deep anelastic continuity equation (4.4) and the assumption of zero vertical velocity at the surface ($w_{i+\frac{1}{2}, l} = 0$). The finite difference form of mesoscale vertical velocity at each level is

$$w_{i+\frac{1}{2}, j+1} = \frac{1}{\rho_{j+1}} [\rho_j w_{i+\frac{1}{2}, j} - \rho_{j+\frac{1}{2}} \cdot \text{Div}_{j+\frac{1}{2}} \cdot \Delta z] \quad (4.75)$$

Due to the convergence lifting, there is no need to initiate the convection with a temperature or moisture anomaly at low-levels (the "warm bubble" method). The major disadvantage of using the "bubble" method is that a simulated cloud is sensitive to the spatial dimensions of the initial perturbation (e.g., Reuter and Yau 1987). This is not the case when using horizontally uniform conditions with radially uniform lifting.

4.9 Summary

In this chapter, the axi-symmetric cloud model used in this work has been described in detail. Essentially, it is a nonhydrostatic, anelastic, moist cloud model which consists of five prognostic partial differential equations representing the dynamical, microphysical and thermodynamical processes occurring in cloud. A first-order closure scheme is employed to deal with sub-grid scale turbulent motions. A bulk-water parameterization technique is used to simulate cloud formation and warm-rain processes. The unique feature of the current version of the model is its ability to incorporate larger-scale convergence effects.

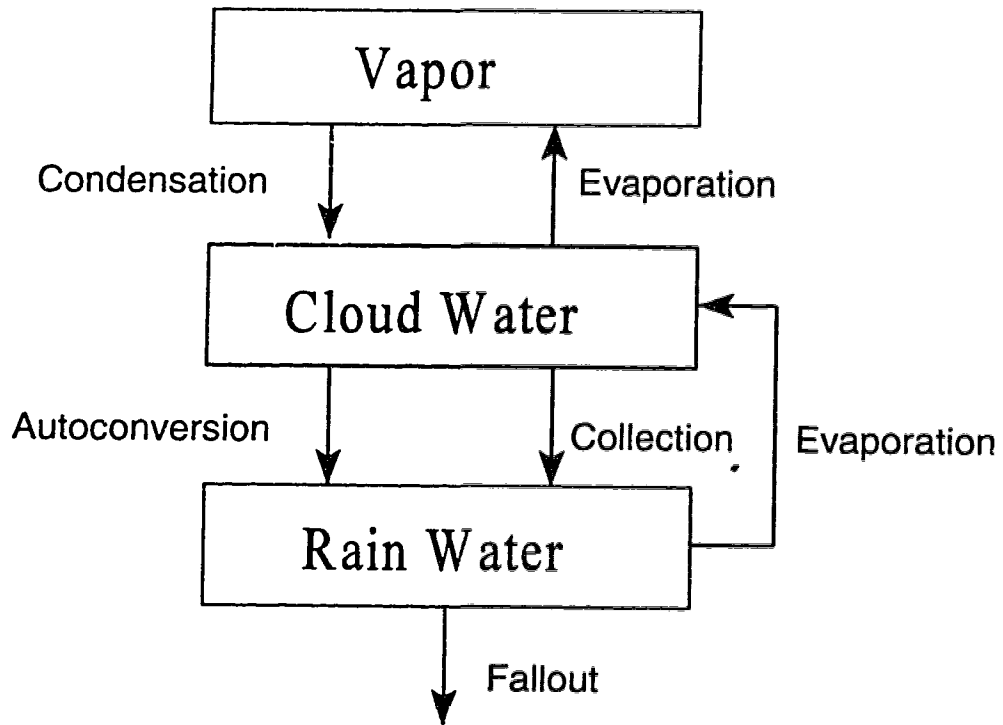


Figure 4.1 Flow diagram describing microphysical processes, including different paths for warm-rain formation.

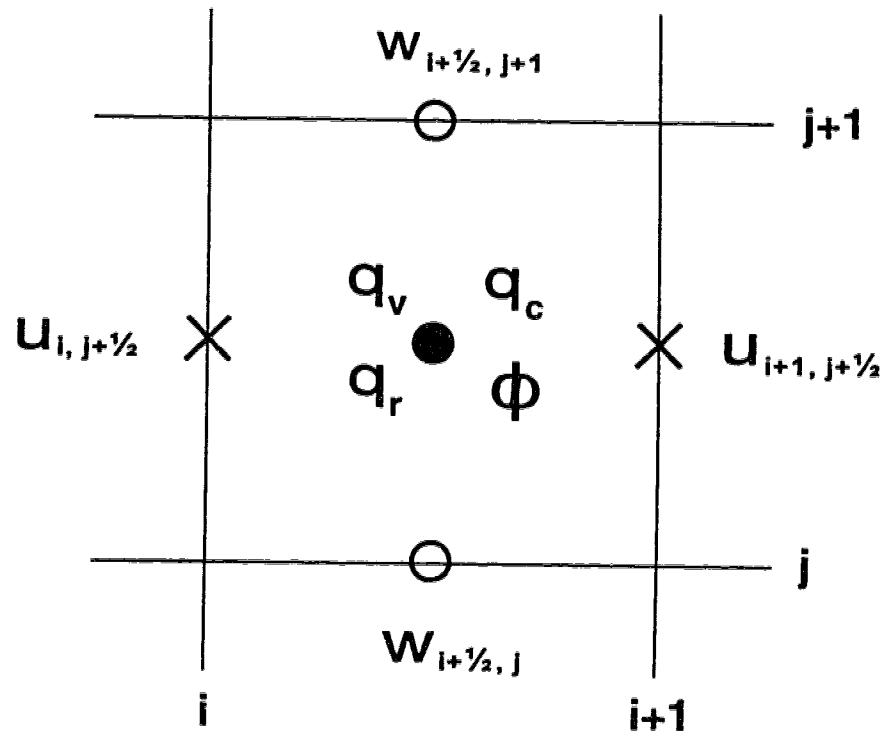


Figure 4.2 The staggered grid arrangement used in the centred difference scheme.

References

- Bennetts, D. A., and F. Rawlins, 1981: Parameterization of the ice-phase in a model of mid-latitude cumulonimbus convection and its influence on the simulation of cloud development. *Quart. J. Roy. Meteor. Soc.*, **107**, 477-502.
- Bolton, D., 1980: The computation of equivalent potential temperature. *Mon. Wea. Rev.*, **108**, 1046-1053.
- Caniaux, G., J.-L. Redelsperger, and J.-P. Lafore, 1994: A numerical study of the stratiform region of a fast-moving squall line. Part I: General description and water and heat budgets. *J. Atmos. Sci.*, **51**, 2046-2074.
- Cotton, W. R., and G. Tripoli, 1978: Cumulus convection in shear flow: three-dimensional numerical experiments. *J. Atmos. Sci.*, **35**, 1503-1521.
- Gordon, N. D., 1978: Numerical simulation of a long-lasting mesoscale squall line. Sc. D. Thesis, Massachusetts Institute of Technology, 219 pp.
- Guan, S., and G. W. Reuter, 1995: Numerical simulation of a rain shower affected by waste energy released from a cooling tower complex in a calm environment. *J. Appl. Meteor.*, **34**, 131-142.
- Harlow, F. H., and J. E. Welch, 1965: Numerical calculation of time dependent viscous incompressible flow of fluid with free surface. *Phys. Fluids*, **8**, 2182-2189.
- Hill, G. E., 1974: Factors controlling the size and spacing of cumulus clouds as revealed by numerical experiments. *J. Atmos. Sci.*, **31**, 646-673.
- Innocentini, V., and E. S. Caetano, 1992: A numerical study of the role of humidity in the updraft driven by moist slantwise convection. *J. Atmos. Sci.*, **49**, 1092-1106.
- Kessler, E., 1969: *On the distribution and continuity of water substance in atmospheric circulations. Meteor. Monograph*, **10**, No. 32, Amer. Meteor. Soc., Boston, 84 pp.
- Koenig, L. R., and W. R. Murray, 1984: Further theoretical studies of the role of splintering in cumulus glaciation. *Quart. J. Roy. Meteor. Soc.*, **110**, 1121-1141.
- Lilly, D. K., 1967: The representation of small-scale turbulence in numerical simulation experiments. *Proc. I.B.M. Sci. Comput. Symp. Environ. Sci.*, Yorktown Heights, N. Y., 195-209.

- Liu, J. Y., and H. D. Orville, 1969: Numerical modelling of precipitation and cloud shadow effects on mountain induced cumuli. *J. Atmos. Sci.*, **26**, 1285-1297.
- Marshall, J. S., and W. M. Palmer, 1948: The distribution of raindrops with size. *J. Meteor.*, **5**, 165-166.
- Ogura, Y., 1963: The evolution of a moist convective element in shallow conditionally unstable atmosphere: a numerical calculation. *J. Atmos. Sci.*, **20**, 407-424.
- Reuter, G. W., and M. K. Yau, 1987: Mixing mechanisms in cumulus congestus clouds. Part II: Numerical simulations. *J. Atmos. Sci.*, **44**, 798-827.
- _____, 1987: Penetrative downdrafts in mixed-phase clouds. *S. Afr. J. Phys.*, **10**, 139-145.
- _____, 1988: Water budget and kinetic energy transformations of a mixed-phase cumulus cell: Three dimensional numerical simulation. *Beitr. Phy. Atmos.*, **61**, 30-38.
- Schlesinger, R. E., 1984: Effects of the pressure perturbation field in numerical models of uni-directionally sheared thunderstorm convection: Two versus three dimensions. *J. Atmos. Sci.*, **41**, 1571-1587.
- Smagorinsky, J., 1963: General circulation experiments with the primitive equations: Part I: The basic experiment. *Mon. Wea. Rev.*, **91**, 99-164.
- Soong, S.-T., and Y. Ogura, 1973: A comparison between axisymmetric and slab-symmetric cumulus cloud model. *J. Atmos. Sci.*, **30**, 879-893.
- Steiner, J. T., 1973: A three-dimensional model of cumulus cloud development. *J. Atmos. Sci.*, **30**, 414-435.
- _____, 1982: *An axially symmetric cloud model: Development and simulations*. Storm Weather Group Scientific Report MW-94, McGill University, Montreal, Canada, 55 pp.
- Tao, W.-K., and J. Simpson, 1993: Goddard cumulus ensemble model. Part I: Model description. *Terrestrial Atmos. Ocean Sci.*, **4**, 35-71.
- Tripoli, G. J., and W. R. Cotton, 1980: A numerical investigation of several factors leading to the observed variable intensity of deep convection over South Florida. *J. Appl. Meteor.*, **19**, 1037-1063.
- _____, and _____, 1982: The Colorado State University three-dimensional cloud / mesoscale model. Part I: General theoretical framework and sensitivity experiments. *J. Rech. Atmos.*, **16**, 185-220.

CHAPTER 5

NUMERICAL SIMULATION OF THE EFFECTS OF MESOSCALE CONVERGENCE ON CONVECTIVE RAIN SHOWERS

Remark: This chapter has been accepted for publication, and will appear in the *Monthly Weather Review*.

5.1 Introduction

There is abounding evidence from observations that low-level mesoscale convergence tends to trigger and enhance cumulus convection. A major finding of the Thunderstorm Project was that airmass thunderstorms are often preceded by convergence of surface winds (on the scale of 10-100 km) up to 30 min before the detection of the first radar echo (Byers and Braham 1949). Close correlation between areas of convergence and convective cloud formation was found for the central United States (Lewis 1971, Hudson 1971). Wilson and Schreiber (1986) reported that in northeast Colorado about 80% of precipitating convective cells with radar reflectivity values greater than 30 dBZ occurred in close proximity to convergence boundaries identified by radar. Sea-breeze fronts, thunderstorm outflow boundaries, and drylines often define a narrow zone of strong low-level convergence that acts as forcing for subsequent convective development (Purdum 1976, Cooper et al. 1982). Comparing locations of surface wind convergence with convective precipitation, Achtemeier (1983) concluded that the forcing for storm development is often rooted close to the surface. Studies were undertaken for Florida rainstorms to determine the time lag between surface convergence and the initiation of rain on the ground. Ulanski and Garstang (1978) found that patches of convergence appear from 20 to 90 min before the onset of rain. The average time lag between the beginning of

convergence and the initiation of rain was 35 min, while the average time between the beginning of convergence and the peak rainfall was 86 min (Watson and Blanchard 1984). Observations suggest that persistent low-level mesoscale convergence is generally necessary to generate ensembles of deep convective clouds in the tropics (Ogura et al. 1979).

The effects of meso- β convergence on cumulus convection have also been examined using numerical cloud models. Using a time-dependent slab-symmetric model, Chang and Orville (1973) showed that the addition of persistent boundary-layer convergence in the model leads to a broader and more intense cumulus than the model cloud without convergence. Using a more sophisticated approach of including the convergence profile, Chen and Orville (1980) found that the convection is more intense when there is low-level convergence, while it is suppressed when there is divergence. The persistent presence of strong low-level convergence can increase the surface rainfall by 40% for midlatitude conditions (Crook and Moncrieff 1988). More vigorous storms with greater precipitation intensities occurred when low-level convergence was present in three-dimensional simulations (Tripoli and Cotton 1980). Slab-symmetric simulations of tropical rainbands showed that long-lasting deep convection was supported by mesoscale lifting (Soong and Ogura 1980, Tao and Simpson 1989).

There are some major shortcomings in previous modelling studies relating convergence with convective rainfall. First, mesoscale convergence imposed on the model flow was kept fixed, specified from a priori conditions of large-scale observations. In nature, however, the cloud convection will feed back (positively and negatively) into the convergent forcing. This interactive two-way feedback between small-scale and large-scale circulations is probably most important for long-lasting organized convection such as persistent rainbands, squall-lines or supercells. The present study does not improve on this aspect.

A second shortcoming of previous modelling studies is that, they used the assumption of slab-symmetry, except for the simulations by Tripoli and Cotton (1980) and Dudhia and Moncrieff (1987) which were based on three-dimensional model geometry. It

is well known that by restricting the flow to a vertical plane, the model imposes some unrealistic artifacts to the convective cloud circulations. To clarify what is involved we consider the case of a convective cell consisting of a cumulus updraft and compensating downward motion in the outer rim. Suppose at a given horizontal section the updraft area can be approximated by a circle with a radius a , and the downdraft area by an annulus with outer radius b . Mass continuity dictates that the upward and downward mass fluxes are balanced:

$$\begin{aligned} \pi a^2 \rho w^{\uparrow} &= \pi (b^2 - a^2) \rho w^{\downarrow} \\ \Rightarrow \frac{w^{\uparrow}}{w^{\downarrow}} &= \frac{b^2 - a^2}{a^2} \end{aligned} \quad (5.1)$$

where ρ is the air density, w^{\uparrow} the mean updraft speed, and w^{\downarrow} the mean downdraft speed, respectively. In the framework of slab-symmetry, however, the mass flux balance becomes

$$\begin{aligned} a L \rho w^{\uparrow} &= (b - a) L \rho w^{\downarrow} \\ \Rightarrow \frac{w^{\uparrow}}{w^{\downarrow}} &= \frac{(b - a)}{a} \end{aligned} \quad (5.2)$$

where L is the length of the slab considered. Obviously, (5.1) and (5.2) are not compatible as the 3D relation (5.1) is quadratic whereas the 2D relation (5.2) is linear. The slab-symmetric simulation can be "tuned" to simulate realistically the magnitudes of mean cumulus updraft and downdraft, or the area of updraft and downdraft. However, it is impossible to make a slab-symmetric simulation that provides realistic estimates for both magnitudes and the areas of the updraft and downdraft, respectively (Soong and Ogura 1973). Related to this geometric defect, the deviations from the hydrostatic pressure are overestimated in slab-symmetric models causing unrealistic perturbation pressure effects (Schlesinger 1984). Based on these considerations, it is likely that the slab-symmetric assumption tends to overestimate the role of mesoscale convergence, at least for rapidly

developing cumulus cells with strong updrafts. With the axisymmetric model used in this study, however, the main shortcoming of the slab-symmetric assumption is avoided as the axisymmetric mass balance is consistent with the three-dimensional version (5.1). It should be pointed out that the axisymmetric cloud model is not suited for simulating a convective cloud line. Convective cloud bands, however, can often be simulated quite well with slab-symmetric models; so both axisymmetric and slab-symmetric geometries have their advantages depending on the structures of cloud systems.

A third shortcoming of previous modelling studies was that they focused mainly on indicating major differences in model runs with and without strong convergence rather than quantifying the contribution of convergence toward surface rainfall.

To our knowledge no serious attempts were reported in the literature to quantify the relation between convective rainfall and the mesoscale convergence profile. The objective of this chapter is to quantify how cloud development and convective rainfall are affected by the magnitude and the depth of convergence, when the ambient flow exhibits no vertical shear. A time-dependent non-hydrostatic cumulus model will be used in the axisymmetric geometry in which the equations are formulated in cylindrical polar coordinates and all azimuthal gradients are set to zero. Axisymmetric models (often called 2.5 dimensional models) require far less computing resource than fully three-dimensional models, yet at the same time, they overcome the key limitation of the slab-symmetric assumption that unrealistically constrains the convective circulation in that the magnitudes and areas of mean updrafts and downdrafts cannot be reproduced realistically (see discussion above).

We recognize that axisymmetric models have shortcomings of their own. For example, they cannot accommodate vertical wind shear and cloud-cloud interactions. In this study, however, these are not major issues as the axisymmetric model will be used to simulate a single convective cell developing in an environment that has zero vertical shear in its horizontally averaged flow field.

This chapter is organized into five sections. The cloud model is briefly reviewed in section 5.2. In section 5.3, the environmental conditions, the control case simulation, and

its verification against radar observations are described. Section 5.4 presents sensitivity experiments to quantify the effects of magnitude and depth of the convergent layer on cloud development, the intensity of precipitation, and the time needed for the onset of surface rainfall. The relative contribution of convergence magnitude versus convergence depth is also dealt with. Finally, the results are summarized and interpreted in section 5.5.

5.2 Numerical Cloud Model

5.2.1 General characteristics

The tool used in this study is the axisymmetric version of a cumulus cloud model with large-scale convergent forcing. As the model assumptions, equations and numerical techniques were presented in Steiner (1982), Reuter and Yau (1987), Reuter (1987), Guan and Reuter (1995), only the main features of the model are briefly summarized here. The deep anelastic continuity equation is used to filter out acoustic waves by neglecting the local variation of air density with time:

$$\frac{1}{r} \frac{\partial(ur)}{\partial r} + \frac{1}{\rho_0} \frac{\partial(\rho_0 w)}{\partial z} = 0. \quad (5.3)$$

Here r and z denote the radial and vertical coordinates; u and w are the radial and vertical velocity components, respectively. The basic state air density, i.e., the density of the hydrostatically balanced horizontally-averaged flow, is denoted by $\rho_0 = \rho_0(z)$ and depends on height only. Conservation of radial and vertical momentum results in prognostic partial differential equations for u and w , respectively. By combining the equations of motion in flux form with (5.3), a diagnostic (Poisson) partial differential equation for the perturbation pressure is obtained. The effects of friction at the earth's surface are neglected. Sub-grid scale turbulent processes are modeled using a first-order closure scheme where the Reynold stresses are assumed to be proportional to the velocity deformation. The eddy exchange coefficient depends on the local moist buoyancy and shear deformation time scales. The local Prandtl number for turbulent diffusion is assumed

unity implying that the eddy exchange coefficient for scalar quantities has the same value as that for momentum.

More prognostic partial differential equations are obtained from the conservation of total specific moist entropy and the water substance in vapor and liquid form. The cloud microphysics uses a Kessler-type bulk water parameterization scheme consisting of cloud water and rainwater. Cloud water follows air motion passively and evaporates instantaneously in subsaturated air, whereas the advection of rainwater is affected by a mass-weighted terminal fall speed and the evaporation which depends on the size of precipitation particles. The size distribution of raindrops is taken to be the Marshall-Palmer inverse exponential. The expressions for the mass-weighted terminal fall speed of rain, the evaporation rate of rain and the rate of conversion of cloud to rain were given in Chapter 4. The threshold value for the auto-conversion of cloud to rain was set at 1 g kg^{-1} .

Omitting ice phase microphysical processes in the model simulations requires some justification. Previous studies indicated that including ice microphysics is important for simulating precipitation in squall lines with extensive stratiform rain falling from its broad rear anvil (e.g., Tao and Simpson 1993, Caniaux et al. 1994). Ice processes are also desirable when simulating tall tropical storms that develop in a neutrally stratified environment (e.g., Bennets and Rawlins 1981). However, ice microphysics has little effects on the precipitation and dynamics of clouds developing in strongly convective-unstable conditions with little vertical shear (Tripoli and Cotton 1982, Koenig and Murray 1984, Reuter 1987, 1988). Based on the selection of the thermodynamic sounding and the absence of ambient shear, we expect that our model results would not change significantly if an ice phase microphysics parameterization were adopted.

5.2.2 *Mesoscale convergence and initialization*

Several different methods of incorporating large-scale convergence in cloud-scale models have been described in the literature (Chang and Orville 1973, Soong and Tao 1980, Chen and Orville 1980, Tripoli and Cotton 1980). In this study the approach was to implement a one-way open lateral boundary condition with a prescribed vertical profile of

radial inflow at the lateral boundary $r = R$:

$$u(r=R, z) = \frac{-R}{2\rho_o} \frac{\partial(\rho_o w)}{\partial z} \Big|_{(r=R, z)} = \frac{R}{2} CONV(z) \quad (5.4)$$

where $CONV(z)$ denotes a height-dependent convergence profile. Care was given to assume that there is no net influx of mass when integrating over the entire model domain, that is, the air entering in lower layers must exit the domain at some higher levels.

$$\begin{aligned} \int_{z=0}^{z=H} \rho_o(z) u(r=R, z) dz &= \frac{R}{2} \int_{z=0}^{z=H} \frac{\partial(\rho_o w)}{\partial z} \Big|_{(r=R, z)} dz \\ &= \frac{R}{2} \int_{z=0}^{z=H} \rho_o(z) CONV(z) dz = 0. \end{aligned} \quad (5.5)$$

In this study, the radial inflow was determined from the low-level mesoscale convergence estimates, derived from the Doppler radar velocity data using the Volume Velocity Processing (VVP) technique (Waldteufel and Corbin 1979, Koscielny et al. 1982). For the upper portion of the troposphere, where mesoscale convergence estimates were not available, a constant radial outflow was determined using the constraint of zero accumulation of mass in the model domain.

The top and bottom boundaries of the model are assumed to be flat, rigid and smooth. The very stable thermal stratification, combined with dissipation, near the tropopause assures that the reflection of gravity waves is minimal at the model top boundary. In the model, there is no transport of heat, vapor and cloud water through the top and bottom boundaries. However, rainwater is allowed to leave the domain at the bottom. The mesoscale convergence has also implications for initialization of the model simulations. At the initial time, the radial wind components vary horizontally to satisfy locally the balance of mass. The deep moist anelastic continuity equation (5.3) is used to relate the vertical velocity and radial wind component. The vertical velocity is horizontally uniform given by the mesoscale lifting derived from integrating the mesoscale convergence

profile $CONV(z)$:

$$u(r, z, t=0) = \frac{1}{r} \int_0^r r CONV(z) dr = \frac{1}{2} r CONV(z)$$

$$w(r, z, t=0) = \frac{1}{\rho_o(z)} \int_0^z \rho_o(z) CONV(z) dz \quad . \quad (5.6)$$

Owing to the large-scale lifting, there was no need for initiating the convection with a temperature or humidity anomaly at low levels (i.e., the "bubble" method). Instead initial temperature and humidity values were horizontally uniform for each level, based on the observed sounding profile. The major disadvantage of using the "bubble" method is that the simulated cloud is rather sensitive to the spatial dimensions of the initial perturbation (e.g., Reuter and Yau 1987). This is not the case when using horizontally uniform conditions with radially uniform lifting since here convection begins from local perturbation which develops from numerical truncation inaccuracies. In fact, if the numerical scheme would be perfect (i.e., without truncation inaccuracies), the flow pattern would remain horizontally uniform throughout the simulation period. Since in nature there is usually some horizontal nonuniformity, we might anticipate that the model simulations with horizontal uniformity might lag nature in spawning convective overturning.

5.2.3 Numerical aspects

The partial differential equations are solved numerically using a finite-difference scheme on a staggered grid. To integrate in time, the second-order non-diffusive leapfrog method is used with the subgrid scale eddy exchange processes lagged in time (Steiner 1982). A time-filtering procedure is invoked to prevent splitting of solutions at odd and even time steps. An energy-conserving centered difference method is used in space.

All numerical experiments presented here had the same numerical grid arrangement. The computational domain had a diameter of 40 km and a depth of 12 km. The spatial resolution was uniform, set at 200 m in both the radial and vertical directions.

The time step was 3 seconds. Some numerical experiments were run with a larger domain and with finer grid resolution. The similarity of the model outputs indicates that the model findings presented here are not sensitive to the specific numerical grid arrangement.

5.3 Simulation of Control Case

5.3.1 Environmental conditions

Since the realistic simulation of convective precipitation is considered a prerequisite for a detailed study of the convergence effects on convective rainfall, the environmental conditions of a particular observed case were adopted to verify model results with observations. No attempt was made to model the development of severe convection because the axisymmetric model with warm rain microphysics cannot simulate the formation of graupel and hail, cloud-cloud interactions, and the effects of vertical shear. Instead a case was selected where a moderate-sized cumulonimbus formed in calm conditions from 0600 to 0930 UTC on 19 August 1992, in the northwest quadrant between 40 and 90 km from the Carvel radar site (53°34' N, 114°09' W). Figure 5.1 shows the sounding sampled at Stony Plain (53°33' N, 114°06' W, 766 m ASL) at 1200 UTC. This sounding, taken at 30 km from the observed cell, should be representative for actual convective environment. The temperature lapse rate was close to dry adiabatic from the surface to about 850 mb. However, the vapor mixing ratio was not well-mixed in the boundary layer. With surface conditions, the lifting condensation level was estimated at 820 mb. The airmass was convectively unstable (Figure 5.2) with a Convective Available Potential Energy of about 610 J kg^{-1} for surface air. The level of free convection was about 785 mb. Thus if the air originating from near the surface were lifted up to 785 mb (1.5 km), the CAPE could be released to fuel convection. The existence of mesoscale convergence did provide the necessary forcing for lifting, and cloud convection did occur (see the following radar data analysis).

Information about the low-level convergence field in the area of interest could be estimated by applying the Volume Velocity Processing (VVP) technique to the Doppler

velocity data in this area, sampled at two low elevation angles. A detailed discussion of the VVP procedures used to retrieve the convergence values is given in Chapter 3. The finding from the Doppler velocity data analysis, essential for the area of interest, is that the lowest 700 m of the atmosphere had a peak convergence value of about 10^{-3} s^{-1} . The convergence preceded the enhancement of rainfall by nearly 30 min, and covered an area about $40 \text{ km} \times 40 \text{ km}$. Averaging the convergence values over this area, provides a mean convergence value of $2.1 \times 10^{-4} \text{ s}^{-1}$. Based on these observations, we deduced the following profile of mesoscale convergence ($CONV(z)$) used for the control case simulation:

$$CONV(z) = \begin{cases} -2.10 \times 10^{-4} \text{ s}^{-1} & 0 \leq z \leq 0.7 \text{ km} \\ 0 & 0.7 < z \leq 2.5 \text{ km} \\ 2.45 \times 10^{-5} \text{ s}^{-1} & 2.5 < z \leq 8.5 \text{ km} \\ 0 & 8.5 < z \leq 12 \text{ km} . \end{cases} \quad (5.7)$$

With this convergence profile, a significant inflow of 2.1 ms^{-1} enters the domain from the lateral boundary over the lowest 0.7 km while a weak outflow of 0.39 ms^{-1} exists between 2.7 and 8.5 km. The wind field can alternatively be shown using stream function, ψ , which is defined by:

$$\rho_o u = -\frac{\partial \psi}{\partial z} \quad , \quad \rho_o w = \frac{1}{r} \frac{\partial (r\psi)}{\partial r} \quad (5.8)$$

according to the deep moist anelastic continuity equation (5.3). The stream function was computed by the integration of (5.8), assuming $\psi(0,0) = 0$. Figure 5.2 shows the vertical section of the initial wind field used in the control case simulation. The vertical velocity is 0.13 ms^{-1} at 1.1 km (the LCL level), increasing to 0.15 ms^{-1} at 2.5 km as density is reduced with height and then decreasing to zero at 7.5 km.

5.3.2 Evolution of cloud and precipitation

Model cloud dynamics can be traced conveniently in terms of peak vertical updraft

(w_{max}) and domain-integrated kinetic energy (KE), which is given by

$$KE = \frac{1}{V} \int_V \frac{1}{2} \rho_o (u^2 + w^2) dV \quad (5.9)$$

where V denotes the volume of the model domain. Here w_{max} and KE are local and global parameters of the flow field, respectively. In the first hour w_{max} oscillates and develops a local maximum of about 5 ms^{-1} at 1.5 h (Figure 5.3). The time evolution of the total kinetic energy indicates that about 1.5 h of model time were required to "fire up" the convection. The slow "warm-up" process for generating convection by mesoscale lifting agrees with the finding of Lipps and Hemler (1986), and is associated with the need for eroding the negative CAPE and the relatively dry air below 800 mb. For this particular case, about 10 J of external work are required to lift 1 kg of air from the surface to its level of free convection. After the "warm-up" process, the total kinetic energy increases rapidly to reach a maximum of 8 TJ ($= 8 \times 10^{12} \text{ J}$) at about 2 h. After reaching a secondary maximum at about 4 h, both w_{max} and KE decrease to a quasi-equilibrium level of about 6.5 ms^{-1} and about 5.5 TJ.

Figure 5.4 shows (truncated) vertical cross-sections at 80, 100, 140, and 180 min depicting velocity stream function (ψ), equivalent potential temperature (θ_e), cloud water mixing ratio (q_c), and radar reflectivity (dBZ). The radar reflectivity values were calculated from rain water content values using Geotis' (1971) expression. At 80 min the flow is still dominated by the mesoscale pattern characterized by radial inflow through the lateral boundary in low levels, and radial outflow aloft. The boundary lifting causes saturation resulting in a flat cloud base located at about 900 m above the ground. The cloud top is also flat near the height of 6 km. The vertical velocity is weak, peaking at about 1.4 ms^{-1} in the boundary layer. Widespread stratiform rain is present as indicated by the layer of radar reflectivity echoes near the surface. Equivalent potential temperature values decrease from about 323 K near the surface to a minimum of about 320 K at height 7.4 km, indicating that at 80 min the environment is susceptible to convective overturning.

After 80 min, cloud development intensifies forming a large convective cell with a

diameter of about 15 km (Figure 5.4b). Intense surface rainfall exceeding 40 dBZ occurs near the domain center. The boundary layer air becomes cooler due to evaporation of rain falling below the cloud and due to mesoscale lifting as well. At 140 min (Figure 5.4c) the convection has strengthened and the cloud top has penetrated above 7 km. The strong updraft, around 5 ms^{-1} , yields a 'donut' shape in the radar reflectivity field near the cloud top. The cloud water field suggests that the outward slanted circulation is due to a buildup of water loading near the cloud top at the central axis. The loading of cloud water and rainwater causes weak downward acceleration, pushing the rising air radially outward. The 20 dBZ contour (approximating the rainfall rate of 1 mmh^{-1}) reaches its highest altitude of 7 km. At 140 min the development of secondary convection becomes apparent at a radius of about 14 km, which is responsible for the formation of the intense precipitation echoes (larger than 37 dBZ) shown at 180 min (Figure 5.4d). At 180 min an updraft is found at a height of about 6 km at the central axis. Beneath this updraft, however, there is descending motion extending from about $z = 3 \text{ km}$ to the surface. The cloud water field shows that this downdraft has partially eroded the lower portion of the cloud. The equivalent potential temperature field shows most of the air between heights of 2 km and 7 km have approximately the same θ_e value of 321 K. Thus, this layer is at its state of neutrality with respect to moist convection. After 180 min (not shown), the convection and precipitation start to dissipate, gradually reaching a quasi-steady state with the motion driven by the mesoscale convergent forcing in the absence of convective instability.

5.3.3 *Comparison with radar observations*

The control run simulation will be compared with radar observations to assess whether the model can realistically simulate nature under the assumed conditions. A problem inherently involved in comparing convective rainfall is in the natural variability of convection, caused by the temporal and spatial variability of small-scale temperature values, sub-cloud moisture supply, and interaction of turbulent eddies. It is thus not expected that this (or any other) model can reproduce the observed radar reflectivity

structure in all its details. To allow for meaningful intercomparison, we have to choose the model time when the simulated convection is at the same stage of its development as the observed one. Since the cloud model starts the convection from totally cloud-free conditions, it needs an artificial "warm-up" period before the convective instability can be released. Figure 5.3 suggests that this warm-up period for the control case is about 100 min. In addition, the model radar reflectivity values represent average values for rings of depth 200 m and width 200 m, whereas the radar measurements represent bins with length 0.5 km and elevation angle and azimuthal beam widths of about 1°. There is also mismatch in temporal resolutions of model and observations: 3 seconds in model versus 10 min in recorded radar observations.

Bearing in mind these limitations, a comparison was made of the area-averaged rainfall rate near the ground. The radar reflectivity values from the lowest elevation angle (0.5°) were averaged over the convergence region of 40 km × 40 km, and converted to rainfall rate values using the Z-R relationship: $Z=295 R^{1.43}$. The modelled rainfall rates were calculated from the flux of rain water at the ground averaged over the circular base having a diameter of 40 km. The rainfall curves (shown in Figure 5.5) are similar, differing by less than 1.5 mmh⁻¹ from 100- to 220- min model times. The model showed both the primary and secondary precipitation peaks separated by about one hour. After 220 min the good agreement ceases, presumably related to the fact that in nature the strong boundary-layer convergence was not maintained for more than three hours as the model used.

The model is also compared with observations in terms of peak reflectivity values (Table 5.1). The agreement in dBZ_{max} is fairly close, differing by 1.8 dBZ on average. As the wind field and thermodynamic structure were not observed, the model structure cannot be validated. Therefore, the good comparison between observed and simulated results in rainfall intensity and maximum radar reflectivity should not be overstated.

Table 5.1 Comparison of modelled peak radar reflectivity values (dBZ_{max}) from the control run with the Carvel radar observations between 0630 and 0820 UTC on 19 August 1992.

Time (min)	Model	Observations
100	43.5	45.3
110	41.3	44.0
120	43.9	46.0
130	44.0	45.7
140	44.1	43.8
150	45.1	43.4
170	42.7	43.8
180	40.0	44.9
200	43.2	42.6
210	40.0	40.7

5.4 Results of Sensitivity Experiments

5.4.1 Specifications of experiments

All numerical experiments here have the same structure in their mesoscale convergence profile shown in Figure 5.6. It has an exact balance of low-level convergence and upper-level divergence:

$$\bar{\rho}_{DIV} M_{DIV} Z_{DIV} = - \bar{\rho}_{CON} M_{CON} Z_{CON} . \quad (5.10)$$

The convergence with a magnitude M_{CON} is spread over the depth of Z_{CON} from the surface, while the divergence (of magnitude M_{DIV}) extends over a depth of Z_{DIV} (from Z_{DIV} to Z_{DT}). In (5.10), $\bar{\rho}_{CON}$ and $\bar{\rho}_{DIV}$ are the mean air densities (vertically) averaged over the layers with convergence and divergence, respectively. From the deep anelastic continuity equation (5.3), the mesoscale updraft at Z_{CON} is given by:

$$w(Z_{CON}) = \frac{1}{\rho(Z_{CON})} \int_0^{Z_{CON}} \rho(z) M_{CON} dz = \frac{\bar{\rho}_{CON}}{\rho(Z_{CON})} M_{CON} Z_{CON} \quad (5.11)$$

where the density-weighted convergence is integrated over the depth of Z_{CON} .

Three sets of sensitivity experiments were made to examine the effects of the magnitude of convergence (experiments M1-M10), the depth of convergence layer (experiments D1-D8), and the relative importance of magnitude versus depth (C1-C8). The selected parameters for these experiments are listed in Table 5.2. For experiments M1 to M10 the depths of the convergence and the divergence layers are taken as the values of the control run discussed in the previous section, that is, $Z_{CON} = 0.7$ km and $Z_{DIV} = 6.0$ km. For other experiments, the vertical spacings are modified to provide meaningful results.

5.4.2 *Effects of the magnitude of boundary-layer convergence*

Figure 5.7 compares the evolution of experiments M1-M10 in terms of the instantaneous rainfall rate (in mmh^{-1}) and the accumulated rainfall (in mm) averaged over the circular model base area. The curves show that as the magnitude of the convergence (M_{CON}) increases, so does the accumulated rain. Furthermore, the increase in M_{CON} brings about a progressively earlier onset of surface rainfall. The instantaneous rainfall rate also increases monotonically with increasing M_{CON} during the initial development of the convective cell. Then for a strongly convective intermediate stage, rainfall rate and the M_{CON} are more poorly correlated. Once the strongly convective activity subsides, the original strong correlation between the two parameters is re-established.

In theory, if rainfall were entirely due to the mesoscale vertical motion forced by the boundary-layer convergence (i.e., without convective drafts), the rainfall rate should be directly proportional to the mesoscale upward vapor flux, which is proportional to the mesoscale updraft for a constant vapor content (i.e., constant product of air density times vapor mixing ratio). The theory predicting a linear relationship between rainfall rate and ascending motion is based on the assumption of steady-state balance of upward vapor flux and downward flux of rain water (e.g., McIlveen 1986). Alternatively, this proportionality relationship could also be derived by assuming an instantaneous conversion of condensed cloud water into precipitation, because the condensation rate is proportional to the updraft

Table 5.2 Specification of sensitivity experiments. Also listed are the time needed for rainfall larger than 1 mm (T_{1mm}).

<i>Experiments</i>	M_{CON} ($10^{-4} s^{-1}$)	Z_{CON} (km)	Z_{DIV} (km)	T_{1mm} (min)
M1	0.25	0.7	6.0	> 300
M2	0.50	0.7	6.0	267
M3	0.75	0.7	6.0	207
M4	1.00	0.7	6.0	169
M5	1.25	0.7	6.0	143
M6	1.50	0.7	6.0	125
M7	1.75	0.7	6.0	111
M8	2.00	0.7	6.0	100
M9	2.25	0.7	6.0	93
M10	2.50	0.7	6.0	87
D1	1.0	0.5	4.0	184
D2	1.0	1.0	4.0	113
D3	1.0	1.5	4.0	89
D4	1.0	2.0	4.0	75
D5	1.0	2.5	4.0	70
D6	1.0	3.0	4.0	64
D7	1.0	3.5	4.0	59
D8	1.0	4.0	4.0	57
C1	0.54	4.0	4.0	90.1
C2	0.61	3.5	4.0	87.1
C3	0.69	3.0	4.0	84.0
C4	0.81	2.5	4.0	80.9
C5	0.99	2.0	4.0	75.8
C6	1.29	1.5	4.0	73.8
C7	1.89	1.0	4.0	71.7
C8	3.72	0.5	4.0	71.2

speed (Rogers and Yau 1987). From (5.11) it follows for a constant convergence depth

(Z_{CON}); the mesoscale upward vapor flux is proportional to the magnitude of the convergence M_{CON} .

Figure 5.7 shows that in the presence of convection, the linear relationship between rainfall and mesoscale convergence magnitude comes close, but is not entirely appropriate. For example, doubling the convergence magnitude from 1.0×10^{-4} to $2.0 \times 10^{-4} \text{ s}^{-1}$ increases the 5-h accumulated rainfall by a factor of 2.6, whereas doubling the convergence from 1.25×10^{-4} to $2.5 \times 10^{-4} \text{ s}^{-1}$ increases the rainfall by a factor of 2.3. The convective rainfall increases monotonically with increasing convergence, but does not follow the exact linear relationship as suggested by theory for steady precipitation. The nonlinearity also shows up when plotting the start time of the surface rainfall versus the convergence magnitude (Figure 5.8). Increasing the convergence speeds up the formation of rain. It takes 300 min in the weakest convergence case (M1) to accumulate 0.1 mm rainfall at the surface, but only 75 min in the strongest convergence case (M10). Intermediate convergence values yield time lapses between these two extremes. In fact, the data points could be fitted by hyperbolas.

The nonlinear interaction of mesoscale and cumulus dynamics is also apparent in Figure 5.9, which shows the time evolution of total kinetic energy (KE) for selected experiments. To maintain clarity in the graph, only the curves for five experiments are plotted here. Once again, the increasing convergence reduces the time required to initiate the convection. In the first hour the kinetic energy depends linearly on the convergence magnitude since the ascent is solely driven by the mesoscale lifting due to the convergence in the lowest 0.7 km. It takes about 60 min for M9 to enter the rapid development of the KE (indicative for the onset of convection), but about 240 min for M1 to reach the same stage as M9. We analyzed the soundings of temperature and dewpoint for each of the cases at the time instant just prior to the rapid increase of the KE . Figure 5.10 shows the sounding for experiment M5 at 96.3 min. The soundings for the other cases are almost identical to the one shown. As all cases exhibit the same thermodynamic structure, the mesoscale updraft apparently has caused the same amount of lifting in each case. At this stage it should be pointed out that in nature it is rather unlikely to yield such a deep

saturated, yet marginally unstable sounding due to the presence of horizontal nonuniformity that would tend to cause local convective overturning. The model thermodynamic fields, on the other hand, are horizontally uniform, with only small perturbation driven by the numerical approximations. After the model convection is initiated, stronger convergence magnitude leads to a more intense circulation. The kinetic energy starts to oscillate after reaching its maximum. Interestingly, the weakest convergence case, M1, follows a growth cycle that differs markedly from the others. After a 3-h "brewing" period, the convection develops strongly, and its KE values are even larger than those in both M3 and M5. It is speculated this spurt of late development is a manifestation of a reservoir effect (Lee et al. 1991), created by the persistent convergence forcing that allows more moisture to be advected into the central region than in the cases where the convective overturning depletes the moisture earlier.

5.4.3 *Effects of the depth of boundary-layer convergence*

Experiments D1-D8 (with convergence parameters defined in Table 5.2) were designed to quantify changes in the depth of the convergence layer (Z_{CON}), while keeping the convergence magnitude (M_{CON}) constant. Eq. (5.11) shows that the mesoscale updraft at Z_{CON} becomes stronger when Z_{CON} is increased. Thus increasing the depth of the convergence layer, while keeping M_{CON} constant, results in more mass and moisture convergence into the vertical column. Figure 5.11 compares the evolution of accumulated rain and rainfall rate (averaged over the domain base) for simulations D1 to D8. Consistent with findings reported for marine tropical conditions (Frank 1978, Song and Frank 1983), the modelled results show that more rain reaches the ground as the convergence layer becomes progressively deeper. The accumulated rain increases monotonically, yet nonlinearly with the increase of Z_{CON} . When Z_{CON} is increased from 2.5 to 3.0 km the rainfall increases noticeably, whereas the enhancement of rain is small when Z_{CON} is increased from 3.0 to 3.5 km. Doubling the convergence depth from 0.5 to 1.0 km increases the rainfall by a factor of about 2.7. Nevertheless, doubling Z_{CON} from 2.0 to 4.0 km causes the rainfall to increase only by a factor of about 1.5. This decrease in rain

enhancement is largely related to the change of vapor mixing ratio which becomes less at higher altitude (see Figure 5.1). The air between 785 and 710 mb (corresponding to the altitudes of 1.5 and 2.0 km above the ground) is moist and has a conditionally unstable temperature lapse rate. Therefore, increasing the convergence depth from 1.5 to 2.0 km causes a substantial increase in the 5-h accumulated rain. On the other hand, since the air above 650 mb contains smaller amounts of vapor mixing ratio, the 5-h rainfall is only increased by about 2 mm from D6 to D7.

The evolution of the area-averaged rainfall rates (Figure 5.11b) indicates that after the rapid initial growth, there comes a short period of weakening in rainfall rates. A new spurt of rain development occurs, followed by a gradual levelling off with some irregular oscillations. Deeper convergent layers not only stimulate the rainfall amounts, but also reduce the time required for the rain to reach the ground. Table 5.2 shows the comparison of the time T_{1mm} for simulations D1-D8, at which the area-averaged rain accumulation exceeds 1 mm. The dependence of T_{1mm} on Z_{CON} is not strictly linear. Increasing Z_{CON} from 0.5 to 1.0 km reduces T_{1mm} from 184 to 113 min, while a further increase in Z_{CON} to 2.0 km shortens T_{1mm} to 75 min.

5.4.4 *Relative contributions of the convergence magnitude versus its depth*

The sensitivity experiments described in the previous two subsections have shown that the accumulated rain increases if either the convergence magnitude, M_{CON} , or the depth of the convergent layer, Z_{CON} , is increased. However, the relative contribution of these two parameters to convection is still not clear and will be discussed in this subsection. From (5.11) it follows that the vertical mass flux at the top of convergence layers depends on the product of three factors: M_{CON} , Z_{CON} , and the air density averaged over the convergence layer. For moisture fluxes, the relative vertical spacing between the altitude of the peak mesoscale updraft and the cloud base level is also important as the vapor mixing ratio changes with height. Numerical experiments C1 to C8 were made with Z_{CON} values set from 0.5 to 4.0 km at an even increasing interval of 0.5 km. As Z_{CON} is increased, the corresponding M_{CON} value is decreased accordingly such that the vertical

mass flux given by $\rho(Z_{CON}) \cdot w(Z_{CON})$ at the altitude Z_{CON} is kept constant at $0.2 \text{ kg m}^{-2} \text{ s}^{-1}$. The specification of the eight experiments is given in Table 5.2. Figure 5.12a compares the evolution of the total kinetic energy for the eight experiments. Initially, KE is determined by the model initialization. However, after about 50 min, convection develops in all eight cases. The first peak in KE shows up at around 65 min. The highest KE is found in C8, which has the strongest convergence magnitude and the smallest Z_{CON} . To examine more closely the convection development, the time evolution of the vertical moisture flux at the cloud base level for the eight experiments was also computed. The results are shown in Figure 5.12b. Before the onset of the convection (i.e., before 50 min), the moisture flux increases as the convergence depth decreases. The reduction in moisture flux is caused by the stratification of water vapor, which drops off sharply with height. Thus, as the convergence layer becomes deeper, the effective water vapor mixing ratio decreases, thereby lowering the moisture flux through cloud base. From 50 to 80 min, the depth of convergence layers becomes even more significant as evidenced by the rapid increase in moisture flux. In fact, experiments C1-C8 show that almost the same amounts of moisture flux feed vapor through the cloud base. There is some correlation between the evolution of the vapor flux $\rho q_v w$ at the cloud base and that of the total kinetic energy KE .

After 100 min, the convection in all experiments enters the second rapid development period. Compared with the first growing stage, the convection in the eight cases exhibits more complicated behavior under the combined effects of convergence magnitude and its depth. The largest peak value in KE is found in C6, which also has the largest vapor flux at cloud base. The combination of the convergence magnitude and the convergence depth in C6 apparently provides the most favorable conditions for reaching the highest peak value of KE . Closer examination shows that C6 has higher θ_e air feeding into the cloud than the other cases during its peak activity.

It is interesting to examine the evolution of the moisture flux for experiment C8, the run with the shallowest convergence layer. After the first convective burst, the moisture flux decreases sharply and almost reaches zero. The associated flow field reveals that cumulus downdraft outflow fills almost the entire portion of the sub-cloud air. At this

stage, the flow field shows little resemblance to the initial mesoscale convergence field despite the fact that the low-level inflow through the model lateral boundary has been maintained. For the other runs, the downdraft outflow is less pronounced because the convergence is spread out over a much deeper layer and thereby reduces its impact.

The precipitation for the experiments C1-C8 are compared in Figure 5.12c, where area-averaged rainfall accumulation is plotted versus time. Increasing the convergence magnitude (while reducing its depth accordingly) tends to increase the accumulated rainfall. The reason for this increase in precipitation is related to the increase in (time-averaged) water vapor flux through the cloud base when the convergence layer becomes shallower and more humid. As the average vapor content of the convergent layer becomes progressively larger (when we change from C1 to C8), it increases the equivalent potential temperature of the convergent air and thus provides more buoyancy for convection and rainfall. The 5-h accumulated rainfall amounts increase by about 29% from C1 to C5 and by about 9.5% from C5 to C7 when the convergence magnitude is nearly doubled but the convergence depth is halved. The trend of rain increase is even smaller from C7 to C8 (8.6%). Comparing the times $T_{1\text{mm}}$, at which 1-mm rainfall is accumulated, for the eight experiments (Table 5.2), we find that $T_{1\text{mm}}$ becomes smaller when Z_{CON} is decreased, that is, when the moisture flux is strengthened.

5.5 Summary and Conclusions

A systematic study was presented to determine the role of the convergence magnitude and the convergence depth in the development of cloud convection and convective rainfall. Focusing on a case where the environmental wind shear was weak, a time-dependent axisymmetric cloud model was used to allow us to make many sensitivity experiments with limited computing resources. The lateral boundary condition of the model was modified to allow a prescribed profile of radial inflow advecting heat and moisture into the domain. The model convection was initiated by convergent forcing without any thermal or moisture perturbation. The convergence magnitude and depth for

the control run were adopted from the VVP analysis of single-Doppler radar velocity data. Good agreements were found between model results and radar observations in terms of the evolution of area-averaged rainfall rates and peak radar reflectivity factors.

Sensitivity experiments were designed to quantify how the convergence magnitude and depth affect the cloud circulation and convective rainfall. The results show that the convection is intensified with more rainfall when either the magnitude or the depth of convergent layers is increased. In both conditions, the accumulated rainfall increases monotonically, but not in the strictly linear fashion as suggested by theory based on steady-state balance. Increasing the convergence not only produces more rain, but it also accelerates the onset of rainfall reaching the ground. The lag time from the beginning of convergence to the beginning of surface rainfall varies between 1 and 2 hours for the typical conditions, consistent with the observational data from Florida storms (Ulanski and Garstang 1978).

The model results show that the intensity of convection depends markedly on the depth of the convergence layer, a parameter often unavailable from surface observations sampled on a mesoscale network. The results, that deeper convergent layers cause more rain, confirm observations reported by Frank (1978), and Song and Frank (1983).

While fixing the mesoscale vertical mass flux at the top of the convergence layer, yet allowing the values of the convergence magnitude and the convergence depth to vary, we investigated the relative contributions of the convergence magnitude and its depth toward the convection and rainfall. For the particular sounding conditions where vapor decreases with height, it is found that a reduction in the convergence depth is associated with a larger vertical moisture flux that supports stronger convection. The experiments confirm that rainfall depends crucially on the thermodynamic structure such as the average vapor mixing ratio of the converging air. Increasing humidity tends to increase the total rainfall when the upward mass flux remains the same.

The findings reported here are based on a particular set of environmental conditions from a midlatitude summer sounding. The specific quantitative results depend on the sounding data. Also, the model assumptions of axisymmetry and warm rain

microphysics affect the specific rainfall amounts stated here. The effects of vertical shear in the large-scale flow are not addressed here but might affect our findings as well.

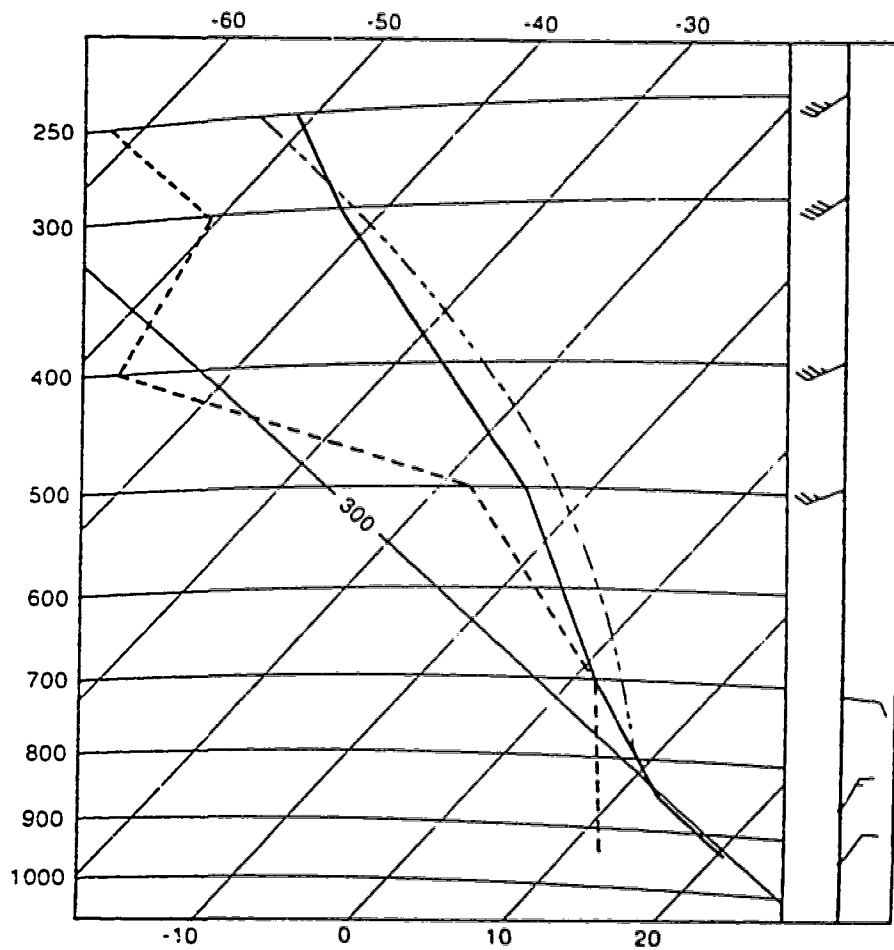


Figure 5.1 Tephigram for sounding at Stony Plain, Alberta on 19 August 1992 depicting temperature (solid) and dewpoint (dashed). The dry adiabat (300 K) and saturated adiabat passing through the lifting condensation level are shown by thin solid and long dashed lines, respectively. The wind profile on the right uses the conventional station model.

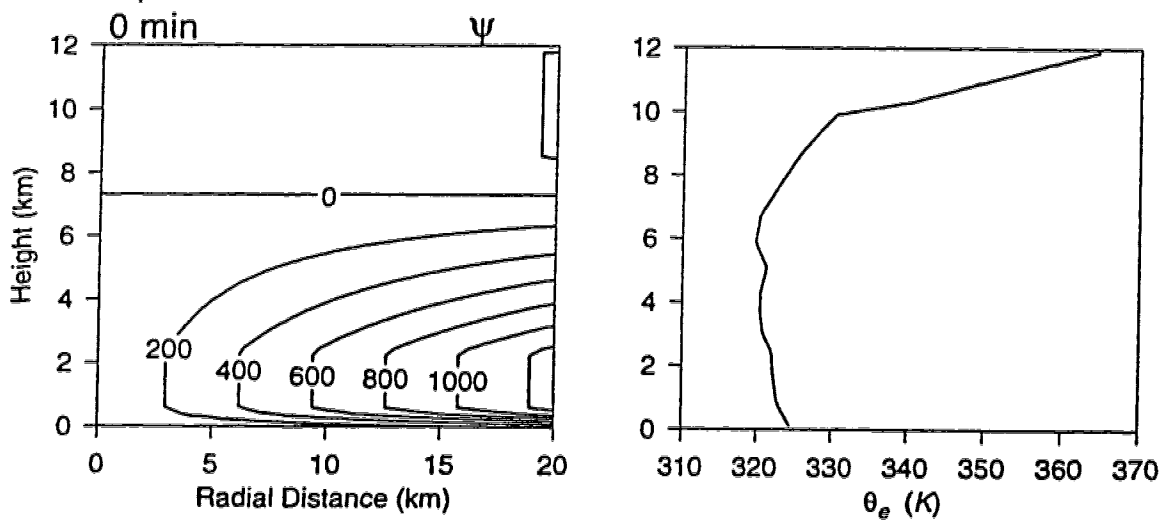


Figure 5.2 Initial conditions for the control case simulation: vertical section of velocity stream function (ψ) contoured every $200 \text{ kgm}^{-1}\text{s}^{-1}$ (left) and vertical profile of equivalent potential temperature (θ_e) (right).

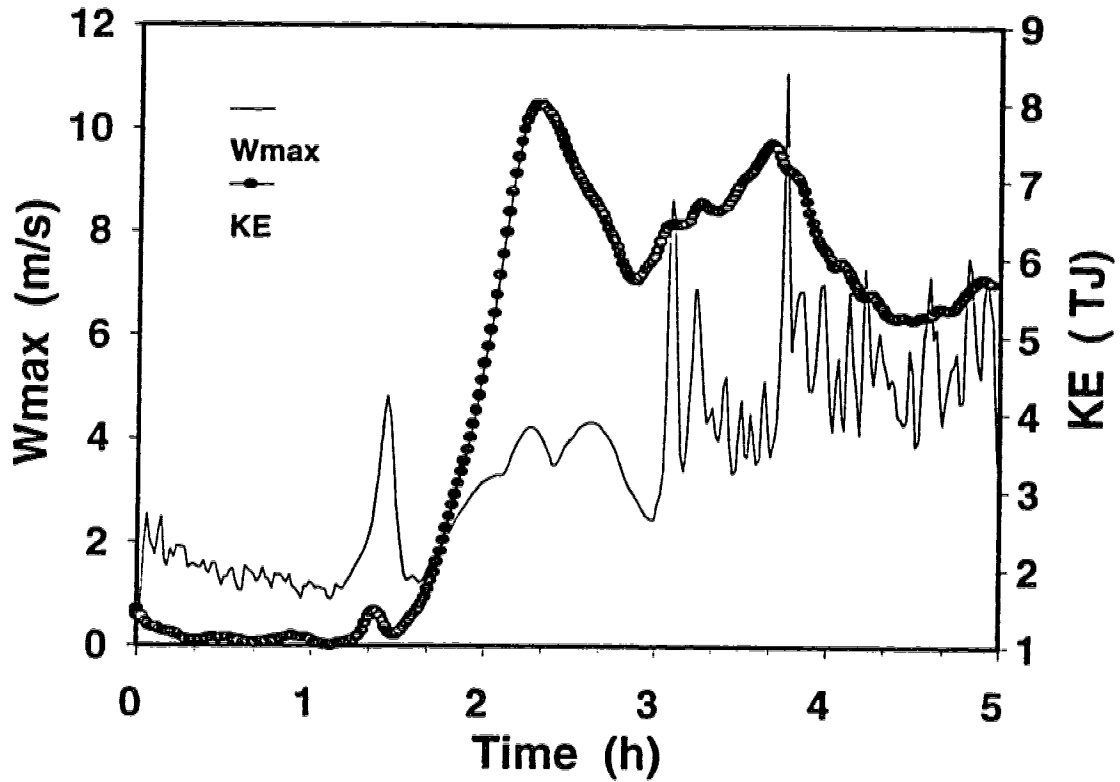


Figure 5.3 Time evolution of maximum vertical velocity w_{max} (thin line) and total kinetic energy KE (line with circles) for the control run. The KE is in units of TJ ($1 TJ=10^{12} J$).

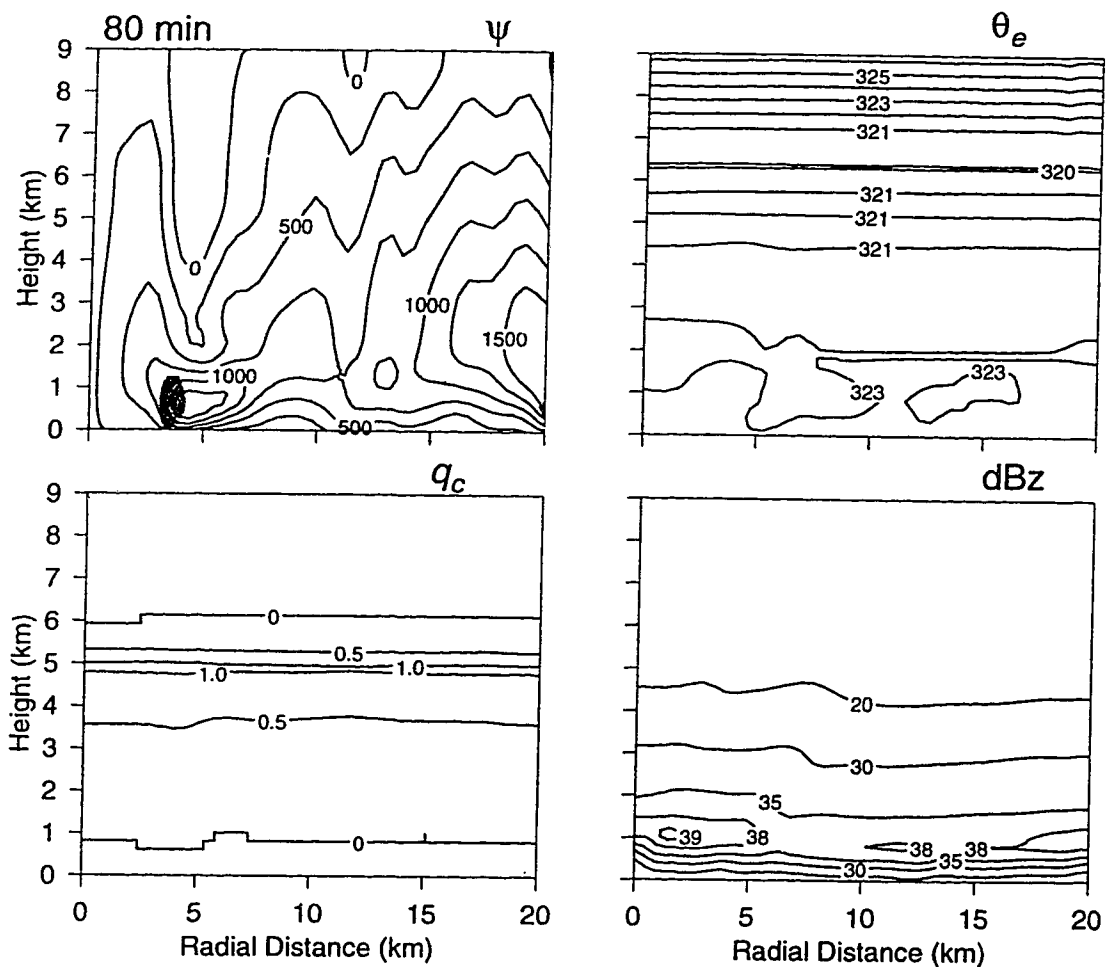


Figure 5.4 Vertical cross sections of stream function (ψ) in $\text{kgm}^{-1}\text{s}^{-1}$, equivalent potential temperature (θ_e) in K, cloud water mixing ratio (q_c) in gkg^{-1} , and radar reflectivity (dBz) at (a) 80 min, (b) 100 min, (c) 140 min, and (d) 180 min for the control run. The shaded areas in the ψ fields denote vertical velocity larger than 1 ms^{-1} (light grey) and larger than 3 ms^{-1} (dark grey), respectively.

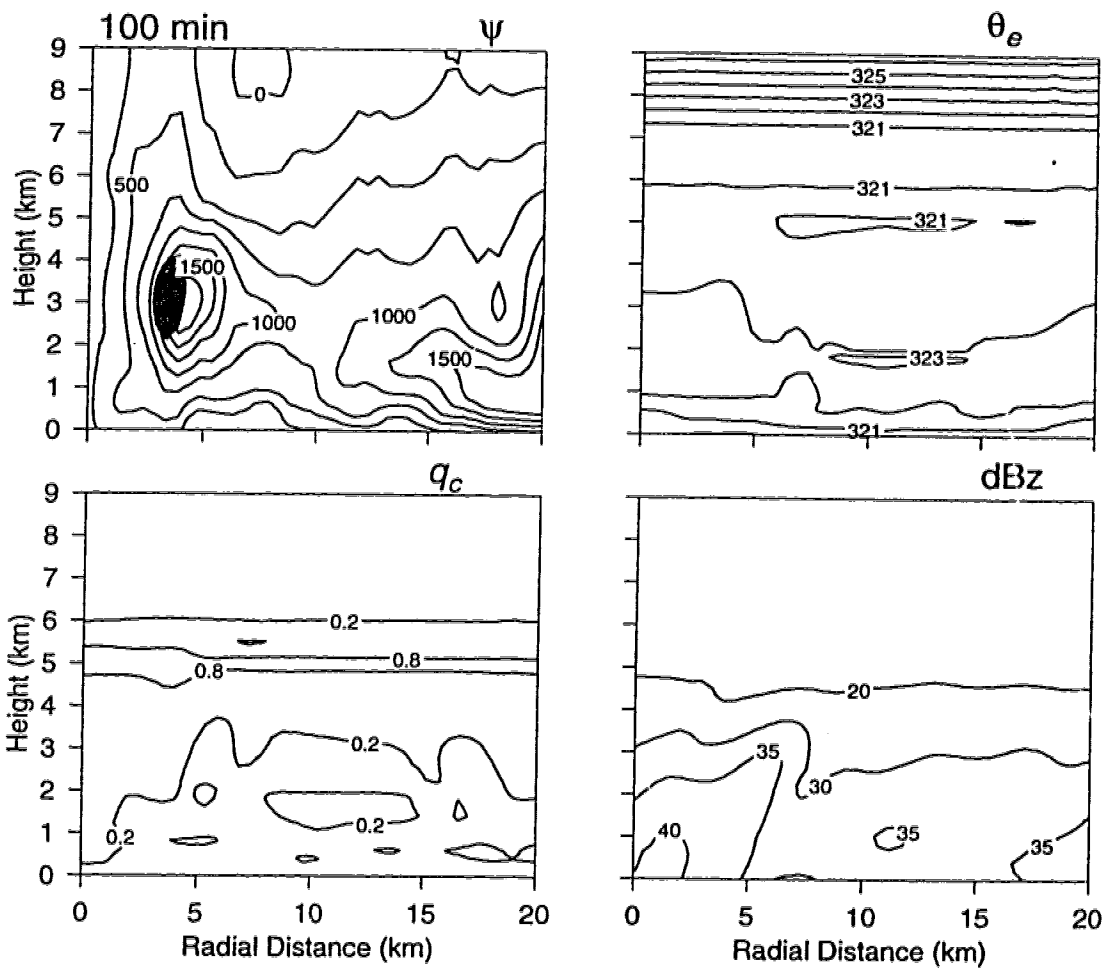


Figure 5.4b

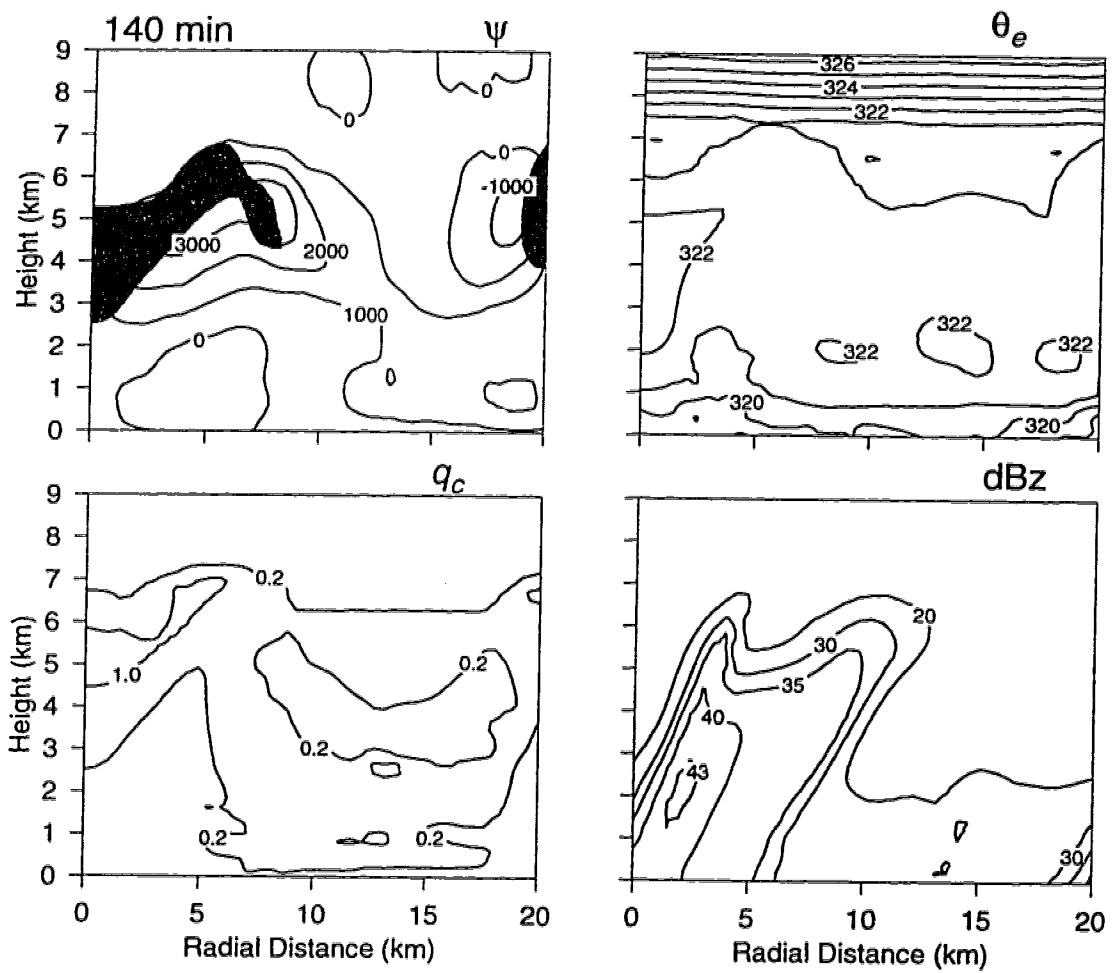


Figure 5.4c

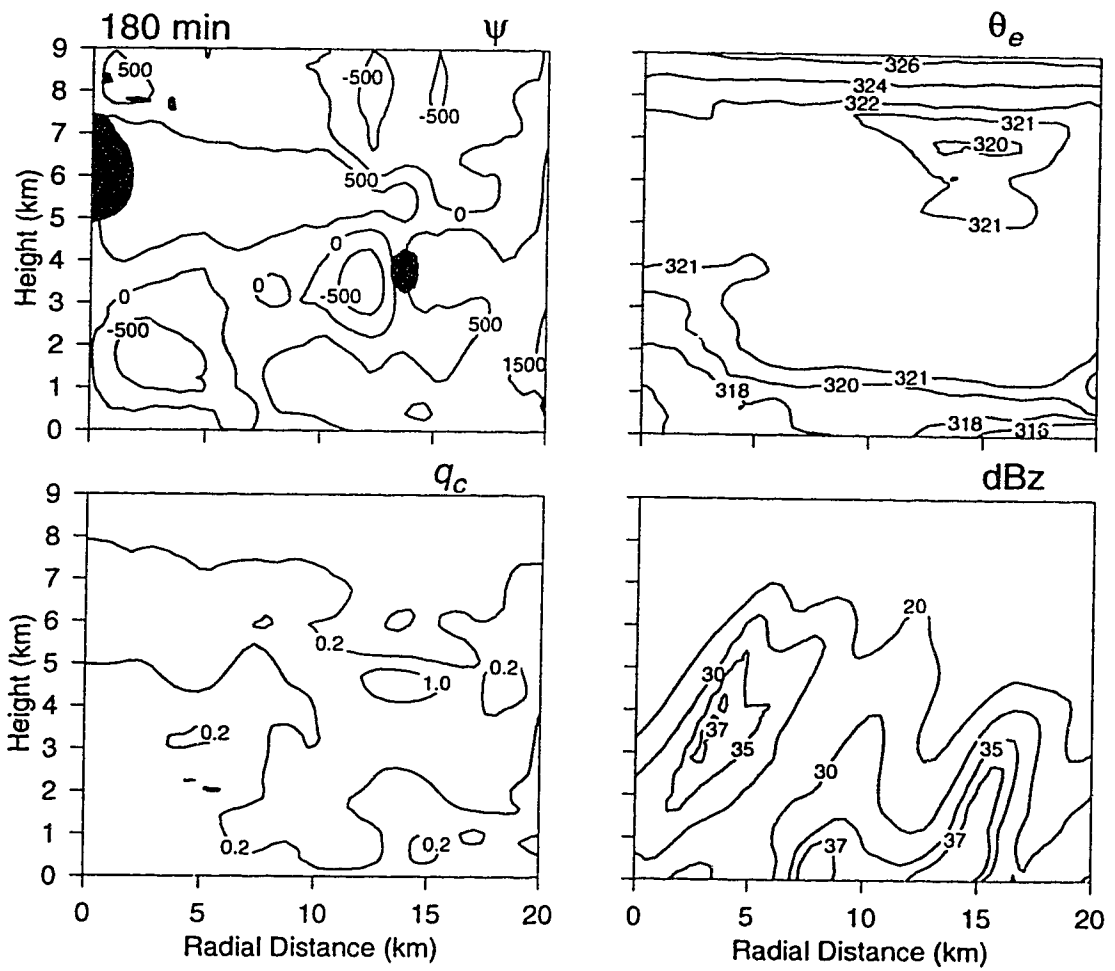


Figure 5.4d

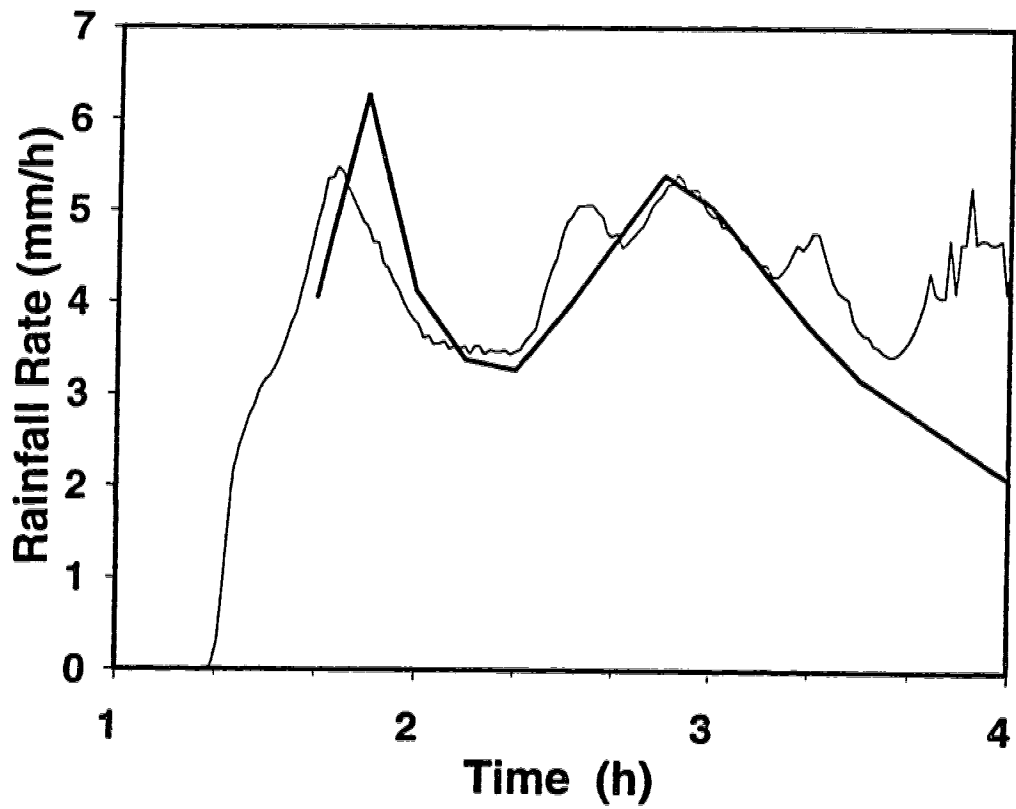


Figure 5.5 Time evolution of radar-observed (thick line) and simulated (thin line) area-averaged rainfall rates. Radar observations were shown from 0630 to 0900 UTC at 10 min intervals.

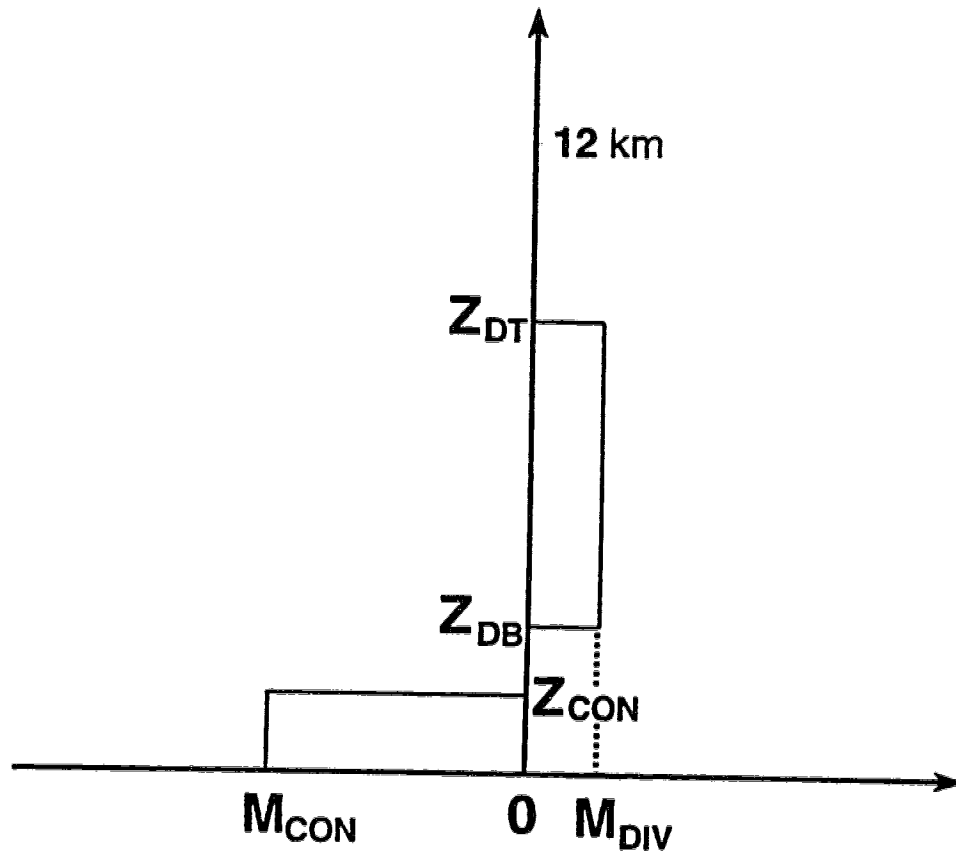


Figure 5.6. Vertical profile of convergence used in sensitivity experiments. M_{CON} and M_{DIV} are the magnitudes of low-level convergence and upper-level divergence, respectively. The convergence extends from the surface to Z_{CON} and the divergence extends from Z_{DB} to Z_{DT} .

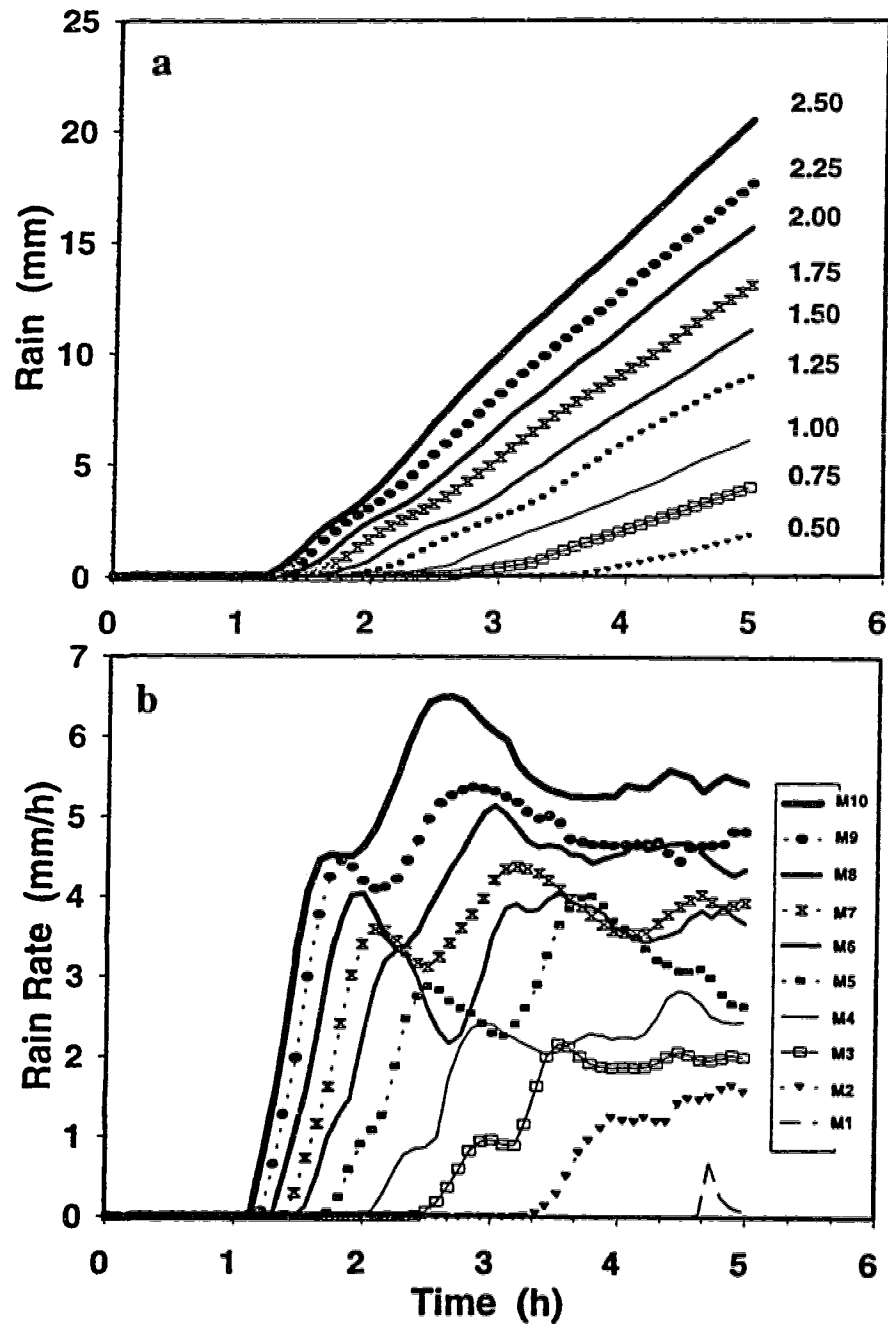


Figure 5.7 Time evolution of (a) rain accumulation on the ground, and (b) rainfall rate for experiments M1 to M10 defined in Table 5.2. The curves in (a) are labelled according to the magnitude of convergence in units of $10^{-4} s^{-1}$.

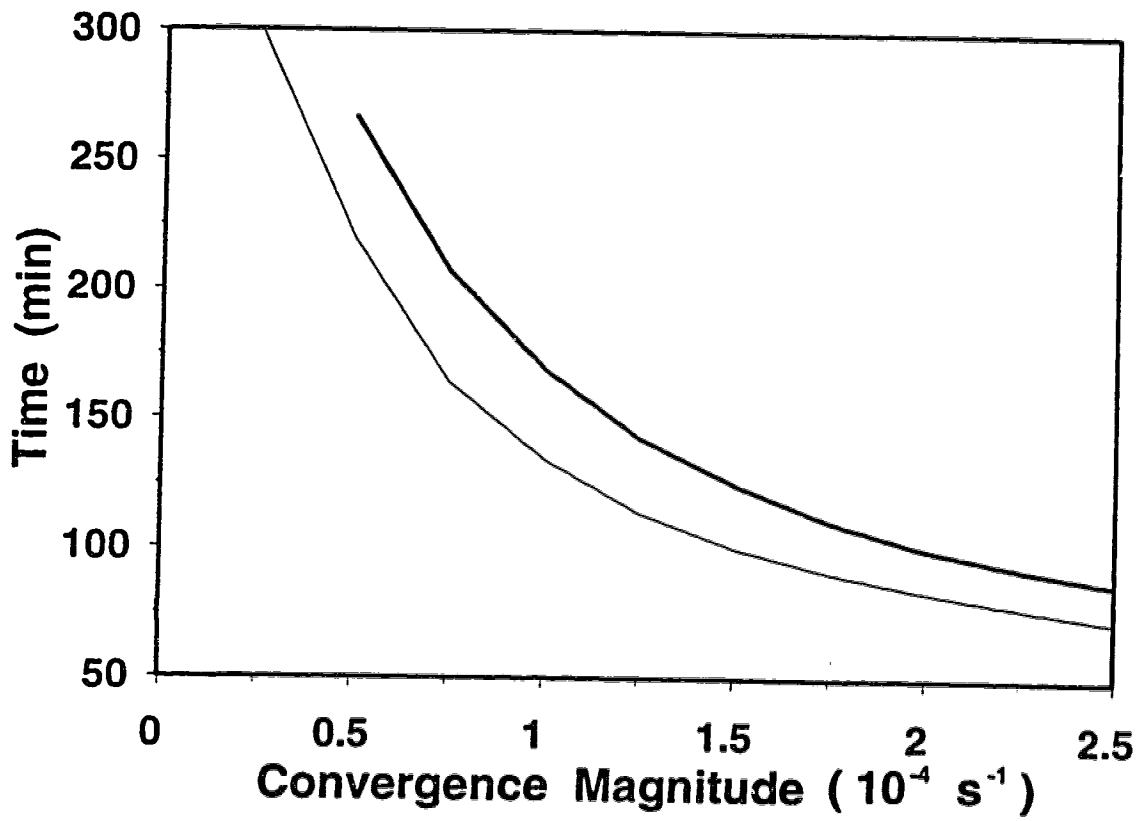


Figure 5.8 Time needed for accumulating rain of 0.1 mm (thin line) and 1 mm (thick line) plotted versus the convergence magnitude.

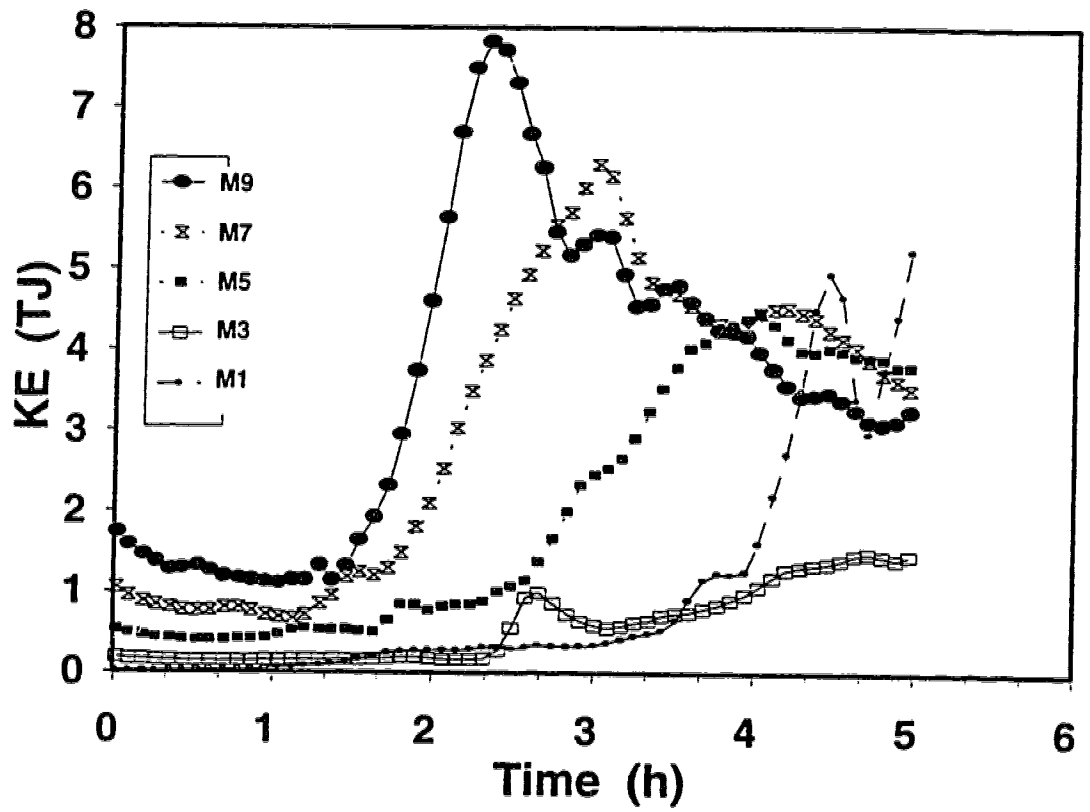


Figure 5.9 Time evolution of total kinetic energy KE for experiments $M1$, $M3$, $M5$, $M7$, and $M9$.

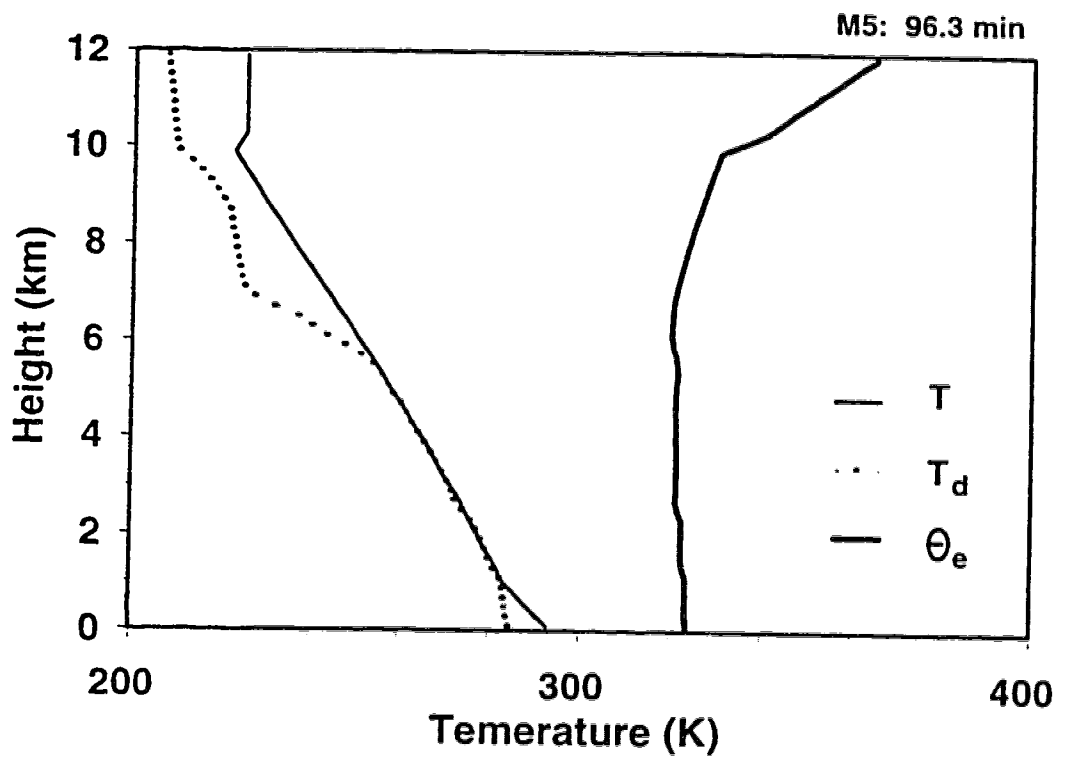


Figure 5.10 Soundings of temperature (solid), dewpoint(dotted), and equivalent potential temperature (thick solid) for experiment M5 at 96.3 minutes just before the onset of convection.

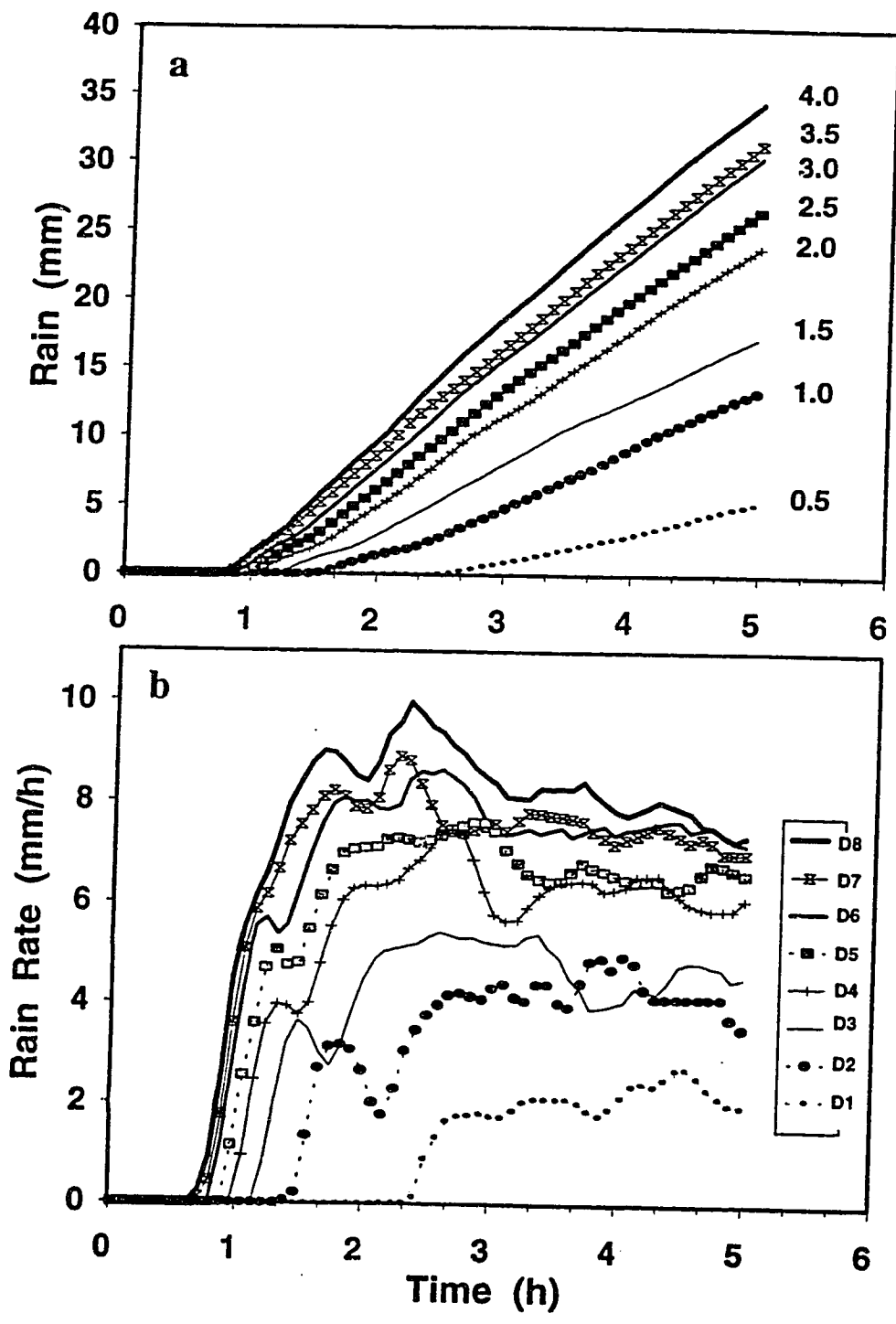


Figure 5.11 Time evolution of (a) area-averaged accumulated rain and (b) rainfall rate for experiments D1 to D8. The curves in (a) are labelled with the depth of convergent layers in km.

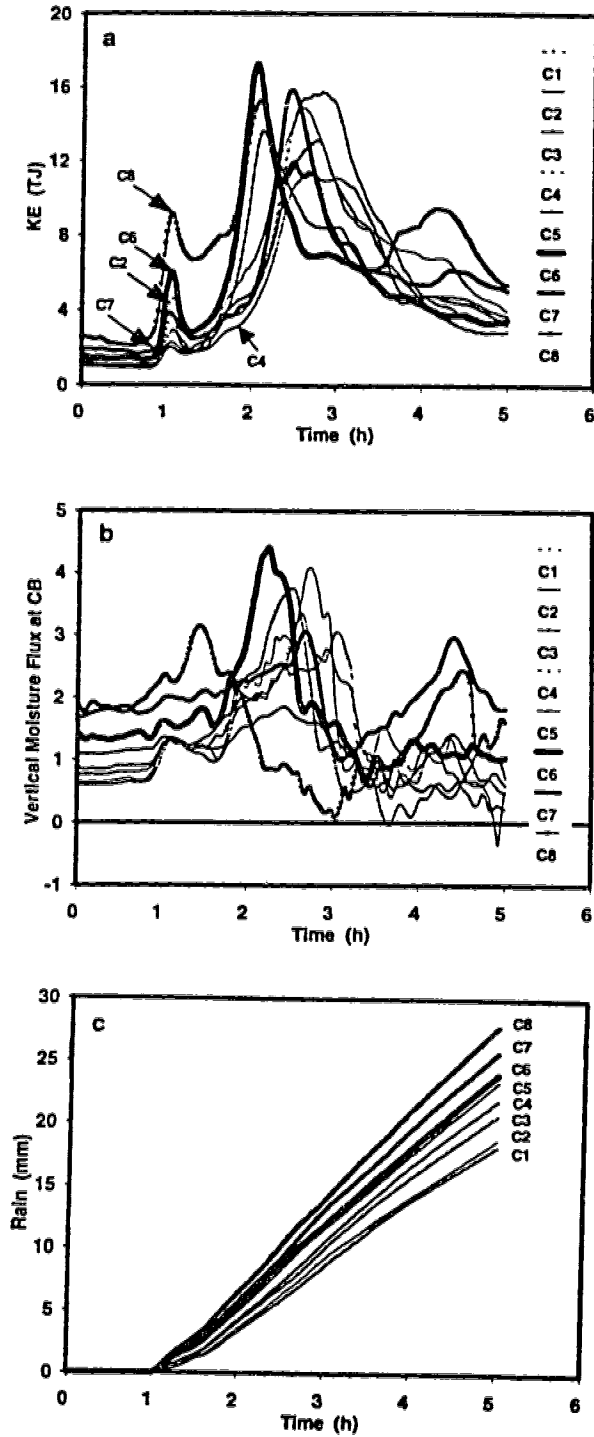


Figure 5.12 Time evolution of (a) total kinetic energy KE, (b) upward water vapor flux through cloud base, and (c) area-averaged accumulated rain for experiments C1 to C8 defined in Table 5.2.

References

- Achtemeier, G.L., 1983: The relationship between the surface wind field and convective precipitation over the St. Louis area. *J. Climate Appl. Meteor.*, **22**, 982-999.
- Bennetts, D. A., and F. Rawlins, 1981: Parameterization of the ice-phase in a model of mid-latitude cumulonimbus convection and its influence on the simulation of cloud development. *Quart. J. Roy. Meteor. Soc.*, **107**, 477-502.
- Byers, H. R., and R. R. Braham, Jr., 1949: *The Thunderstorm*. U.S. Govt. Printing Office, Washington, D. C., 287 pp. [NTIS PB-234-515].
- Caniaux, G., J.-L. Redelsperger, and J.-P. Lafore, 1994: A numerical study of the stratiform region of a fast-moving squall line. Part I: General description and water and heat budgets. *J. Atmos. Sci.*, **51**, 2046-2074.
- Chang, S. M., and H. D. Orville, 1973: Large-scale convergence in a numerical cloud model. *J. Atmos. Sci.*, **30**, 947-950.
- Chen, C. H., and H. D. Orville, 1980: Effects of mesoscale convergence on cloud convection. *J. Appl. Meteor.*, **19**, 256-274.
- Cooper, H. J., M. Garstang, and J. Simpson, 1982: The diurnal interaction between convection and peninsular-scale forcing over South Florida. *Mon. Wea. Rev.*, **110**, 486-503.
- Crook, N. A., and M. W. Moncrieff, 1988: The effect of large-scale convergence on the generation and maintenance of deep moist convection. *J. Atmos. Sci.*, **45**, 3606-3624.
- Dudhia, J., and M.W. Moncrieff, 1987: Numerical simulation of quasi-stationary tropical convective bands. *Quart. J. Roy. Meteor. Soc.*, **113**, 929-967.
- Frank, W. M., 1978: The life cycle of GATE convective systems. *J. Atmos. Sci.*, **35**, 1256-1264.
- Geotis, S. G., 1971: Thunderstorm water contents and rain fluxes deduced from radar. *J. Appl. Meteor.*, **10**, 1233-1237.
- Guan, S., and G. W. Reuter, 1995: Numerical simulation of a rain shower affected by waste energy released from a cooling tower complex in a calm environment. *J. Appl.*

- Meteor.*, **34**, 131-142.
- Hudson, H. R., 1971: On the relationship between horizontal moisture convergence and convective cloud formation. *J. Appl. Meteor.*, **10**, 755-762.
- Koenig, L. R., and W. R. Murray, 1984: Further theoretical studies of the role of splintering in cumulus glaciation. *Quart. J. Roy. Meteor. Soc.*, **110**, 1121-1141.
- Koscielny, A. J., R. J. Doviak, and R. Rabin, 1982: Statistical considerations in the estimation of divergence from single Doppler radar and application to pre-storm boundary-layer observation. *J. Appl. Meteor.*, **21**, 197-210.
- Lee, B. D., R. D. Farley, and M. R. Hjelmfelt, 1991: A numerical case study of convection initiation along colliding convergence boundaries in Northeast Colorado. *J. Atmos. Sci.*, **48**, 2350-2366.
- Lewis, J. M., 1971: Variational subsynoptic analysis with applications to severe local storms. *Mon. Wea. Rev.*, **99**, 786-795.
- Lipps, F. B., and R. S. Hemler, 1986: Numerical simulation of deep tropical convection associated with large-scale convergence. *J. Atmos. Sci.*, **43**, 1796-1816.
- McIlveen, J. F. R., 1986: *Basic Meteorology – a Physical Outline*. Van Nostrand Reinhold (UK) Co. Ltd, 457 pp.
- Ogura, Y., Y.-L. Chen, J. Russel and S.-T. Soong, 1979: On the formation of organized convective systems observed over the eastern Atlantic. *Mon. Wea. Rev.*, **107**, 426-441.
- Purdum, J. F. W., 1976: Some uses of high-resolution GOES imagery in the mesoscale forecasting of convection and its behaviour. *Mon. Wea. Rev.*, **104**, 1474-1483.
- Reuter, G. W., 1987: Penetrative downdrafts in mixed-phase clouds. *S. Afr. J. Phys.*, **10**, 139-145.
- _____, and M. K. Yau, 1987: Mixing mechanisms in cumulus congestus clouds. Part II: Numerical simulations. *J. Atmos. Sci.*, **44**, 798-827.
- _____, 1988: Water budget and kinetic energy transformations of a mixed-phase cumulus cell: Three dimensional numerical simulation. *Beitr. Phys. Atmos.*, **61**, 30-38.
- Rogers, R. R., and M. K. Yau, 1989: *A short course in cloud physics*. 3rd edition, Peramon

- Press, Oxford, 293 pp.
- Schlesinger, R. E., 1984: Effects of the pressure perturbation field in numerical models of unidirectionally sheared thunderstorm convection: Two versus three dimensions. *J. Atmos. Sci.*, **41**, 1571-1587.
- Song, J.-L., and W. M. Frank, 1983: Relationships between deep convection and large-scale processes during GATE. *Mon. Wea. Rev.*, **111**, 2145-2160.
- Soong, S.-T., and Y. Ogura, 1973: A comparison between axisymmetric and slab-symmetric cumulus cloud model. *J. Atmos. Sci.*, **30**, 879-893.
- _____, and _____, 1980: Response of tradewind cumuli to large-scale processes. *J. Atmos. Sci.*, **37**, 2035-2050.
- _____, and W.-K. Tao, 1980: Response of deep tropical clouds to mesoscale processes. *J. Atmos. Sci.*, **40**, 2016-2036.
- Steiner, J. T., 1982: *An axially symmetric cloud model: Development and simulations*. Storm Weather Group Scientific Report MW-94, McGill University, 55 pp.
- Tao, W.-K., and J. Simpson, 1989: Modeling study of a tropical squall-type convective line. *J. Atmos. Sci.*, **46**, 177-202.
- _____, and _____, 1993: Goddard cumulus ensemble model. Part I: Model description. *Terrestrial Atmos. Ocean. Sci.*, **4**, 35-71.
- Tripoli, G. J., and W. R. Cotton, 1980: A numerical investigation of several factors contributing to the observed variable intensity of deep convection over south Florida. *J. Appl. Meteor.*, **19**, 1037-1063.
- _____, and _____, 1982: The Colorado State University three-dimensional cloud / mesoscale model. Part I: General theoretical framework and sensitivity experiments. *J. Rech. Atmos.*, **16**, 185-220.
- Ulanski, S. L., and M. Garstang, 1978: The role of surface divergence and vorticity in the life cycle of convective rainfall. Part I: Observation and analysis. *J. Atmos. Sci.*, **35**, 1047-1062.
- Waldteufel, R., and H. Corbin, 1979: On the analysis of single Doppler data. *J. Appl. Meteor.*, **18**, 532-542.

- Watson, A. I., and D. O. Blanchard, 1984: The relationship between total area divergence and convective precipitation in South Florida. *Mon. Wea. Rev.*, **112**, 673-685.
- Wilson, J. W., and W. E. Schreiber, 1986: Initiation of convective storms at radar-observed boundary-layer convergence lines. *Mon. Wea. Rev.*, **114**, 2516-2536.

CHAPTER 6

STRATIFORM RAINFALL RATES FROM THE WATER FLUX BALANCE EQUATION AND NUMERICAL CLOUD MODEL

Remark: This chapter has been submitted to the *Atmospheric Research* for publication.

6.1 Introduction

It has been long recognized that local rainfall is closely related to the convergence in the boundary layer wind field (e.g., Hudson 1971, Ulanski and Garstang 1978, and Wilson and Schreiber 1986). Observations indicate that low-level convergence greatly supports long-lasting rain events both in the tropics (Ogura et al. 1979, McBride and Gray 1980, Tollerud and Esbensen 1985), and in the mid-latitudes (Maddox 1983, Srivastava et al. 1986, and Heideman and Fritsch 1988). Numerical studies using cloud models confirmed these findings (e.g., Soong and Ogura 1980, Lipps and Hemler 1986, Crook and Moncrieff 1988, and Tao and Simpson 1989).

This chapter deals with the issue of whether estimates of the low-level convergence profile can be used to estimate the rate of precipitation falling from stratiform clouds. Specifically, we examine the accuracy and sensitivity of the water flux balance equation that equates the precipitation rate with the moisture convergence. A brief review of the water flux balance equation is presented first, followed by a more precise statement of the problem.

Within a given column of the atmosphere, conservation of water substance requires that the flux of precipitation must be equal to the upward vapor flux plus the surface evaporation, minus the water storage in the cloud and the possible evaporation at the cloud top (e.g., Holton 1979, p.342), that is:

$$\langle P \rangle = \langle q(z_b) \cdot \rho(z_b) \cdot w(z_b) \rangle + \langle E \rangle - \langle C \rangle \quad (6.1)$$

where P is the precipitation rate ($\text{kg m}^{-2} \text{s}^{-1}$), q the vapor mixing ratio (kg kg^{-1}), ρ the air density (kg m^{-3}), and w the air vertical velocity (ms^{-1}). z_b is the top altitude of the moist boundary layer, E the evaporation rate at the surface and cloud top ($\text{kg m}^{-2} \text{s}^{-1}$), and C the rate of storage of water substance in the cloud and its immediate environment ($\text{kg m}^{-2} \text{s}^{-1}$). The angular brackets represent values averaged over a cross-section area. Since the storage and evaporation of water are relatively small for extensive layer clouds, the rainfall rate from stratiform clouds can be approximated by

$$\begin{aligned} \langle P \rangle &= \langle q(z_b) \rangle \langle \rho(z_b) \cdot w(z_b) \rangle \\ &= \langle q(z_b) \rangle \int_0^{z_b} \langle -\rho \nabla \cdot \mathbf{V} \rangle dz \end{aligned} \quad (6.2)$$

where the mass continuity equation for deep convection $\partial(\rho w)/\partial z = -\rho \nabla \cdot \mathbf{V}$ has been used.

It is difficult to obtain accurate mesoscale convergence, particularly its vertical profile from surface observations and balloon soundings. Instead of in situ measurements, remote sensing offers better opportunities for estimating the vertical profile of mass convergence. With the installation of sensitive Doppler weather radar in North America, western Europe and eastern Asia, mesoscale convergence in stratiform rain regions can be obtained from Doppler velocity data (Rabin and Zrnice 1980, Rabin and Zadwadzki 1984).

With the advent of digital computers, rapid advances have been made in numerical modelling of clouds and storms. Cloud models have been proved particularly useful for investigating physical mechanisms and interactions between dynamic, thermodynamic, and microphysical processes (e.g., Hill 1974, and Reuter and Yau 1987). Models also offer great tools for sensitivity studies because model input variables can be changed in a controlled fashion. Intercomparing the results from such experiments reveals the dependence of an output parameter (such as rainfall) on input variables (e.g., Guan and Reuter 1995). This is impossible from observations that are collected in field experiments, since in nature there are no "repetitions" of identical conditions with only one parameter being changed.

The focus of this chapter is on investigating the accuracy and sensitivity of using the water flux balance relationship (6.2) to estimate rainfall by intercomparing with the results from a time-dependent nonhydrostatic cloud model. By keeping the same initial thermodynamic conditions, yet changing the large-scale divergence profile, model sensitivity experiments are made to show the dependence of area-averaged precipitation rate on various divergence profiles. This allows for systematic examination of the water flux balance equation subjected to different conditions of moisture convergence. Special emphasis is on the magnitude and the depth of the boundary-layer convergence. The precipitation rate here does not represent a point value but an average value with a time-scale of about one hour and a spatial-scale of about 1000 km².

6.2 Numerical Cloud Model

The numerical model used in this study is the modified version of the cloud model developed by Steiner (1982), Reuter and Yau (1987), and Guan and Reuter (1995). It consists of the nonhydrostatic deep anelastic set of equations for conservation of momentum, air mass, heat and water substance. Perturbation pressure is computed from the diagnostic balance equation which is obtained from combining the momentum and continuity equations. Sub-grid scale exchange processes are parameterized using a first-order closure scheme in which the eddy exchange coefficient depends on the local rate of flow velocity-deformation and also on the local lapse rates of temperature and moisture (Hill 1974). To keep the computational requirements manageable, axial symmetry is assumed, that is, the differential equations are written in cylindrical polar coordinates with the tangential gradients set to zero. This assumption is reasonable for modelling clouds in calm wind conditions.

Microphysical processes are modelled using a bulk water parameterization scheme. Three classes of water substance: vapor, cloud water, and rain water, are considered. Cloud water consists of droplets that move along with the surrounding air, whereas rainwater consists of drops that fall with a finite terminal velocity. The rainwater

is assumed to have an exponential size distribution (Marshall and Palmer 1948). Cloud water is converted to rain by auto-conversion and by collection of falling raindrops (Kessler 1969). The threshold value for auto-conversion is a cloud water mixing ratio value of 1 g kg^{-1} . Details about condensation, fallout and evaporation of rain are given in Chapter 4.

Larger-scale convergence forcing is included in the model using a one-way open lateral boundary condition. The radial wind flow at the lateral boundary is kept constant throughout the simulation period as prescribed by a divergence profile. The top and bottom of the domain are rigid and free-slip boundaries. There is no transport of heat and moisture through the top and bottom boundaries except for rainfall at the surface. The model equations are solved numerically using a finite difference scheme on a staggered-grid arrangement. For the results presented in this chapter, the computational domain has a vertical depth of 12 km and a horizontal radius of 50 km. The vertical and radial grid spacings are 200 m and 400 m, respectively.

6.3 Control Case Simulation

6.3.1 Observations on 23 June 1993

To investigate the usefulness of the water flux balance relation for estimating area-averaged rainfall rates, a case with widespread precipitation over central Alberta region was selected. Figure 6.1 shows the sounding sampled at Stony Plain at 0000 UTC on 23 June 1993. The airmass was saturated throughout a thick layer extending from 850 to 600 mb. It was stable for convective overturning with the exception of two shallow conditionally unstable layers near 830 and 740 mb. The lifting condensation level was at 885 mb with a temperature of 7°C . The airmass below 600 mb was moist. Above 500 mb, the air became gradually dry, and the southeasterly flow prevailed.

Precipitation and wind fields were monitored by the Carvel C-band Doppler radar. Radar images (shown in Figure 2.11) indicated that widespread stratiform precipitation covered the entire Alberta region on that day for several hours. Doppler velocity data

were analyzed to retrieve the vertical profile of the area-averaged divergence using the Extended Velocity Azimuth Display (EVAD) technique (Srivastava et al. 1986, and Matejka and Srivastava 1991). In this method, each measured radial velocity is approximated with a truncated harmonic series. The approximations are optimal in that they minimize a cost function consisting of weighted squares of deviations. Details on implementing the EVAD technique for velocity measurements sampled with the Carvel radar were presented in Chapter 2. Figure 6.2 shows the profile of area-averaged divergence derived from the EVAD analysis at 0030 UTC. The divergent (positive) flow beneath the altitude of 0.6 km was presumably related to the precipitation fallout from the cloud base. The flow was convergent over the layer from 0.6 to 2.4 km with a peak value of about $3 \times 10^{-4} \text{ s}^{-1}$. The divergence profile for the heights above 2.5 km could not be estimated since the highest elevation angle of the Carvel radar is only 3.5° . The EVAD analyses show that this divergence profile remained similar throughout the period from 0030 to 0400 UTC (see Figure 2.12). The profile presented in Figure 6.2 was approximated with piece-wise linear segments to provide initial and boundary conditions for the model. To mimic the synoptic observations of a steady surface pressure, the net mass accumulation of air in the model domain was kept at zero by assuming a constant divergence extending from the level of 2.9 km to 8.9 km. A complete profile of divergence used for the control case simulation is:

$$Div(z) = \begin{cases} a_k \cdot z + b_k & Z_k \leq z \leq Z_{k+1}, \quad k=1, \dots, 5 \\ 0 & z > Z_6 \end{cases} \quad (6.3)$$

$$\text{where } a_k = \frac{DIV_{k+1} - DIV_k}{Z_{k+1} - Z_k}, \quad b_k = DIV_k - a_k \cdot Z_k.$$

Here, DIV_k denotes the magnitude of divergence at the altitude of Z_k . Based on (6.3), the divergence decreases linearly from DIV_1 at Z_1 to zero at Z_2 . The convergence first increases from 0 to DIV_3 between the altitude of Z_2 and Z_3 , and then reduces linearly until

it equals zero at Z_4 . The divergence from Z_4 to Z_6 is to balance the net mass inflow at low levels so that a zero mass flux is ensured over the entire domain. Above Z_6 , divergence is set to zero so that the vertical motion near the top boundary is small. In the control run, which is used to simulate the stratiform rain event on 23 June 1993, $DIV_1 = 1.8 \times 10^{-4} \text{ s}^{-1}$, $DIV_3 = -3.2 \times 10^{-4} \text{ s}^{-1}$, and $DIV_{2,4,6} = 0$. The altitudes of Z_k , ($k=1, \dots, 6$) are 0, 0.5, 2.3, 2.9, 5.9 and 8.9 km, respectively.

6.3.2 Simulation results for the control case

Figure 6.3 shows the time evolution of the peak updraft speed and the area-averaged surface rainfall for the control simulation. The peak updraft (defined as the maximum vertical velocity over the entire domain) grows rapidly, reaching an extreme value of 3 ms^{-1} at about 70 min. After this initial spurt, the peak updraft subsides and remains close to 1.3 ms^{-1} for the next two hours. At 3.5 hours of simulation time, the peak upward motion becomes stronger again, oscillating between 1.5 and 3 ms^{-1} . The time history of accumulated rainfall shows that rain reaches the ground at about 50 min and accumulates to 5.6 mm at 2 h. Thereafter, the rainfall accumulation increases with time to a rate of about 3.3 mmh^{-1} . The rainfall rate remains uniform for the remainder of the simulation.

The temporal evolution of the vertical cross-sections of cloud water mixing ratio (not shown) indicates that the simulated cloud is stratiform with a little variability in the horizontal. The precipitation field also shows a stratified feature with only a few short-lived cumulus cells embedded. Figure 6.4 shows the time-height pattern of the horizontally averaged radar reflectivity factor, $\langle Z \rangle$, in a window of $8 \text{ km} \times 6 \text{ hours}$. From 45 to 80 min, $\langle Z \rangle$ develops rapidly. The strongest cell forms at an altitude of 0.5 km with a reflectivity value of 35 dBZ. After 2 hours, $\langle Z \rangle$ weakens gradually aloft. The stratified feature is maintained until the end of the simulation.

6.3.3 Comparison of model results with observations

The model rainfall was compared with surface and radar measurements to clarify

whether the cloud model is suited to evaluate the water flux balance equation for estimating stratiform precipitation. Table 6.1 lists the comparison of the area-averaged 6-hourly accumulated rainfall from the model with the 6-hourly gauge observations from three nearby synoptic stations. The model rainfall rate is computed from the accumulated rainfall in last four hours. The observed rainfall rates averaged over the period of 0000 to 0600 UTC are also given. The comparisons show that the values of modelled accumulated rain and rainfall rate are slightly larger than observed values by about 10% to 15%, depending on which station is considered. This overestimate is within the error margin of rainfall observations. The comparison of observed radar reflectivity at the three stations with the value from the model shows that the differences were less than 1.7 dBZ. The observed reflectivity listed in Table 6.1 was the mean value, which was obtained from radar images and then averaged over the time period from 0000 to 0400 UTC.

Table 6.1 Comparison of cloud model results with radar and surface observations at three synoptic stations in Edmonton.

	<i>6-h Rain (mm)</i>	<i>Rainfall Rate (mmh⁻¹)</i>	<i>Radar Reflectivity (dBZ)</i>
<i>Model</i>	18.5	3.1	31.6
<i>Stony Plain</i>	16.5	2.7	30.9
<i>Municipal Airport</i>	16.0	2.6	30.5
<i>International Airport</i>	16.8	2.8	32.0

6.4 Evaluation of the Water Flux Balance Equation for Estimating Rain Rates

In this section, a comparison is made of the precipitation rate $\langle P \rangle$ estimated from water flux balance equation (6.2) with that computed with the cloud model for various divergence profiles. All cases presented here are based on the same thermodynamic condition (shown in Figure 6.1) and an area-averaged divergence profile with its generic

form sketched in Figure 6.5. Here, Z_2 denotes the depth of the surface convergence layer, which reaches its maximum convergence (CON_{max}) at $Z_1=0$ km. Divergence is assumed over the layer from Z_2 to Z_4 with its maximum value (DIV_{max}) occurring at Z_3 (the mid-altitude of the divergence layer). Based on this divergence profile, (6.2) can be combined with the continuity equation to result in

$$\begin{aligned}
 \langle P \rangle &= \langle q(z_b) \cdot \rho(z_b) \cdot w(z_b) \rangle \approx \langle q(Z_2) \cdot \rho(Z_2) \cdot w(Z_2) \rangle \\
 &= \langle q(Z_2) \rangle \int_0^{Z_2} \rho \cdot CON_{max} \left(\frac{z}{Z_2} - 1 \right) dz \\
 &= -\frac{1}{2} \langle q(Z_2) \rangle \rho^* \cdot CON_{max} \cdot Z_2
 \end{aligned} \tag{6.4}$$

where ρ^* is the mean air density averaged over the layer from $z=0$ to $z=Z_2$. In (6.4), the depth of the moist layer has been estimated by the depth of the convergence layer (i.e., $z_b=Z_2$).

6.4.1 Sensitivity to the magnitude of convergence

Theoretical expression (6.4) gives a relationship between the precipitation rate and divergence profile. In this subsection, numerical experiments are made to examine the dependence of the precipitation rate upon the magnitude of surface convergence (CON_{max}). Two sets of experiments are designed. The first three simulations (CON05, CON10, and CON20) are compared to determine how the peak updraft (w_{max}) and precipitation features are affected by the variation in surface convergence. The other nine simulations (M1-M9) emphasize investigating the quantitative response of rain intensity to the magnitude of low-level convergence.

Figure 6.6 compares the time evolution of w_{max} when CON_{max} is $0.5 \times 10^{-4} \text{ s}^{-1}$ (CON05), $1.0 \times 10^{-4} \text{ s}^{-1}$ (CON10) and $2.0 \times 10^{-4} \text{ s}^{-1}$ (CON20), respectively, while the depth of convergence layers, Z_2 , is kept at 3.0 km. In the first hour, w_{max} increases linearly with the value of CON_{max} because the air flow during this period is controlled by the mesoscale

convergent flow before convection starts. After 1.5 hours, cloud convection develops with a stronger w_{max} when the convergence increases. The peak w_{max} is 4.0 ms^{-1} for simulation CON05, 6.5 ms^{-1} for CON10, and 19 ms^{-1} for CON20.

The height-time pattern of precipitation field for simulations CON05, CON10 and CON20 is shown in Figure 6.7. With the increase of the surface convergence, convection develops earlier and becomes stronger. It takes 2 hours for CON05 to have rain on the ground, whereas about 75 min is needed when the surface convergence is doubled (CON10). This “warming” period for the convection breakout is reduced to 45 minutes when the convergence is further doubled from $1 \times 10^{-4} \text{ s}^{-1}$ to $2 \times 10^{-4} \text{ s}^{-1}$. The cloud in simulation CON20 (Figure 6.7c) is the tallest with its cloud top reaching to 6.5 km. The peak radar reflectivity is also the largest with a value more than 40 dBZ. For simulations CON05 and CON10, the altitudes of cloud top are 5 km and 5.8 km, and the reflectivity maxima are 33 dBZ and 37 dBZ, respectively.

Since the water flux balance equation (6.4) shows a linear relationship between surface convergence magnitude and precipitation rate when the convergence depth is fixed, the accuracy of using this equation to estimate the stratiform rainfall rate should be examined. Simulations M1-M9 are designed, in which CON_{max} is changed from $0.2 \times 10^{-4} \text{ s}^{-1}$ to $1.8 \times 10^{-4} \text{ s}^{-1}$ with an equal interval of $0.2 \times 10^{-4} \text{ s}^{-1}$. The history of rainfall accumulation for these cases (plotted in Figure 6.8a) indicates that: 1) the rainfall amount increases roughly linearly with time; 2) the rainfall increases with larger CON_{max} ; and 3) the onset of precipitation occurs sooner with the increase of the surface convergence. The time required for rain production is reduced from 5.5 hours to 50 minutes when the CON_{max} values are increased from 0.2×10^{-4} to $1.8 \times 10^{-4} \text{ s}^{-1}$. The curves of rainfall rate versus CON_{max} are shown in Figure 6.8b. The model precipitation rate, $\langle P \rangle_{model}$, increases monotonically but nonlinearly with the surface convergence. This is because the vertical moisture flux at the cloud base level is no longer controlled only by mesoscale convergence lifting after convection develops. The $\langle P \rangle_{model}$ values are higher than the $\langle P \rangle$ values suggesting that the simple water flux relationship underestimates precipitation rates by about 25%.

6.4.2 Sensitivity to the depth of convergence layers

Simulations D1-D8 are made to examine the sensitivity of precipitation rate to the variation in the depth of the convergence layer. These runs have the same convergence value: $CON_{max}=1.0\times 10^{-4} \text{ s}^{-1}$, but their convergence depths, Z_2 , differ from 0.5 to 4.0 km. Figure 6.9a shows the evolution of rainfall accumulation. As the convergence depth is increased, more rain accumulates on the ground. Also, the onset of rain becomes more rapid. Rain is produced at about 70 minutes in simulation D8 ($Z_2=4.0$ km), but the time is doubled for simulation D1 ($Z_2=0.5$ km). The rainfall curves for the convergence depths of 2.5 (D5) and 3.0 km (D6) are rather interesting. The similar slopes of the curves indicate their similar rainfall rates. This similarity is related to the sounding profile which shows a very stable layer existing from 2.5 to 3.0 km. The model rainfall curves for D5 and D6, however, differ in that the deeper convergence layer in D6 yields surface rainfall at a slightly earlier time. Comparing the $\langle P \rangle$ and $\langle P \rangle_{model}$ values in Figure 6.9b suggests that the water flux balance equation underestimates the surface rainfall, particularly when deeper convergence layers exist. Nevertheless, $\langle P \rangle$ and $\langle P \rangle_{model}$ curves agree that deeper convergence results in larger rainfall rates when CON_{max} remains unchanged.

6.4.3 Sensitivity to the upper-level divergence

To investigate the sensitivity of rainfall to the distribution of upper-level divergence, four experiments (UD1-UD4) are made. Figure 6.10 shows the divergence profiles used to specify the initial and boundary conditions for these experiments. All four experiments have the same magnitude and depth of convergence ($CON_{max} = 10^{-4} \text{ s}^{-1}$ and $Z_2 = 1.0$ km). The shape of the upper-level divergence profile in all four cases is a symmetric "V" with the divergence top set at the height of 9 km. However, the experiments differ in the depth of their divergence layers. The maximum divergence value is chosen such that the total (density-weighted) height-integrated divergence is zero. That is, the divergence aloft balances the low-level density-weighted convergence to assure the strict

conservation of air mass within the model domain. In all four cases UD1-UD4, surface rainfall starts simultaneously, just after 2 hours (Figure 2.11a). Thus, the onset of rainfall is not affected by the vertical distribution of the upper-level divergence. However, the modelled rainfall amount is slightly sensitive to the divergence profile aloft. When the upper-level divergence is spread out over a deep layer from 1 to 9 km (case UD1), the rainfall is weaker compared to the case when all the divergence occurs in a much more shallow layer from 4 to 9 km (case UD4). The intermediate cases yield rainfall amounts that lie between these two extremes. However, for all cases, the differences in total rainfall is fairly small, varying by less than 20% from 6 mm. Figure 6.11b shows the area-averaged rainfall rates plotted versus divergence maximum. The rainfall rate becomes larger when the magnitude of the divergence maximum is increased (associated with a decrease in the depth of the divergent flow aloft). The model rainfall rates vary between 1.32 and 1.56 mmh⁻¹.

Compared to the model results, an obvious shortcoming of the water flux balance equation $\langle P \rangle = \langle q(z_b) \rho(z_b) w(z_b) \rangle$ is that the precipitation rate is independent of the divergence profile above the level of the moist air layer, z_b . Model results (for cases UD1-UD4) show that the vertical distribution of the upper-level divergence has a certain impact on the rainfall rates even when the total vertically integrated divergence remains unchanged. We did not investigate cases where the total upper-level divergence is increased since this would result in a decrease in mass and cause a drop in surface pressure. Once the surface pressure falls, the low-level convergence field would likely be affected, causing other dynamic feedbacks that would make direct model-model intercomparisons problematic. Suffice it to note here that the simple water flux balance relation misses the effects of the upper-level divergence which can influence the surface rainfall in some conditions.

6.5 Discussion and Conclusion

The water flux balance relation equates the upward water vapour flux with the downward flux of precipitation, thereby providing a simple diagnostic estimate for the area-averaged precipitation rate. In its simplest setting, the precipitation rate equals the product of updraft speed, air density and vapor mixing ratio values that are horizontally averaged at the top of the moist surface layer (z_b). This diagnostic relationship is only appropriate for stratiform rain since its key assumption is that of steady-state balance. The precipitation estimate can be sensitive to z_b when the moist boundary layer is not clearly marked. Often, however, the low-level vapor content profile is rather uniform due to the evaporating rain below cloud base and the turbulent mixing. This makes the particular choice of z_b rather unimportant.

To examine the accuracy of the water flux balance equation for estimating stratiform rainfall rates, results computed with the equation were compared against those obtained from a numerical cloud model. We are aware that the cloud simulations presented here have shortcomings in that they neglect ambient wind shear and ice phase processes. Averaging the rainfall rate over the entire horizontal area and a time span of a few hours should smooth many of the details that are associated with the shear and ice microphysics. Since this model has been found to mimic nature realistically for a particular stratiform rainfall occurrence in central Alberta, it should be a reliable tool for making sensitivity experiments when using the same thermodynamic conditions.

Compared against the cloud model, the water flux balance equation tends to underestimate the area-averaged precipitation rates by about 25% when the low-level convergence magnitude changes. The water flux balance estimates agree with the cloud model ones in that the rainfall increases when the magnitude of the surface convergence becomes larger. The water flux balance yields a strictly linear increase, while the cloud model results suggest a nonlinear increase. Also, the water flux balance relation and the cloud model agree that the precipitation rate increases monotonically when the depth of the convergent flow is increased. However, compared to the model, the water flux balance equation underestimates the increase in rainfall when the convergence layer

becomes very deep. The model results show the effects of upper-level divergence on the intensity of surface rainfall. This contribution is not incorporated in the water flux equation, which is a significant weakness of this simple equation for some conditions.

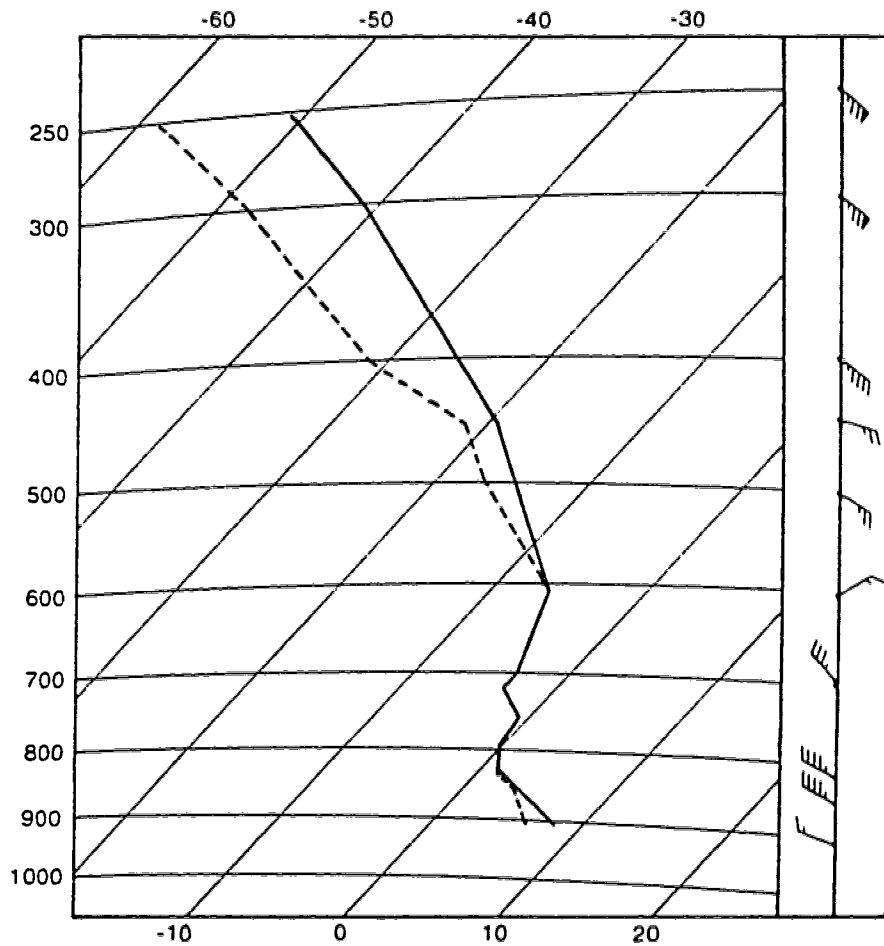


Figure 6.1 Tephigram for sounding at Stony Plain, Alberta (WSE) sampled at 0000 UTC on 23 June 1993. The thick solid line depicts the temperature, and the thick dashed line the dew-point. Full wind barb is 5 ms⁻¹, and the wind flag 10 ms⁻¹.

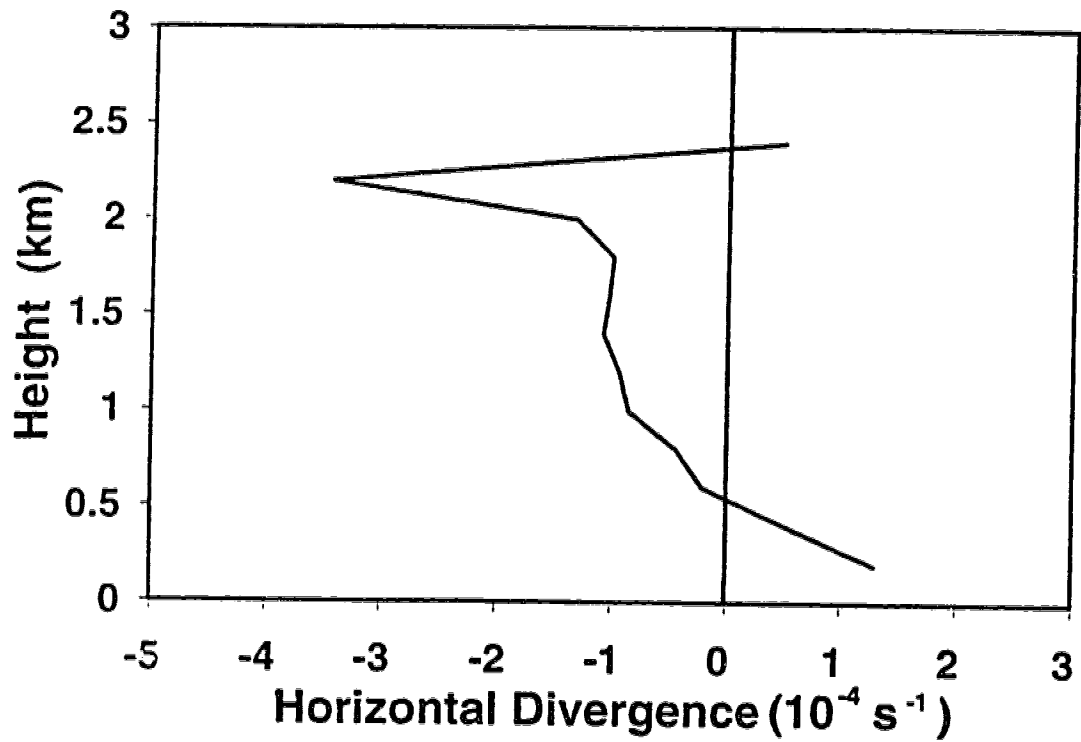


Figure 6.2 Profile of divergence obtained from the Doppler velocity data with the EVAD analysis at 0030 UTC on 23 June 1993.

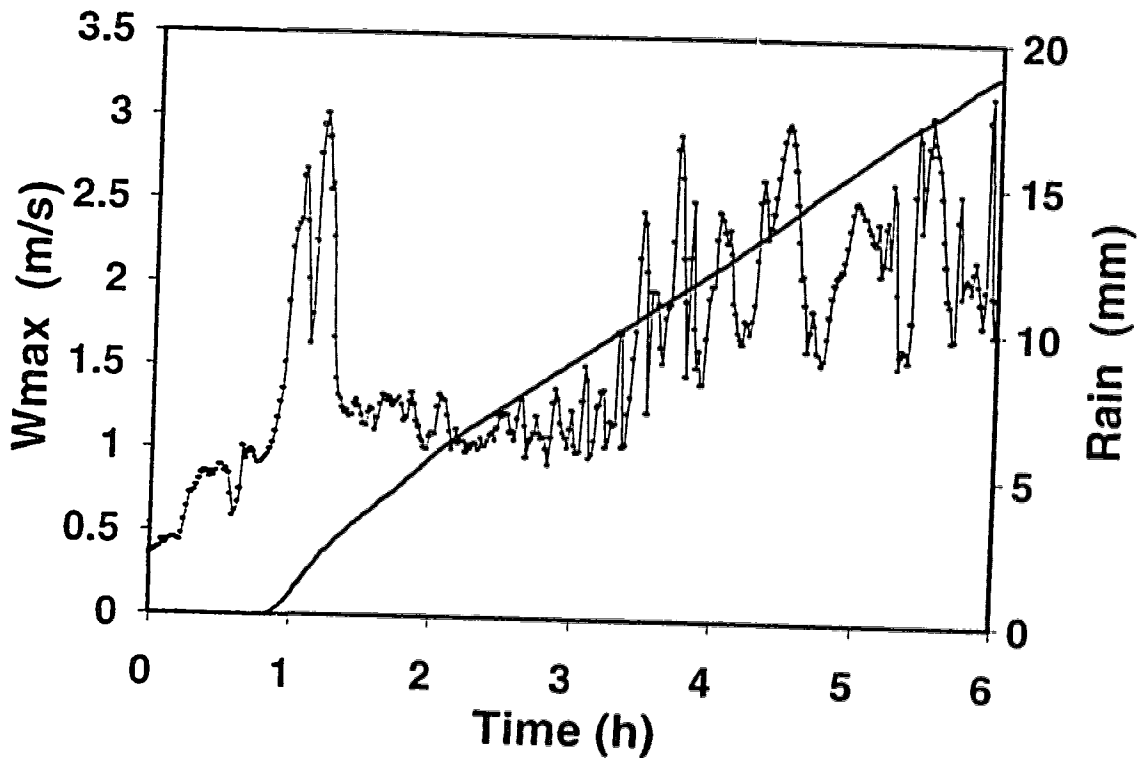


Figure 6.3 Evolution of maximum vertical velocity w_{max} (thin line with dots), and accumulated rain (thick line) for the control case simulation.

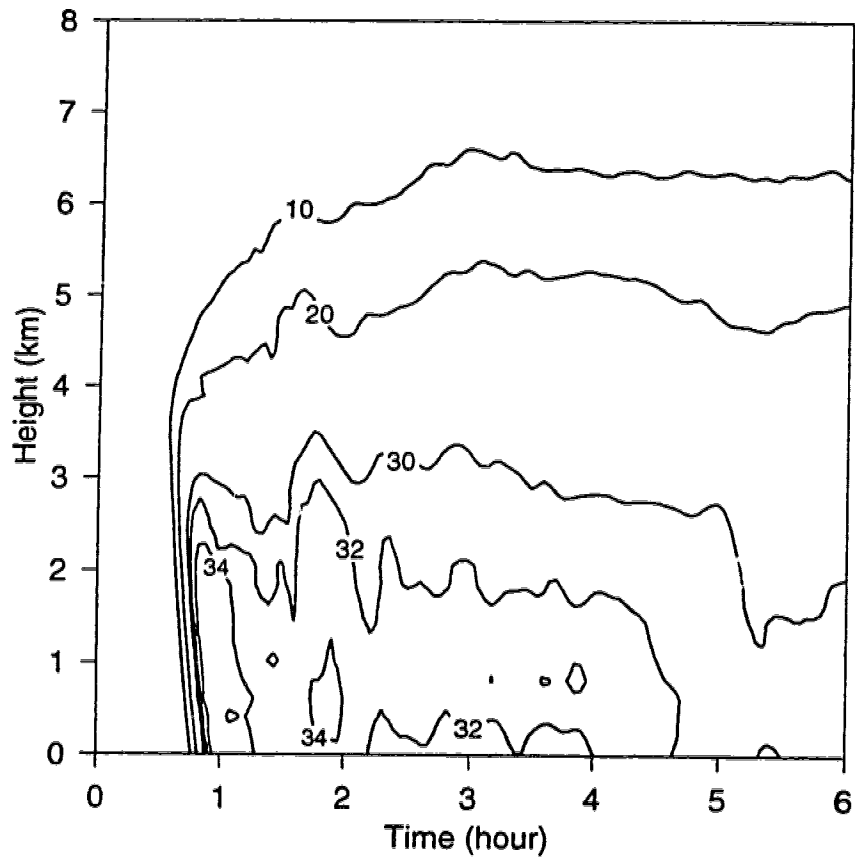


Figure 6.4 Height-time pattern of mean area-averaged radar reflectivity contoured at 10, 20, 30, 32, 34 and 35 dBz for the control case simulation.

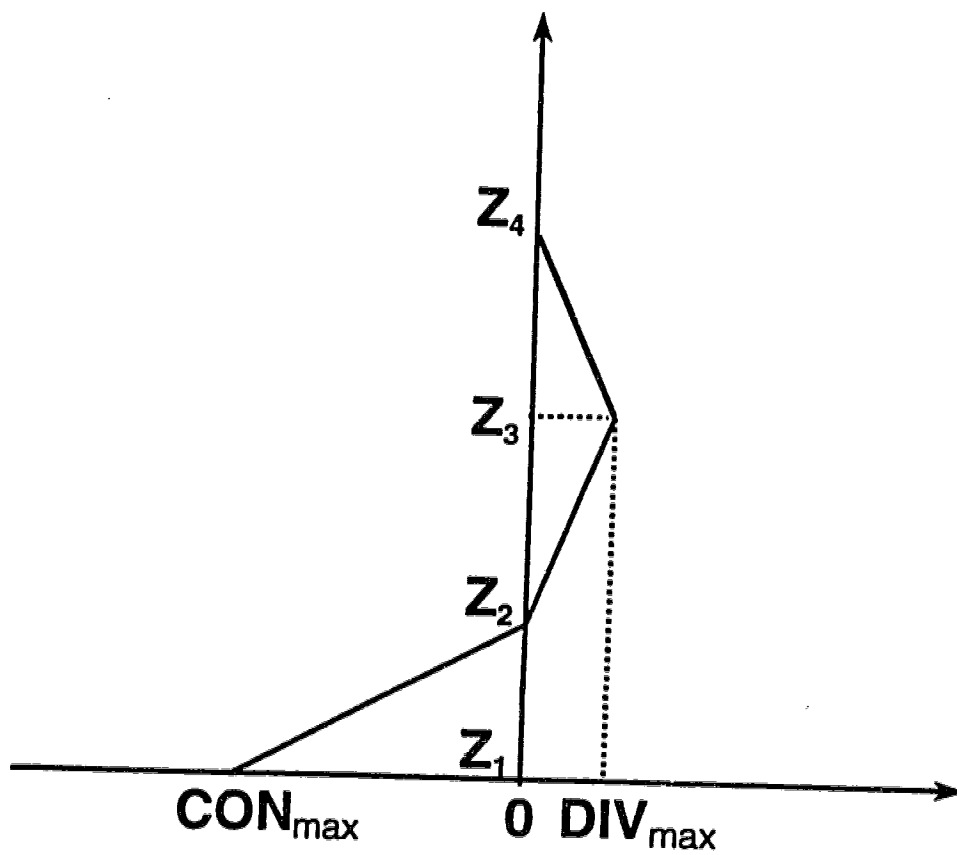


Figure 6.5 Profile of divergence used in numerical simulations CON05, CON10, CON20, M1 to M9, and D1 to D8. CON_{max} and DIV_{max} denote the maximum values of surface convergence and upper-level divergence.

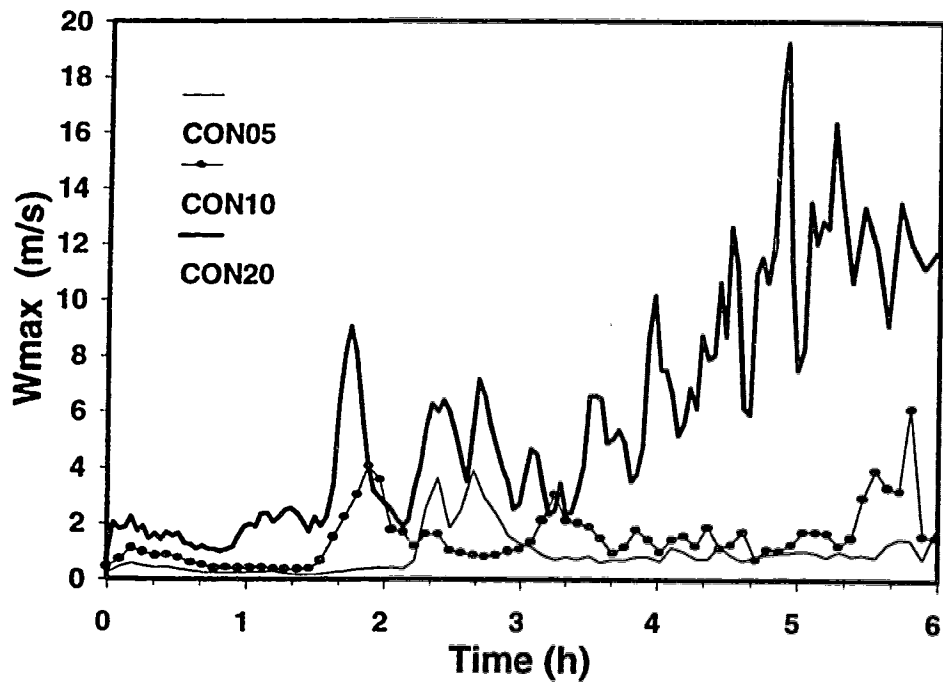


Figure 6.6 Evolution of w_{max} for simulations CON05 (thin line), CON10 (thin line with circles) and CON20 (thick line). The values of CON_{max} in the three experiments are 0.5×10^{-4} , 1.0×10^{-4} and $2.0 \times 10^{-4} s^{-1}$, respectively.

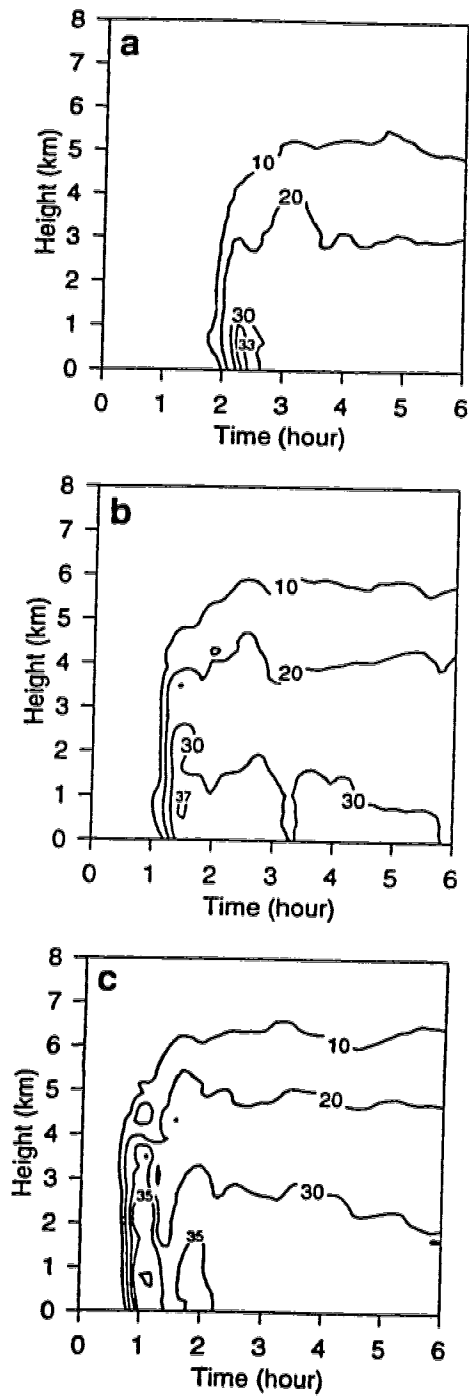


Figure 6.7 Height-time pattern of mean area-averaged radar reflectivity for simulations (a) CON05, (b) CON10, and (c) CON20. The peak reflectivity values are 33, 37 and 38 dBz, respectively.

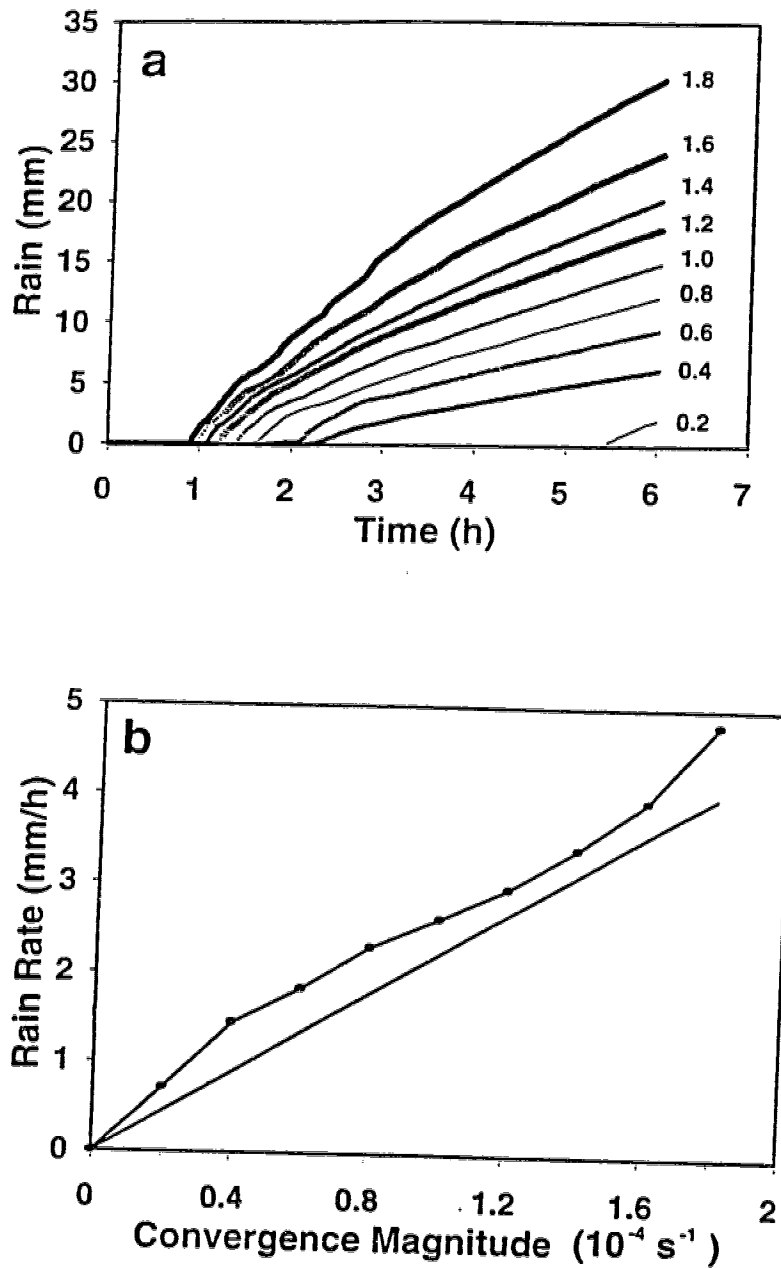


Figure 6.8 (a) Area-averaged accumulated rainfall plotted versus time for simulations M1 to M9. The curve labels list the magnitude of convergence maximum (CON_{max}) in units of $10^{-4} s^{-1}$. (b) Area-averaged rainfall rate plotted versus surface convergence magnitude (CON_{max}). The solid line shows the water flux balance relationship, while the line with data points shows the cloud model results.

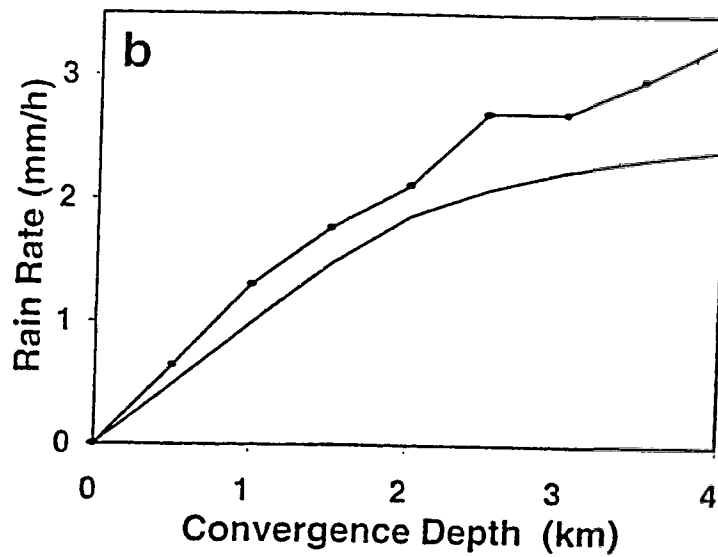
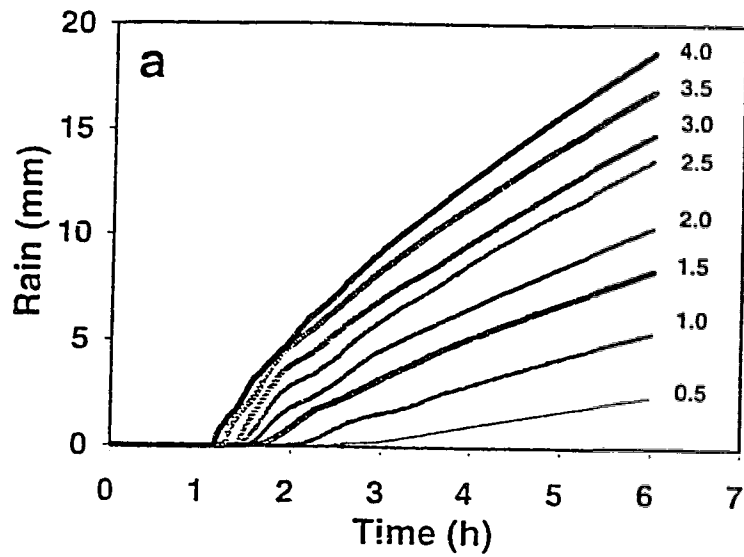


Figure 6.9 (a) Area-averaged accumulated rainfall plotted versus time for simulations D1 to D9. The curve labels list the depth of convergence layer (Z_2) in units of km. (b) Area-averaged rainfall rate plotted versus convergence depth (Z_2). The solid line shows the water flux balance relationship, while the line with data points shows the cloud model results.

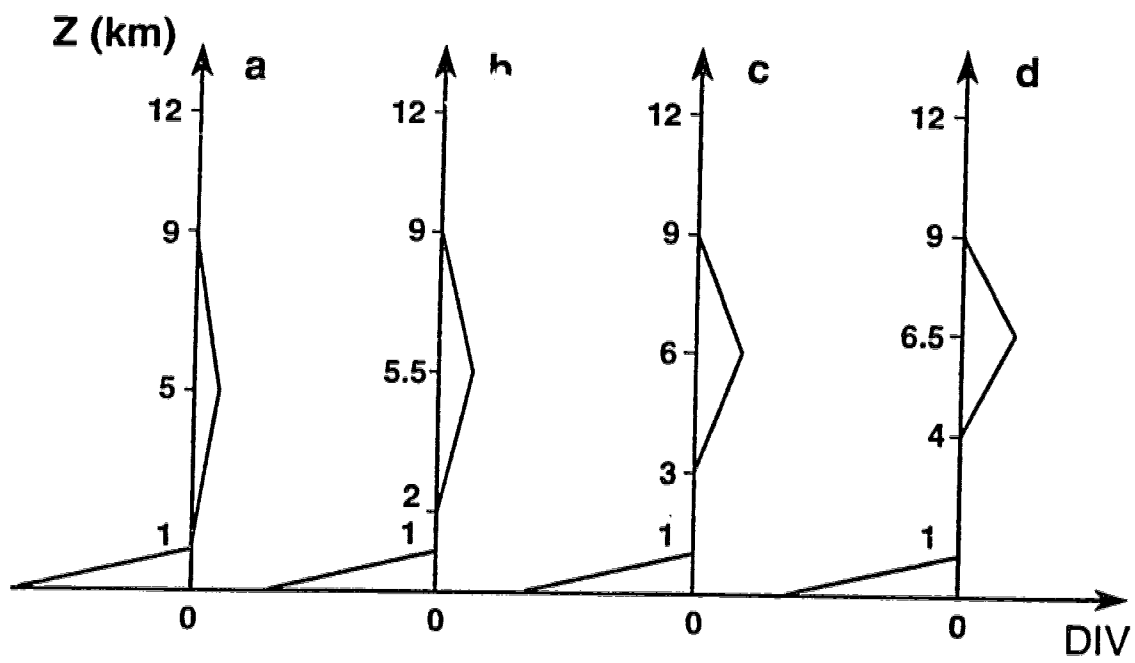


Figure 6.10 Vertical profile of divergence used in cloud simulations (a) UD1, (b) UD2, (c) UD3, and (d) UD4

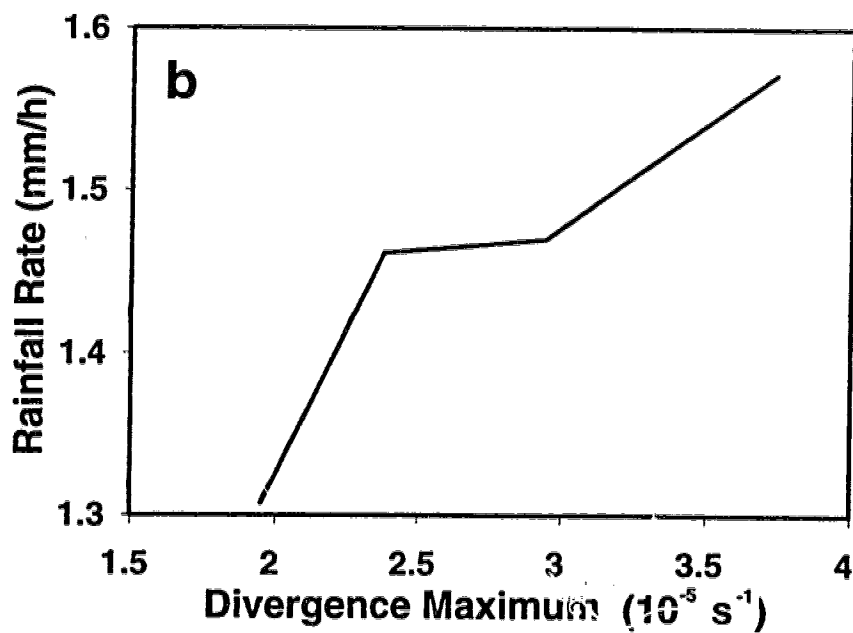
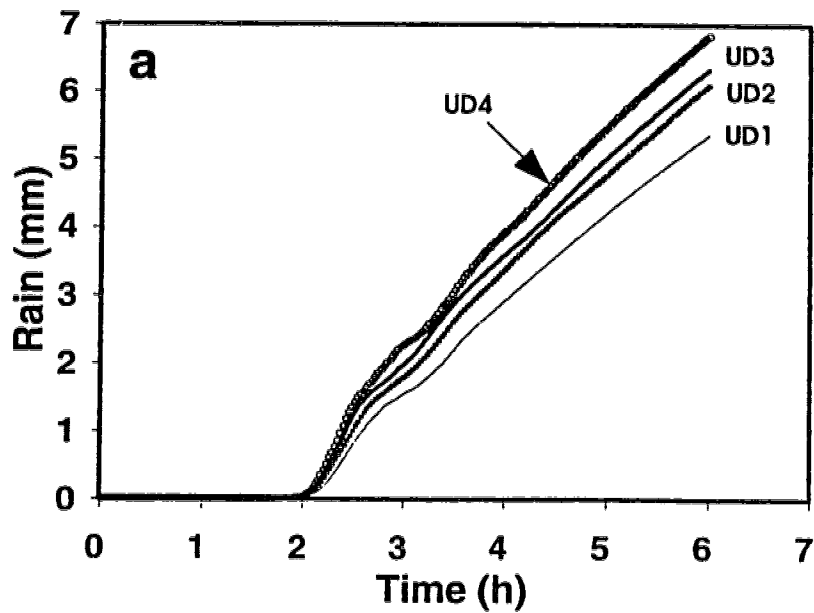


Figure 6.11 (a) Area-averaged accumulated rainfall plotted versus time for simulations UD1 to UD4. (b) Area-averaged rainfall rate plotted versus maximum divergence value based on model simulation results.

References

- Crook, N. A., and M. W. Moncrieff, 1988: The effect of large-scale convergence on the generation and maintenance of deep moist convection. *J. Atmos. Sci.*, **45**, 3606-3624.
- Guan, S., and G. W. Reuter, 1995: Numerical simulation of a rain shower affected by waste energy released from a cooling tower complex in a calm environment. *J. Appl. Meteor.*, **34**, 131-142.
- Heideman, K. F., and J. M. Fritsch, 1988: Forcing mechanisms and other characteristics of significant summertime precipitation. *Wea. Forecasting*, **3**, 115-130.
- Hill, G. E., 1974: Factors controlling the size and spacing of cumulus clouds as revealed by numerical experiments. *J. Atmos. Sci.*, **31**, 646-673.
- Holton, J. R., 1979: *An Introduction to Dynamic Meteorology*. 2nd edition. Academic Press. New York, 391 pp.
- Hudson, H. R., 1971: On the relationship between horizontal moisture convergence and convective cloud formation. *J. Appl. Meteor.*, **10**, 744-762.
- Kessler, E., 1969: *On the Distribution and Continuity of Water Substance in Atmospheric Circulations*. Meteor. Monogr., No. 32, Amer. Meteor. Soc., 84 pp.
- Lipps, F. B., and R. S. Hemler, 1986: Numerical simulation of deep tropical convection associated with large-scale convergence. *J. Atmos. Sci.*, **43**, 1796-1816.
- Maddox, R. A., 1983: Large-scale meteorological conditions associated with midlatitude, mesoscale convective complexes. *Mon. Wea. Rev.*, **111**, 1475-1493.
- Marshall, J. S., and W. M. Palmer, 1948: The distribution of raindrops with size. *J. Meteor.*, **5**, 165-166.
- Matejka, T. J., and R. C. Srivastava, 1991: An improved version of the extended velocity-azimuth display analysis of single-Doppler radar data. *J. Atmos. Oceanic Technol.*, **8**, 453-466.
- McBride, J. L., and W. M. Gray, 1980: Mass divergence in tropical weather system. Part I: Diurnal variations. *Quart. J. Roy. Meteor. Soc.*, **106**, 501-516.
- Ogura, Y., M.-T. Liou, J. Russell, and S. T. Soong, 1979: On the formation of organized convective systems observed over the eastern Atlantic. *Mon. Wea. Rev.*, **107**, 426-

441.

- Perkey, D. J., and R. A. Maddox, 1985: A numerical investigation of a mesoscale convective system. *Mon. Wea. Rev.*, **113**, 553-566.
- Rabin, R. M., and I. Zawadzki, 1984: On the single Doppler measurements of divergence in clear air. *J. Atmos. Oceanic Technol.*, **1**, 50-57.
- , and Zrníc, D. S., 1980: Subsynoptic-scale vertical wind revealed by dual-Doppler radar and VAD analysis. *J. Atmos. Sci.*, **37**, 644-654.
- Reuter, G. W., and M. K. Yau, 1987: Mixing mechanisms in cumulus congestus clouds. Part II: Numerical simulations. *J. Atmos. Sci.*, **44**, 798-827.
- Soong, S.-T., and Y. Ogura, 1973: Response of trade wind cumuli to large-scale processes. *J. Atmos. Sci.*, **37**, 2035-2050.
- Srivastava, R. C., T. J. Matejka, and T. J. Lorello, 1986: Doppler radar study of the trailing anvil region associated with a squall line. *J. Atmos. Sci.*, **43**, 356-377.
- Steiner, J. T., 1982: *An Axially Symmetric Cloud Model: Development and Simulations*. Storm Weather Group, Scientific Report. MW-94, McGill University, 55 pp.
- Tao, W.-K., and J. Simpson, 1989: Modelling study of a tropical squall-type convective line. *J. Atmos. Sci.*, **46**, 177-202
- Tollerud, E. I., and S. K. Esbensen, 1985: A composite life cycle of nonsquall mesoscale convective systems over the tropical ocean. Part I: Kinematic fields. *J. Atmos. Sci.*, **42**, 823-837.
- Ulanski, S. L., and M. Garstang, 1978: The role of surface divergence and vorticity in the life cycle of convective rainfall. Part I: Observations and analysis. *J. Atmos. Sci.*, **35**, 1047-1062.
- Watson, A. I., and D. O. Blanchard, 1984: The relationship between total area divergence and convective precipitation in South Florida. *Mon. Wea. Rev.*, **112**, 673-685.
- Wilson, J. W., and W. E. Schreiber, 1986: Initiation of convective storms at radar-observed boundary-layer convergence lines. *Mon. Wea. Rev.*, **114**, 2516-2536.

CHAPTER 7

CONCLUSIONS

This thesis combines Doppler weather radar measurements with high-resolution numerical cloud modelling to investigate how rainfall is affected by meso-scale convergence profiles. The first major objective of this thesis was to obtain estimates, from a single ~~operational~~ Doppler radar, of the kinematic properties of wind field for both convective and stratiform precipitation systems. The second major objective was to quantify the effects of mesoscale convergence on precipitation using numerical cloud simulations.

Two summer cases in central Alberta were examined: a multicellular thunderstorm, and a long-lasting nimbostratus event. The Volume Velocity Processing (VVP) algorithm with seven-parameters was used to extract the convergence field in scattered-echo regions for the convective case. Analysis results show that heavy echo cells were preceded by up to 30 minutes by strong low-level convergence. Convective cells tended to develop in the areas with strong convergence and moderate to strong vertical shear values. The accuracy of the VVP convergence estimate largely depended on the size and the shape of the analysis volume. Our analysis suggests that the analysis volume should have an azimuthal width of 30° or larger and a radial extent of 20 km or more. The accuracy of the VVP convergence estimates reached about 10^{-5} s^{-1} for a 40° azimuth \times 20 km range sector volume. This precision is one order less than the typical convergence magnitudes observed in moderate to intense storms (Ogura and Chen 1977) and thus meaningful to monitor the storm development. Due to the limitation of sampling azimuthal coverage and the non-orthogonality of harmonic functions in the analysis volume, the VVP processing can provide the estimates for divergence, deformation, vertical shear, and horizontal winds with fair accuracy, but neglects the remaining vertical wind terms for a linear wind field. The uncertainty in all estimates was found to increase linearly with the errors in radial velocity measurements.

For widespread stratiform precipitation, the profile of the area-averaged divergence was deduced by employing the Extended Velocity Azimuth Display (EVAD) algorithm. Error analyses were performed in simulated wind fields to investigate the sensitivity of the technique to radar parameters, such as radar maximum elevation angle and radar horizontal detection range. The results suggest that using either higher elevation angles or larger horizontal detecting range would raise the altitude below which the divergence can be obtained accurately. For the limited scans used by the Carvel radar (three low elevation angles), the profile of the EVAD-deduced divergence could be estimated accurately up to an altitude of about 2.0 km when using an analysis cylinder radius of 60 km. The inaccuracy of the EVAD divergence estimates was found to increase with the uncertainty inherent in Doppler velocity measurements. The divergence estimate is not contaminated by the fall speed of hydrometeors, supporting the conclusion of Srivastava et al. (1986). The analyses on 23 June 1993 show that the widespread precipitation was associated with a convergence layer from an altitude of 0.6 to 2.2 km with a convergence intensity exceeding $2 \times 10^{-4} \text{ s}^{-1}$, whereas the divergent flow beneath 0.6 km was related to the precipitation fallout below the cloud base. The convergence was maintained for more than three hours and resulted in a typical, long-lasting continuous ascending motion in stratus.

Numerical simulations of the convective and stratiform rain events were made using an axi-symmetric cloud model. This model, which is suitable to simulate warm rain processes under a large-scale convergence forcing, is an extension of Steiner's axisymmetric model. In the modified version of the model, heat and moisture are allowed to be advected into the domain through the lateral boundary. Thus, the model is initiated by the convergence forcing without any thermal or moisture perturbation. This approach is considered superior to previous studies (e.g., Chang and Orville 1973, and Guan and Reuter 1995) in that the effects of purely dynamic forcing on precipitation could be evaluated. Sounding data recorded at Stony Plain and the convergence information retrieved from the Carvel Doppler radar were used to initialize the model. Surface and radar observations served as the data sets for comparison with the model simulations. The

cloud model simulated realistically the evolution of observed rain events.

Numerical sensitivity experiments were conducted to quantify changes in convection and precipitation arising from changes in the magnitude of the low-level convergence and the convergence depth. Our approach is novel in that the relative contribution of the convergence magnitude versus the convergence depth to convective rain showers was investigated. Also, the effect of upper-level divergence on the stratiform surface rainfall was examined. The major findings of these investigations are:

(1) For both convective and stratiform clouds, the rainfall is enhanced when either the magnitude or the depth of convergence layers is increased. The accumulated rain increases monotonically with stronger convergence but not in a linear fashion.

(2) Stronger convergence or deeper convergence layers accelerate the onset of rainfall reaching the ground. The lag time from the beginning of convergence to the beginning of convective rainfall was about 1 to 2 hours when the convergence depth is changed.

(3) When fixing the mesoscale vertical mass flux at the top of the convergence layer, yet allowing the values of the convergence magnitude and the convergence depth to vary, we investigated the relative contributions of the convergence magnitude and its depth toward the convective rainfall. For the particular sounding we considered, a reduction in the convergence depth is associated with a larger vertical moisture flux which supports stronger convection. The experiments confirm that convective rainfall depends crucially on the thermodynamic structure, such as the average vapor mixing ratio of the converging air. Increasing humidity enhances the total rainfall when the upward air mass flux remains the same.

(4) Calculation of stratiform precipitation using a water flux balance equation is biased to underestimate the area-averaged rainfall rates. For the specific stratiform case investigated, the underestimate was about 25%.

(5) Upper-level divergence does not affect the onset time of the stratiform rain, but stronger upper-level divergence tends to enhance the surface rain. Neglecting the contribution of the upper-level divergence to the surface rainfall in the water flux balance

equation is a significant weakness of this simple equation for some conditions.

Our model results indicate that both the magnitude and the depth of the mesoscale convergence affect the development of cloud and local surface rainfall. Although a meso-network of surface stations can provide an estimate of the magnitude of surface convergence (e.g., Lee et al. 1991), information about the actual depth of the boundary layer convergence cannot be supplied. An advantage of using a sensitive Doppler weather radar is that it can indeed estimate an area-averaged convergence as a function of height. The data analyses in this thesis suggest that a divergence profile can be obtained from single-Doppler radar data for certain meteorological conditions. For the Carvel radar, the convergence magnitude can typically be estimated within a 25% error or less. This would result in an uncertainty of 30% or less in the 5-hour rainfall accumulation according to our model simulation for the environmental conditions of 19 August 1992. For the stratiform precipitation, model simulations suggest that the 6-h accumulated rainfall varies by 16% when the convergence magnitude is changed by 10%. The 10% uncertainty in the convergence is well within the capability of the EVAD analysis for the stratiform rain case (see Chapter 2).

This study, together with others, indicates the potential of combining a single Doppler radar with a numerical model to improve mesoscale nowcasting and forecasting. With a radar, nowcasters can recognize changes in shape, orientation, and speed of a moving, persistent meso-system, and identify new developing echoes. Although information on the mesoscale convergence in this thesis was retrieved from radar echo regions where rain had been produced already, highly sensitive Doppler radars (e.g., the NEXRAD¹) can provide such parameters in pre-storm environments (e.g., Wilson and Wilk 1982). The determination of mean vertical wind shear and the depth of the moist layer in the radar environment allows nowcasters to monitor important features of the flow, and to evaluate the likelihood of convective storm development and severe weather.

¹The abbreviation of NEXt generation of weather RADars (United States).

To investigate the development of individual cells in a multicell thunderstorm, it is of particular interest to observe the evolution of the three-dimensional distribution of the convergence. Incorporating Doppler radar measurements into a three-dimensional storm model would be an important tool for forecasting storms and precipitation.

References

- Chang, S. M., and H. D. Orville, 1973: Large-scale convergence in a numerical cloud model. *J. Atmos. Sci.*, **30**, 947-950.
- Chen, C. H., and H. D. Orville, 1980: Effects of mesoscale convergence on cloud convection. *J. Appl. Meteor.*, **19**, 256-274.
- Koscielny, A. J., R. J. Doviak, and R. Rabin, 1982: Statistical considerations in the estimation of divergence from single Doppler radar and application to pre-storm boundary-layer observation. *J. Appl. Meteor.*, **21**, 197-210.
- Lee, B. D., R. D. Farley, and M. R. Hjelmfelt, 1991: A numerical case study of convection initiation along colliding convergence boundaries in Northeast Colorado. *J. Atmos. Sci.*, **48**, 2350-2366.
- Lipps, F. B., and R. S. Hemler, 1986: Numerical simulation of deep tropical convection associated with large-scale convergence. *J. Atmos. Sci.*, **43**, 1796-1816.
- Matejka, T. J. and R. C. Srivastava, 1991: An improved version of the extended velocity-azimuth display analysis of single-Doppler radar data. *J. Atmos. Oceanic Technol.*, **8**, 453-466.
- Ogura, Y., and Y. L. Chen, 1977: A life history of an intense mesoscale convective storm in Oklahoma. *J. Atmos. Sci.*, **34**, 1458-1476.
- Ray, P. S. (Ed.), 1986: *Mesoscale Meteorology and Forecasting*. Amer. Meteor. Soc., Boston, 793 pp.
- Rogers, R. R., and M. K. Yau, 1989: *A Short Course in Cloud Physics*. 3rd edition, Peramon Press, Oxford, 293 pp.
- Song, J-L, and W. M. Frank, 1983: Relationships between deep convection and large-scale processes during GATE. *Mon. Wea. Rev.*, **111**, 2145-2160.
- Soong, S.-T., and Y. Ogura, 1973: A comparison between axisymmetric and slab-symmetric cumulus cloud model. *J. Atmos. Sci.*, **30**, 879-893.
- Srivastava, R. C., T. J. Matejka, and T. J. Lorello, 1986: Doppler radar study of the trailing anvil region associated with a squall line. *J. Atmos. Sci.*, **43**, 356-377.
- Ulanski, S. L., and M. Garstang, 1978: The role of surface divergence and vorticity in the life

- cycle of convective rainfall. Part I: Observation and analysis. *J. Atmos. Sci.*, **35**, 1047-1062.
- Waldteufel, R., and H. Corbin, 1979: On the analysis of single Doppler data. *J. Appl. Meteor.*, **18**, 532-542.
- Watson, A. I., and D. O. Blanchard, 1984: The relationship between total area divergence and convective precipitation in South Florida. *Mon. Wea. Rev.*, **112**, 673-685.
- Wilson, J. W., and W. E. Schreiber, 1986: Initiation of convective storms at radar-observed boundary-layer convergence lines. *Mon. Wea. Rev.*, **114**, 2516-2536.
- Wilson, J. W., and K. E. Wilk, 1982: Nowcasting applications of Doppler radar. In *Nowcasting*, K. Browning (Ed.), Academic Press, New York, 87-105.

Appendix A Characteristics of the Carvel Doppler Radar

Environment Canada operates a Doppler weather radar located at Carvel, Alberta (53°34' N, 114°09' W, 783 m), about 45 km west of Edmonton. This radar is used for general surveillance and operational weather forecasting. The scanning protocol goes through a cycle of 10 minutes, consisting of Doppler mode and conventional mode.

In the conventional mode, the radar scans at 23 elevation angles in a five minute period to produce a three-dimensional grid of radar reflectivity data. Such scans are referred to as a "full" volume scan. Data from the volume scan is used to produce CAPPI's (Constant Altitude Plan Position Indicator) and other display products such as radar echo top heights. In the next 5 minutes, the radar goes into the Doppler mode and scans at only four different elevation angles due to the slower rotating rate required for Doppler measurements.

Crozier (1986)¹ describes the technical specification of this Doppler radar. The important parameters are listed in Table A1.

¹Crozier C.L., 1986: *King Weather Radar Operations Manual and Users Guide*. Internal publication, Atmospheric Environment Service, Environment Canada.

Table A1. Characteristics of the Carvel radar.

<i>Parameters</i>	<i>Conventional Mode</i>	<i>Doppler Mode</i>
<i>Dish diameter (feet)</i>	12	
<i>Peak power (kw)</i>	260	
<i>Microwave wavelength (cm)</i>	5.34	
<i>Microwave frequency (MHz)</i>	5625	
<i>Scanning rate (rpm)</i>	6.0	0.75
<i>Elevation angles (degrees)²</i>	0.3 to 24.6 in 25 increments	0.5, 1.5 and 3.5 and 0.4 (folded)
<i>Pulse duration (μs)</i>	2.0	0.5
<i>Pulse length (m)</i>	600	150
<i>Pulse repetition frequency (Hz)</i>	250	1190 and 892
<i>Range resolution (m)</i>	300	75
<i>Beamwidth (degrees)</i>		1.1
<i>Effective azimuthal beamwidth (degrees)³</i>	2.2	1.4
<i>Display resolution (km)</i>	2	1.0
<i>Max. observed range (km)</i>	256	113
<i>Max. displayed range (km)</i>	220	110

²These values may vary slightly.

³This is the effective beamwidth when the motion of the antenna is taken into account.

Appendix B Doppler Radar Data Preprocessing

Processing the data sampled by the Carvel Doppler radar consists of five major steps as follows:

Step 1: **Decoding of radial velocity data.**

Doppler radar data are archived on optical disk at the Carvel radar site. Data unfolding is done prior to recording into data archive. A program¹ reading and decoding data files allows users to select the azimuths, ranges and elevation angles of the data to be decoded, and provides an ASCII format output.

Step 2: **Reformatting the radar data.**

Data reformatting is done according to the elevation angle and range gate number. For a specific elevation angle and range, the velocity data are rearranged according to the order of increasing azimuths.

Step 3: **Unfolding the velocity data.**

Radial velocities exceeding the maximum unambiguous velocity, V_{max} , are called “*folded*” (or aliased). The V_{max} is defined as

$$V_{max} = \pm \frac{PRF \cdot \lambda}{4} \quad (B.1)$$

where PRF and λ denote the radar’s Pulse Repetition Frequency and operating wavelength, respectively. Although the unfolding is done when the data are archived, some data still need to be corrected. Folded velocity values are identified by examining the continuity of the data along each radial. Any required velocity de-aliasing consists of

¹Provided by Tom Nichols, and modified by Bruno Larochelle of the Atmospheric Environment Service, Edmonton, Alberta.

adding or subtracting multiples of 2×12 or $2 \times 16 \text{ ms}^{-1}$ to the V_r at its location until the difference between it and neighbouring data is minimized (Crozier 1986)². The values of 2×12 and $2 \times 16 \text{ ms}^{-1}$, corresponding to the dual-PRFs used by the Carvel radar, represent the folds that possibly occur in the data.

Step 4: Filtering noise signals.

Whether a singular datum is actually a measurement of radial velocity or simply noise is recognized by examining its spectrum width. The spectrum width of an acceptable velocity measurement is given by (Doviak and Zrníc 1993, p.166)³:

$$\sigma_v^* = \frac{\lambda \cdot PRF}{4\pi} \quad (\text{B.2})$$

For the Carvel radar, $\sigma_v^* = 4.5 \text{ ms}^{-1}$. The Doppler velocity whose spectrum width is larger than σ_v^* is considered noise and excluded from analysis.

Step 5: Removing velocity outliers.

Some radial velocities reflect the presence of embedded convective or turbulent motions, and hence are not representative of the mesoscale or synoptic-scale wind field. These velocities are called *outliers*, and should be excluded from regression analyses. Velocity outliers are identified by their failure to conform to the pattern of most of the data in the ring or the analysis volume. Each of the radial velocity measurements is compared with its estimated value obtained from the analysis model (the VVP or EVAD algorithm). Velocities that deviate from the estimated value by more than a certain threshold (3 ms^{-1} for the EVAD, and 5 ms^{-1} for the VVP analyses) are considered as outliers. These outliers are not used in subsequent analysis.

²Crozier, C. L., 1986: *King Weather Radar Operations Manual and Users Guide*. Internal publication, Atmospheric Environment Service, Environment Canada.

³Doviak, R. J., and D. S. Zrníc, 1993: *Doppler Radar and Weather Observations*. 2nd edition, Academic Press, San Diego, California, 562 pp.